

Chapter 8

Panels

In Section 8.1, the *rectangular plate-strip* under uniformly distributed harmonic load taking into account physical and *elastic-plastic deformations* is studied. Various *stress-strain relations* while cyclic loading are applied. Then a computational algorithm including reduction of PDEs to ODEs via either the Bubnov-Galerkin Method (BGM) or the Finite Difference Method (FDM) is described. Different numerical methods for computation of ODEs are reviewed and discussed.

Estimation of *Lyapunov exponents* (LEs) via analytical and numerical approaches is illustrated, and the problem of stability of the studied system is analyzed. Charts of vibrations' regimes for longitudinal and transversal vibrations are reported. Convergence and reliability of the obtained numerical results have been discussed.

Different transition scenarios from regular to chaotic dynamics have been detected and discussed. Then the *Sharkovsky's bifurcation series* has been reported. *Chaos-hyperchaos* and *hyper-hyperchaos* phase transitions have been studied with the help of LEs and *Lyapunov dimension* (LD). Reliability of the obtained chaotic zones has been addressed.

In Section 8.2, cylindrical panels of infinite length are studied. At first, the governing PDEs are formulated with boundary and initial conditions. Reliability of the solutions obtained via FDM is studied. The method of LEs computations is presented, and the chaos-hyperchaos transition as well as the Sharkovsky's series are detected and discussed.

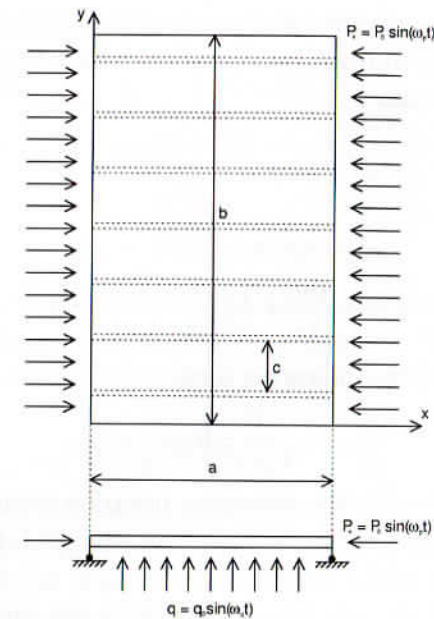


Fig. 8.1 Rectangular plate under periodic load.

8.1 Infinite Length Panels

8.1.1 Mathematical models

We consider nonlinear vibrations of a rectangular plate subjected to the action of uniformly distributed periodic load (Fig. 8.1).

We take into account two types of nonlinearities: physical and elastic-plastic deformations (assuming that loading and relief processes lie on the same curve, then we deal only with the physical nonlinearity). We consider a long plate ($a \ll b$), and we study the plate parts in the neighborhood of its short sides, whereas on the remaining lengths the plate bending is located on a cylindrical surface. We consider a beam-strip of a unit width and having length a . This approach allows to reduce a PDE to that of only one spatial coordinate x . The bended plate is supported by a set of elastic ribs with the same stiffness which are located in parallel to the plate short side a , and the distance between ribs is c . We additionally assume that the ribs may be only compressed.

Surface of the transversal section of each rib is F , i.e. the separated beam-strip has the width $F_c = F/c$. The deformations in the middle beam-strip surface are

$$\begin{aligned} e_{xx} &= \varepsilon_{11} + z\chi_{11}, \\ \chi_{11} &= -\frac{\partial^2 w}{\partial x^2}, \\ \varepsilon_{11} &= \frac{\partial u}{\partial x} + \frac{1}{2}\left(\frac{\partial w}{\partial x}\right)^2 + k_x w. \end{aligned} \quad (8.1)$$

Hooke's law has the following form

$$\sigma_{xx} = \frac{E}{1-\nu^2}[e_{xx} - \varepsilon_{xx}^T], \quad (8.2)$$

where $\varepsilon_{xx}^T = \alpha_T T + \varepsilon_{xx}^{1p}$. The following notation is further used: α_T is the coefficient of linear material heat extension; T is the temperature; w is the deflection of the middle beam surface; u is the displacement in the direction of the axis Ox ; $k_x = 1/R_x$ is the curvature regarding x ; h is the beam thickness; ν is the Poisson's coefficient; g is the Earth acceleration; γ is the specific beam material weight; ε_{xx}^{1p} is the plastic component per loading moment.

Owing to the Birger method of variable elasticity parameters in the form (8.2), we get a relation between stresses and deformations. We assume that the Young's modulus and Poisson's coefficient are not fixed but they depend on the deformed state, i.e. $E = E(x, z, e_0, e_{is}, T)$, $\nu = \nu(x, z, e_0, e_{is}, T)$, where e_0 is volume deformation, e_{is} is plastic deformation. Substitution of (8.1) into (8.2), yields

$$\sigma_{xz} = \frac{E}{1-\nu^2}[\varepsilon_{11} + z\chi_{11} - \varepsilon_{xz}^T]. \quad (8.3)$$

Integration of (8.3) regarding z allows to get forces in the middle plate-strip surface:

$$\begin{aligned} T_{11} &= \int_{-h/2}^{h/2} \sigma_{xx} dz = \varepsilon_{11} \int_{-h/2}^{h/2} \frac{E}{1-\nu^2} dz \\ &+ \chi_{11} \int_{-h/2}^{h/2} \frac{Ez}{1-\nu^2} dz - \int_{-h/2}^{h/2} \frac{E}{1-\nu^2} \varepsilon_{xx}^T dz. \end{aligned} \quad (8.4)$$

Introducing notation

$$a_i = \int_{-h/2}^{h/2} \frac{Ez^i}{1-\nu^2} dz, \quad b_i = \int_{-h/2}^{h/2} \frac{Ez^i}{1-\nu^2} \varepsilon_{xx}^T dz, \quad i = 0, 1, 2, \quad (8.5)$$

we get

$$T_{11} = a_0 \varepsilon_{11} + a_1 \chi_{11} - b_0. \quad (8.6)$$

Note that the coefficient b_0 contains components of the temperature and the remaining plastic deformations. Solving (8.6) with respect to tangential deformations we get

$$\varepsilon_{11} = \frac{1}{a_0} T_{11} - \frac{a_1}{a_0} \chi_{11} + \frac{b_0}{a_0}. \quad (8.7)$$

Further, we multiply both sides of Eq. (8.3) by z and carry out the integration of the plate-strip along its thickness. We get the bending moment

$$M_{11} = \int_{-h/2}^{h/2} \sigma_{xx} z dz = a_1 \varepsilon_{11} + a_2 \chi_{11} - b_1. \quad (8.8)$$

We substitute deformation of the middle surface (8.7) into (8.8) to get

$$\begin{aligned} M_{xx} &= a_1 \left(\frac{1}{a_0} T_{11} - \frac{a_1}{a_0} \chi_{11} + \frac{b_0}{a_0} \right) + a_2 \chi_{11} - b_1 \\ &= \frac{a_1}{a_0} T_{11} + \left(a_2 - \frac{a_1^2}{a_0} \right) \chi_{11} + \left(\frac{a_1 b_0}{a_0} - b_1 \right). \end{aligned} \quad (8.9)$$

Taking into account the following notation

$$A_1 = \frac{a_1}{a_0}, \quad A_2 = a_2 - \frac{a_1^2}{a_0}, \quad M_{xz}^0 = \frac{a_1 b_0}{a_0} - b_1, \quad (8.10)$$

Eq. (8.9) can be cast to the following form

$$M_{xx} = A_1 T_{11} + A_2 \chi_{11} + M_{xz}^0. \quad (8.11)$$

The equilibrium equation is as follows

$$\frac{\partial^2 M_{xx}}{\partial x^2} + \frac{\partial}{\partial x} \left(T_{11} \frac{\partial w}{\partial x} \right) + k_x T_{11} + q - \frac{h\gamma}{g} \frac{\partial^2 w}{\partial t^2} - \varepsilon h \frac{\partial w}{\partial t} = 0. \quad (8.12)$$

Equation of compatibility of deformations is not applied here, since the beam deflections depend only on x . The forces T_{11} occurred in the beam middle surface are generated by reactions coming from reinforced ribs, and they will be further denoted by T . They are constant along the whole length of the beam-strip, and Eq. (8.12) can be rewritten in the following form

$$\frac{\partial^2 M_{xx}}{\partial x^2} + \frac{\partial^2 w}{\partial x^2} + Tk_x + q - \frac{h\gamma}{g} \frac{\partial^2 w}{\partial t^2} - \varepsilon h \frac{\partial w}{\partial t} = 0. \quad (8.13)$$

We derive the equation of compatibility of deformation of the beam-strip and the stiff rib. We define the joint support displacement generated by the beam-strip deformation. For this purpose we write equation of coupling between deformations of the middle surface with displacements

$$\frac{\partial u}{\partial x} = \varepsilon_{11} + k_x w - \frac{1}{2} \left(\frac{\partial w}{\partial x} \right)^2. \quad (8.14)$$

In the latter relation we substitute ε_{11} from the Hook law for the middle surface (8.7), and we obtain

$$\varepsilon_{11} = \frac{1}{a_0} T_{11} - \frac{a_1}{a_0} \chi_{11} + \frac{b_0}{a_0} + k_x - \frac{1}{2} \left(\frac{\partial w}{\partial x} \right)^2. \quad (8.15)$$

Therefore, we may compute the full displacement of support Δ (we call it positive, when supports approach each other):

$$\begin{aligned} \Delta &= - \int_0^a \frac{\partial u}{\partial x} dx = \frac{1}{2} \int_0^a \left(\frac{\partial w}{\partial x} \right)^2 dx - \int_0^a \left(\frac{1}{a_0} T_{11} - \frac{a_1}{a_0} \chi_{11} + \frac{b_0}{a_0} \right) dx \\ &\quad - k_x \int_0^a w dx = \frac{1}{2} \int_0^a \left(\frac{\partial w}{\partial x} \right)^2 dx - T^* - k_x \int_0^a w dx. \end{aligned} \quad (8.16)$$

On the other hand, the quantity Δ is described as shortening of the reinforced beam

$$\Delta = \frac{\sigma_p (1 - \nu_p^2)}{E_p} a. \quad (8.17)$$

The following notation has been applied: σ_p is the compressing stress in a rib, E_p is the constant elasticity material modulus. Multiplier $(1 - \nu_p^2)$ is introduced because the separated stiff rib plays the

role of a thin beam of a rib. Comparison of expressions (8.16) and (8.17) yields

$$\frac{\sigma_p (1 - \nu_p^2)}{E_p} a + T^* = \frac{1}{2} \int_0^a \left(\frac{\partial w}{\partial x} \right)^2 dx - k_x \int_0^a w dx. \quad (8.18)$$

We have introduced a series of assumptions so far. In particular, we have assumed that the deflections of the beam-strip are small in comparison to dimension a , and forces T_{11} acting on the ends of the elementary element dx should be equal, i.e. we have applied here the theory of average bending.

Equilibrium condition of a movable beam-strip end yields

$$\sigma_p = \frac{T^*}{F_e}, \quad (8.19)$$

and substituting it to (8.18) yields

$$T^* \left(\frac{\sigma_p (1 - \nu_p^2)}{E_p F_e} a + 1 \right) = \frac{1}{2} \int_0^a \left(\frac{\partial w}{\partial x} \right)^2 dx - k_x \int_0^a w dx, \quad (8.20)$$

and hence

$$T^* = \frac{\frac{1}{2} \int_0^a \left(\frac{\partial w}{\partial x} \right)^2 dx - k_x \int_0^a w dx}{\left(\frac{\sigma_p (1 - \nu_p^2)}{E_p F_e} a + 1 \right)}. \quad (8.21)$$

In what follows, while applying the iteration procedure, the value T^* will be given from a previous iterative step, i.e.

$$\begin{aligned} T^* &= \int_0^a \left(\frac{1}{a_0} T_{11} - \frac{a_1}{a_0} \chi_{11} + \frac{b_0}{a_0} \right) dx \\ &= T_{11} \int_0^a \frac{1}{a_0} dx - \int_0^a \left(\frac{b_0}{a_0} - \frac{a_1}{a_0} \chi_{11} \right) dx = T_{11} \beta_1 + \beta_0. \end{aligned} \quad (8.22)$$

Therefore, using (8.21) we obtain

$$T_{11} = \frac{\frac{1}{\beta_1} \left(\frac{1}{2} \int_0^a \left(\frac{\partial w}{\partial x} \right)^2 dx - k_x \int_0^a w dx \right)}{\left(\frac{\sigma_p (1 - \nu_p^2)}{E_p F_e} a + 1 \right)} - \frac{\beta_0}{\beta_1}. \quad (8.23)$$

In the case when both ends of the beam-strip are clamped we can take $F_e = \infty$ and the formula is essentially simplified. Let us come back to Eq. (8.12). The values of T_{11} are found through the iteration process via formula (8.23), whereas the value of M_{xx} is yielded by formula (8.11), assuming that $\chi = -\frac{\partial^2 w}{\partial x^2}$. Therefore, we have got the algorithm of computation of infinite panels taking into account geometric nonlinearities and elasto-plastic deformation as well as the external load action.

8.1.1.1 Relief process and secondary plastic deformations

We consider the dependence between strains and stresses for an isotropic material in the following way

$$e_{xx} = \frac{1}{E}\sigma_{xx} + \varepsilon_{xx}^{1p}. \quad (8.24)$$

The Mises flow material criterion is applied [Hill (1956)], since it is validated experimentally by soft materials like aluminum, copper, iron and steel.

In the theory of small elastic-plastic deformations, the properties of the dependence between stresses and deformations are defined by the function

$$\sigma_i = f(e_i), \quad (8.25)$$

where σ_i is the stress intensity, e_i is the strain intensity, G_0 is the characteristic value of the shear modulus in the non-deformed state, σ_s is the plastic flow threshold, e_1^p is the residual deformation in a studied element in the loading instants, e_2^p is the beginning of a secondary loading (Fig. 8.2).

It is assumed that formula (8.25) does not depend on the stress state, and it can be found experimentally while stretching-compressing a cylindrical sample. Below, we give a few analytical forms of dependence $\sigma_i = f(e_i)$:

1. Ideally elastic-plastic body:

$$\sigma_i = \begin{cases} 3G_0 e_i, & \text{for } e_i < e_s, \\ \sigma_s, & \text{for } \geq e_s. \end{cases} \quad (8.26)$$

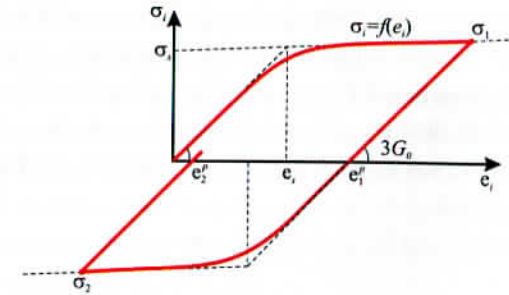


Fig. 8.2 Dependence of the intensity of the deformation of the stress intensity.

2. Elastic-plastic body with a linear strain hardening:

$$\sigma_i = \begin{cases} 3G_0 e_i, & \text{for } e_i < e_s, \\ 3G_0 e_i + 3G_1 (e_i - e_s), & \text{for } e_i \geq e_s. \end{cases} \quad (8.27)$$

3. Pure aluminum model:

$$\sigma_i = \sigma_s [1 - \exp(-e_i/e_s)]. \quad (8.28)$$

4. Fractional exponent dependence:

$$\sigma_i = A e_i^m, \quad 0 \leq m \leq 1. \quad (8.29)$$

where A and m are defined experimentally.

5. Cubic dependence:

$$\sigma_i = E e_i - m e_i^3. \quad (8.30)$$

where E and m are material constants.

6. Fifth degree polynomial:

$$\sigma_i = E e_i - m e_i^3 - m_2 e_i^5. \quad (8.31)$$

where E , m_1 and m_2 are material constants.

7. Square formula:

$$\sigma_i = \frac{A e_i}{\sqrt{1 + \left(\frac{e_i}{m}\right)^2}}. \quad (8.32)$$

8. Ramberg-Osgood formula [Ramberg and Osgood (1943)]:

$$\sigma_i = E e_i - A e_i^m. \quad (8.33)$$

Besides the mentioned formulas $\sigma_i(e_i)$ one may find more examples of the stress-strain relations in the literature. However, for our algorithm the dependence $\sigma_i(e_i)$ can be defined arbitrarily, even in the form of a table obtained from standard experimental results.

In what follows, we consider $\sigma_i(e_i)$ presented in Fig. 8.2. In the elastic part, we have

$$\sigma_i = 3G_0 e_i, \quad (8.34)$$

where G_0 is the characteristic value of the shear modulus in the non-deformed state.

After achieving an elasticity threshold, the loading process ($de_i > 0$) $\sigma_i(e_i)$ is described by (8.25). For lightening ($de_i \leq 0$), owing to the reference [Schevchenko (1970)], $\sigma_i(e_i)$ is defined by relations:

$$\sigma_i = 3G_0 e''_i, \quad e''_i = e_i - e_1^p, \quad (8.35)$$

where e_1^p is the remaining deformation in an element in the lightening time instant. Formula (8.35) defines $\sigma_i(e_i)$ in the case, when in the element (while lightening) the secondary plastic flow deformation does not appear. In a domain of the secondary plastic deformation ($e_i > e_s$), their intensity is defined by the following formula

$$\sigma_i = f_1(e_i). \quad (8.36)$$

Functions $f_1(e_i)$ and $f(e_i)$ do not depend on the stress material state and they are defined experimentally by a stress-strain investigation of cylindrical samples. Owing to the geometrical interpretation of the deformation process in the plane $\sigma_i - \sigma_s$, the quantity e''_i can be presented in the following form

$$e''_i = e_i - e_1^p, \quad (8.37)$$

i.e. in the way as in (8.35), but in this case e''_i and σ_i are negative quantities.

The so far given representation of e''_i corresponds to system coordinates (e''_i, σ_i) , and the directions of axes coincide with the directions of axes (e_i, σ_i) . If after the lightening process a body is loaded by the forces with opposite signs with respect to the firstly initiated loading, then it is more convenient to apply the system coordinates (e_i^1, σ_i^1) with the axes "e" having directions opposite to the axes of

e_i and σ_i . In the latter case $e'_i = e_1^p - e_i$ for $e_i \geq e_1^p$, and for $e_i < e_1^p$ the following formula holds: $e'_i = e_i - e_1^p$.

The corresponding changes should be carried out in relations (8.35), (8.36) and all successive relations. In both cases, the origin of estimation of stress-strain intensity is related to the body element state, which has only plastic components of deformation ε_{ij}^{1p} , occurring in this element up to the beginning of the lightening. Further, we apply the coordinates (e''_i, σ_i) .

For material exhibiting the ideal Bauschinger effect [Kadashevich and Novozhilov (1958)], the equation of curve (8.36) in the space of secondary plastic deformations can be written applying the transformed function $\sigma_i = f_1(e_i)$ in the following form [Schevchenko (1970)]:

$$\sigma_i = \sigma_1 - \sigma_s - f\left(e_1^p + \frac{\sigma_1 - \sigma_s}{3G_0} - e_i\right), \quad (8.38)$$

where σ_1 is a stress corresponding to the beginning of lightening.

Function (8.38) in plane (e_i, σ_i) represents a curve which can be obtained via a parallel displacement of the curve $\sigma_i = f_1(e_i)$ on the value of $\sigma_i = \sigma_1 - \sigma_s$, $e_i = e_1^p + \frac{\sigma_1 - \sigma_s}{3G_0}$, and then the rotation by an amount of radians around the point with the given coordinates. Therefore, for $e_i = e_s^0$ we have $\sigma_i = \sigma_1 - 2\sigma_s$.

Relation (8.38) defines the dependence between intensities of σ_i and e_i in a domain of elastic lightening, if the function f in (8.38) for $e_i > e_s^0$ is written in the following form

$$f\left(e_1^p + \frac{\sigma_1 - \sigma_s}{3G_0} - e_i\right) = 3G_0 \left(e_1^p + \frac{\sigma_1 - \sigma_s}{3G_0} - e_i\right). \quad (8.39)$$

If in the separated body elements, after the lightening with secondary plastic deformations, the process of the next loading $de_i > 0$, the dependence $\sigma_i = f_1(e_i)$ will be described by the formula (8.35), where $e''_i = e_i - e_2^p$, and e_2^p corresponds to the beginning of the secondary loading. If the secondary loading process is associated with the change in plastic deformations, then the intensity of stresses is not governed by (8.35), but rather by the following formula

$$\sigma_i = f_2(e''_i). \quad (8.40)$$

The formula (8.40), similar to functions (8.25) and (8.36), does not depend on the stress state character, and it is defined experimentally. Functions (8.40) define in plane (e_i, σ_i) a curve, a straight line (8.35) (elastic deformation), under the condition that e_i'' is defined by the following equation

$$e_i'' = e_i - e_2^p. \quad (8.41)$$

For a material with the ideal Bauschinger effect [Kadashevich and Novozhilov (1958)], the function (8.40) is defined in the following way [analogously to (8.38) and (8.39)]

$$\sigma_i = \sigma_2 + \sigma_s + f \left(e_i - e_2^p + \frac{\sigma_2 - \sigma_s}{3G_0} \right), \quad (8.42)$$

and the elastic part of the deformation curve is approximated by the following formula

$$f \left(e_i - e_2^p + \frac{\sigma_2 - \sigma_s}{3G_0} \right) = 3G_0 \left(e_i - e_2^p + \frac{\sigma_2 - \sigma_s}{3G_0} \right), \quad (8.43)$$

where σ_2 is the stress intensity defined by the formula (8.38) in time instant associated with the beginning of the secondary loading.

It should be emphasized that the given process takes place in all sample points and in all time instants.

8.1.1.2 Mathematical model and computational algorithm

We consider nonlinear vibrations of a rectangular plate subjected to the longitudinal harmonic load under the condition that one of the plate dimensions is larger than the second one, i.e. $a \ll b$ (Fig. 8.3). We are interested in beam-strip parts adjacent to short edges, and we assume that on the remaining parts the plate is bent along a cylindrical surface. Then, it is sufficient to investigate vibrations of a beam-strip of length a and width equal to 1. Therefore, it is necessary to solve Eq. (8.13) satisfying the following assumptions: lack of curvature $k_x = 0$; intensity of the stress-state $\sigma_i = \frac{E}{1-\nu^2} e_i$, where E (Young's modulus) is constant; temperature influence is neglected $\alpha_T = 0$.

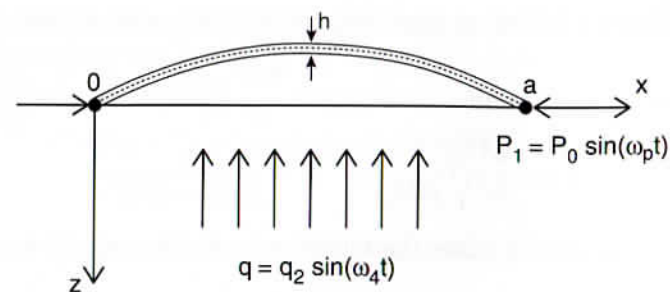


Fig. 8.3 Computational scheme.

The so far given assumptions essentially simplify the computational algorithm given in the previous subsection. Namely, we get

$$\begin{aligned} a_0 &= \frac{Eh}{1-\nu^2}, \quad a_1 = 0, \quad a_2 = \frac{Eh^3}{12(1-\nu^2)}, \quad b_1 = 0, \\ T &= \frac{1}{2\beta_1} \int_0^a \left(\frac{\partial w}{\partial x} \right)^2 dx = \frac{Eh}{2\alpha(1-\nu^2)} \int_0^a \left(\frac{\partial w}{\partial x} \right)^2 dx, \\ M_{xx} &= a_2 \chi_{11} = -\frac{Eh^3}{12(1-\nu^2)} \frac{\partial^2 w}{\partial x^2}. \end{aligned} \quad (8.44)$$

In this way, we have omitted the iteration procedure, and we have got the following 1D variant of the von Kármán equations:

$$\begin{aligned} \frac{h\gamma}{g} \ddot{w} + h\varepsilon \dot{w} &= -D \frac{\partial^4 w}{\partial x^4} + \frac{Eh}{2a(1-\nu^2)} \left\{ \int_0^a \left(\frac{\partial w}{\partial x} \right)^2 dx \right\} \frac{\partial^2 w}{\partial x^2} \\ &\quad - P_x(t) \frac{\partial^2 w}{\partial x^2} + q(t, x), \end{aligned} \quad (8.45)$$

where $w(x, t)$ is the deflection function, x is the spatial coordinate, t is time, a is the dimension of beam-strip, h is the thickness, $P_x(t)$, $q(x, t)$ are longitudinal/parametric and transversal loads, respectively, E is Young's modulus, $D = \frac{Eh^3}{12(1-\nu^2)}$ is the cylindrical stiffness, ν is Poisson's coefficient, γ is volume specific material weight, g is the Earth acceleration, ε is the damping coefficient. We recast the governing equations to the counterpart non-dimensional form by

introducing the following non-dimensional parameters (with bars):

$$x = a\bar{x}, \quad w = h\bar{w}, \quad P_x(t) = \frac{Eh^3}{a^2} \bar{P}_x(t), \quad q = \frac{Eh^4}{a^4} \bar{q},$$

$$t = \frac{a^2}{h^2} \sqrt{\frac{\gamma}{Eh^2g}} \bar{t}, \quad \lambda = \frac{1}{12(1-\nu^2)}.$$

Finally, Eq. (8.45) takes the following non-dimensional form (bars are omitted)

$$\ddot{w} + \varepsilon \dot{w} = -\lambda \frac{\partial^4 w}{\partial x^4} + 6\lambda \left\{ \int_0^1 \left(\frac{\partial w}{\partial x} \right)^2 dx \right\} \frac{\partial^2 w}{\partial x^2} - P_x(t) \frac{\partial^2 w}{\partial x^2} + q(t, x). \quad (8.46)$$

In Eq. (8.46), dissipative properties being proportional to the motion velocity are taken into account. It should be emphasized that different models of dissipative properties are used (see Chapter 5 and the reference [Bolotin (1961)] for more details). As it is known from a linear theory of vibrations, there exists linear and nonlinear frictions (see [Golovin (2012)]). The latter one can be approximated by various analytical formulas. When the bodies are cyclically loaded and deformed, the Hooke's law violation is observed (even for loading) exhibited by the occurrence of hysteretic loops. The surface of a hysteresis loop defines energy dissipated per one cycle of vibrations and per unit of material volume. It is already known that hysteresis loop surface, for majority of the used materials in industrial applications, does not depend on the deformation frequency process, but it rather depends on the deformation amplitude. Equation (8.46) should be supplemented with one of the following boundary conditions:

(i) Simple-simple support:

$$w = w''_x = 0, \quad \text{for } x = 0, 1; \quad (8.47)$$

(ii) Clamping-clamping support:

$$w = w'_x = 0, \quad \text{for } x = 0, 1; \quad (8.48)$$

(iii) Simple-clamping support:

$$w(0) = w'_x(0) = 0, \quad w(1) = w''_x(1) = 0, \quad (8.49)$$

and one of the following initial conditions associated with the mentioned boundary conditions:

(i)

$$w(x)|_{t=0} = w_0 \sin(\pi x), \quad \dot{w}(x)|_{t=0} = 0; \quad (8.50)$$

(ii)

$$w(x)|_{t=0} = w_0(1 - \cos(2\pi x)), \quad \dot{w}(x)|_{t=0} = 0; \quad (8.51)$$

(iii)

$$w(x)|_{t=0} = f(x), \quad \dot{w}(x)|_{t=0} = 0. \quad (8.52)$$

Function $f(x)$ describes a deflection defined by the set-up method with respect to a small value of the transversal external load action [Feodosev (1963)].

In this chapter, we consider nonlinear vibrations with linear friction. It should be emphasized that when a constant load is applied, then the problem is reduced to the solution of a static problem. Namely, a so-called set-up problem can be applied, when $\varepsilon = \varepsilon_{cr}$ (critical damping). Then the vibrations of the investigated plate rapidly fast decrease, and the solution tends to its stationary counterpart for $\{q_i\} \rightarrow \{w_i\}$. The set-up method was firstly applied by Feodosev, who considered a stability problem of a spherical dome subjected to the transversal load. It should be noted that dissipative terms are introduced artificially even to solve large sets of algebraic equations, and then the iterative process is obtained having a lot of advantages in comparison to the widely used Newton's method. For time dependent loads $P_x(t)$, $q(x, t)$, the parameter ε essentially influences the character of vibrations of a mechanical system as well as the location of chaotic zones.

8.1.2 Reduction of PDEs to ODEs

8.1.2.1 The BGM

The BGM [Volmir (1972)] allows to reduce the initial-boundary problem governed by a PDE (problem of infinite dimension) to a set of truncated ODEs (problem of finite dimension). Although this method has a series of advantages, it also possesses drawbacks. From one side

it allows to get reliable qualitative results even if rough approximation is used, but from the other side the method strongly depends on the introduced boundary conditions. A numerical experiment shows that the mentioned method allows to achieve convergence of the iterations already using 2–3 series terms, which means that the system of ODEs with low dimension can be applied.

Let us introduce a solution in the following form

$$w(x, t) = \sum_{i=0}^N A_i(t) w_i(x), \quad (8.53)$$

where $w(x, t)$ should satisfy the introduced boundary conditions. After application of the BGM to Eq. (8.46), the following system of ODEs is obtained for $A_i(t)$:

$$\begin{aligned} \sum_{i=0}^N (\ddot{A}_i + \varepsilon \dot{A}_i) a_{ik} = & -\lambda \sum_{i=0}^N A_i b_{ir} + 6\lambda L(\{A_i\}_1^N) \sum_{i=0}^N A_i c_{ik} \\ & - P_x(t) \sum_{i=0}^N A_i c_{ik} + Q_k(t), \end{aligned} \quad (8.54)$$

where $k = 0, 1, \dots$

In the above, the following notation for the coefficients is applied

$$\begin{aligned} a_{ik} &= \int_0^1 w_i(x) w_k(x) dx, \quad b_{ik} = \int_0^1 w_i^{IV}(x) w_k(x) dx, \\ c_{ik} &= \int_0^1 w_i''(x) w_k(x) dx, \quad Q_k(t) = \int_0^1 q(x, t) w_k(x) dx, \\ L(\{A_i\}_1^N) &= \int_0^1 \left\{ \sum_{i=0}^N A_i(t) w'_i(x) \right\}^2 dx. \end{aligned} \quad (8.55)$$

The system of second-order ODEs can be reduced to that of first-order ODEs, which can be directly solved with one of the widely applied Runge–Kutta methods.

We analyze the BGM applied vibrations of an infinite panel with a geometric nonlinearity. We consider a solution to Eq. (8.46) with simple support (8.47). We take $\{\sin \pi(2i+1)x\}_{i=1\dots N}$ as basic functions of BGM. Since they satisfy the boundary conditions, we take the solution in the following form

$$w(x, t) = \sum_{i=1}^N A_i(t) \sin(\pi(2i+1)x). \quad (8.56)$$

Substituting (8.56) into (8.46), we get

$$\begin{aligned} \sum_{i=1}^N (\ddot{A}_i + \varepsilon \dot{A}_i) \sin(\pi(2i+1)x) = & -\lambda \sum_{i=1}^N A_i (\pi(2i+1))^4 \sin(\pi(2i+1)x) - 6\lambda L(\{A_i\}_1^N) \\ & - P_x(t) \sum_{i=1}^N A_i (\pi(2i+1))^2 \sin(\pi(2i+1)x) + q(x, t), \end{aligned} \quad (8.57)$$

where

$$\begin{aligned} L(\{A_i\}_1^N) &= \int_0^1 \left\{ \sum_{i=1}^N A_i (\pi(2i+1)) \cos(\pi(2i+1)x) \right\}^2 dx \\ &= \sum_{i=1}^N \sum_{j=1}^N \int_0^1 \{A_i A_j \pi^2 (2i+1)(2j+1) \\ &\quad \times \cos(\pi(2i+1)x) \cos(\pi(2j+1)x) dx \\ &= \sum_{i=1}^N \int_0^1 \{A_i \pi(2i+1) \cos(\pi(2i+1)x)\}^2 dx \\ &= \frac{\pi^2}{2} \sum_{i=1}^N (A_i(2i+1))^2. \end{aligned} \quad (8.58)$$

We multiply both sides of (8.57) by $\sin(\pi(2j+1)x)$, and then we integrate both sides of the new equations for x from 0 to 1 to get

$$\begin{aligned} & \sum_{i=1}^N (\ddot{A}_i + \varepsilon \dot{A}_i) \int_0^1 \sin(\pi(2i+1)x) \sin(\pi(2j+1)x) dx \\ &= -\lambda \sum_{i=1}^N A_i (\pi i)^4 \int_0^1 \sin(\pi(2i+1)x) \sin(\pi(2j+1)x) dx \\ &+ (6\lambda L \left(\{A_i\}_1^N \right) \\ &- P_x(t)) \sum_{i=1}^N A_i (\pi i)^2 \int_0^1 \sin(\pi i x) \sin(\pi j x) dx \\ &+ q(x, t) \int_0^1 \sin(\pi j x) dx. \end{aligned} \quad (8.59)$$

Since functions $\{\sin(\pi i x)\}_1^N$ are mutually orthogonal in the interval $[0; 1]$, the following equations are finally obtained

$$\begin{aligned} \ddot{A}_j + \varepsilon \dot{A}_j &= -\lambda A_j (\pi j)^4 - \left(3\lambda \pi^2 \sum_{i=1}^N (A_i i)^2 - P_x(t) \right) A_j (\pi j)^2 \\ &+ \frac{4}{\pi j} q(x, t). \end{aligned} \quad (8.60)$$

The N second-order ODEs are transformed to a system of $2N$ first-order differential equations of the following form

$$\begin{aligned} \dot{A}_j(t) &= A'_j(t), \\ A'_j &= -\varepsilon A'_j - \lambda A_j (\pi j)^4 - \left(3\lambda \pi^2 \sum_{i=1}^N (A_i i)^2 - P_x(t) \right) A_j (\pi j)^2 \\ &+ \frac{4}{\pi j} q(x, t), \end{aligned} \quad (8.61)$$

which are solved numerically using one of the Runge-Kutta methods. We consider the problem separately for lack of transversal excitation ($q(x, t) = 0$). It is obvious that in the case when the initial system deflection does not exist, the solution to the problem is trivial (zero). This is why we introduce the initial conditions in the form of (8.50),

which corresponds to the introduction of an artificial small deflection of the plate. Owing to the structure of Eq. (8.61) one may conclude that the initial perturbation in the form of a first harmonic does not interact with higher order harmonics (the coefficients standing by higher harmonics are equal to zero). In the latter case, the system of Eq. (8.60) is reduced to the well-known Duffing equation [Nayfeh and Mook (1995)] of the form

$$\ddot{A}_1 + \varepsilon \dot{A}_1 = -(\lambda \pi^2 (1 + 3A_1^2) - P_x(t)) A_1 \pi^2. \quad (8.62)$$

We consider a solution of Eq. (8.46) with boundary conditions (8.48). As basic functions of the Bubnov-Galerkin approach, we take: $\{\cos \pi 2ix - 1\}_{i=0 \dots N}$, or equivalently, we assume the following solution form

$$w(x, t) = \sum_{i=1}^N A_i(t) (\cos(2\pi i x) - 1). \quad (8.63)$$

Substituting (8.63) into Eq. (8.46), we get

$$\begin{aligned} & \sum_{i=1}^N (\ddot{A}_i + \varepsilon \dot{A}_i) (\cos(2\pi i x) - 1) \\ &= -\lambda \sum_{i=1}^N A_i (2\pi i)^4 \cos(2\pi i x) - (6\lambda L \left(\{A_i\}_1^N \right) \\ &- P_x(t)) \sum_{i=1}^N A_i (2\pi i)^2 \cos(2\pi i x) + q(x, t), \end{aligned} \quad (8.64)$$

where

$$\begin{aligned} L \left(\{A_i\}_1^N \right) &= \int_0^1 \left\{ \sum_{i=1}^N A_i 2\pi i \sin(2\pi i x) \right\}^2 dx \\ &= \sum_{i=1}^N \sum_{j=1}^N \int_0^1 \{A_i A_j 4\pi^2 \sin(2\pi i x) \sin(2\pi j x)\} dx \end{aligned}$$

$$= \sum_{i=1}^N \int_0^1 \{A_i 2\pi i \sin(2\pi i x)\}^2 dx = 2\pi^2 \sum_{i=1}^N (A_i i)^2. \quad (8.65)$$

Multiplying both sides of Eq. (8.64) by $\cos(2\pi j x)$, and carrying out the integration procedure from 0 to 1, we obtain

$$\begin{aligned} & \sum_{i=1}^N (\ddot{A}_i + \varepsilon \dot{A}_i) \int_0^1 (\cos(2\pi i x) - 1) \cos(2\pi j x) dx \\ &= -\lambda \sum_{i=1}^N A_i (2\pi i)^4 \int_0^1 \cos(2\pi i x) \cos(2\pi j x) dx \\ &+ q(x, t) \int_0^1 \cos(2\pi j x) dx \\ &- (6\lambda L (\{A_i\}_1^N) - P_x(t)) \sum_{i=1}^N A_i (2\pi i)^2 \\ &\times \int_0^1 \cos(2\pi i x) \cos(2\pi j x) dx. \end{aligned} \quad (8.66)$$

Since the functions $\{\cos(2\pi i x)\}_1^N$ are mutually orthogonal on interval $[0 : 1]$, the following system of equations is obtained

$$\begin{aligned} \ddot{A}_j + \varepsilon \dot{A}_j &= -\lambda A_j (2\pi j)^4 - \left(12\lambda\pi^2 \sum_{i=1}^N (A_i i)^2 - P_x(t) \right) A_j (2\pi j)^2 \\ &- \sum_{i=1}^N (\ddot{A}_i + \varepsilon \dot{A}_i) = q(x, t), \end{aligned} \quad (8.67)$$

which is reduced to the following first-order differential equations

$$\begin{aligned} \dot{A}_j(t) &= A'_j(t), \\ \dot{A}'_j &= -\varepsilon A'_j - \lambda A_j (2\pi j)^4 - \left(12\lambda\pi^2 \sum_{i=1}^N (A_i i)^2 - P_x(t) \right) A_j (2\pi j)^2. \end{aligned} \quad (8.68)$$

8.1.2.2 FDM

Explicit and implicit schemes

In order to reduce PDEs (8.46) to ODEs, we apply the FDM to the spatial coordinate x . In the mesh

$$G_N = \{0 \leq x_i \leq 1, x_i = i/N, i = 0, \dots, N\}, \quad (8.69)$$

we substitute the partial derivatives by their difference counterparts, and we get

$$\begin{aligned} \ddot{w}_i + \varepsilon \dot{w}_i &= -\lambda \Lambda_{x^4}(w_i) + 6\lambda \left\{ \int_0^1 \Lambda_x^2(w_i) dx \right\} \Lambda_{x^2}(w_i) \\ &- P_x(t) \Lambda_{x^2}(w_i) + q(ih, t). \end{aligned} \quad (8.70)$$

Integral occurring in (8.70) can be found numerically, for example, via the Simpson formula. The following formulas hold for the boundary conditions (8.48), (8.47):

1. Simply supported edge $(\cdot)_{-i} = -(\cdot)_i$.
2. Clamped edge $(\cdot)_{-i} = (\cdot)_i$.

Introduction of the change in variables

$$\dot{w}_i = w'_i \quad (8.71)$$

reduces second-order ODEs (8.70) to the first-order ODEs regarding deflections w_i and velocities w'_i of the following form

$$\begin{aligned} \dot{w}'_i + \varepsilon w'_i &= -\lambda \Lambda_{x^4}(w_i) + 6\lambda \left\{ \int_0^1 \Lambda_x^2(w_i) dx \right\} \Lambda_{x^2}(w_i) \\ &- P_x(t) \Lambda_{x^2}(w_i) + q(ih, t). \end{aligned} \quad (8.72)$$

In order to construct an implicit scheme, we take a regular mesh G_N . On this mesh, we define Eq. (8.46) in the form of three-layer difference scheme with weights (the Krenck-Nicholson method). We have

$$\alpha_j = \int_0^1 \{\Lambda_x^j(w_i)\}^2 dx,$$

$$\begin{aligned}
Z_i^k &= -\lambda \Lambda_{x^4}^k(w_i) + \{6\lambda\alpha - P_x(t)\} \Lambda_{x^2}^k(w_i), \\
&\frac{w_i^{j+1} - 2w_i^j + w_i^{j-1}}{\tau^2} + \varepsilon \frac{w_i^{j+1} - w_i^{j-1}}{2\tau} \\
&= \sigma Z_i^j + (1 - \sigma) Z_i^{j+1} + q(ih, t). \quad (8.73)
\end{aligned}$$

Superscripts (subscripts) correspond to layers in time (space). Time derivatives are approximated with accuracy of $O(\tau^2)$, whereas space derivatives are estimated with accuracy of $O(h^2)$, $O(h^4)$, $O(h^6)$. Computation of the coefficient α as well as boundary conditions is similar to the case of the explicit method. It should be noted that contrary to the explicit method, the integration in time is carried out not by the Runge–Kutta method, but rather via a solution to the linear equations. The system matrix is of a band type and its width depends on the approximation order of the derivatives $O(h^4)$ and $O(h^6)$. For approximation $O(h^2)$, the associated matrix has 5, 7 and 9 diagonals, respectively.

Computation of difference derivatives

Operators Λ_x , Λ_{x^2} , Λ_{x^4} can be estimated with various steps of applied approximation. In order to get formulas for difference derivatives, we apply the following program for symbolic computation in Maple environment.

Here we use the classical approach to find the difference derivatives. We define the dimension of a pattern required for interpolation of a given derivative with required accuracy. Then we construct the interpolating polynomial, and in the next step the obtained polynomial is differentiated by the required number of times. Finally, the polynomial value in the center of the pattern is computed. The following procedure is applied

$$\begin{aligned}
fd &:= proc(n, m) \\
&\quad locall, df; \\
l &:= floor(m/2) + floor((n-1)/2); \\
&\quad interp([seq(k * h, k = -l..l)], \\
&\quad [seq(y(k * h), k = -l..l)], x);
\end{aligned}$$

$$\begin{aligned}
df &:= simplify(subs(x = 0, diff(% , x\$n))); \\
&\quad print(df); \\
&\quad print(series(series(df, h, m + n), h, m)) \\
&\quad endproc
\end{aligned}$$

Here n denotes the order of a derivative, whereas m stands for the approximation order. It is clear that the dimension of the difference derivative is coupled with m and n in the following way

$$l = [m/2] + [(n-1)/2]. \quad (8.74)$$

A given maple-function not only yields a formula for the difference derivative, but also shows that approximation of the difference derivative corresponds to the given parameters. Application of symbolic computations essentially simplifies the process of routine type computations, and also allows to omit possible errors introduced by hand-made derivations.

We demonstrate this approach regarding the difference derivative computation of order $O(h^6)$. In what follows, the formulas for different orders of approximations are given.

For $O(h^2)$, we have

$$\left(\frac{\partial(\cdot)}{\partial x}\right) \approx \frac{1}{2h} [(\cdot)_{i+1} - (\cdot)_{i-1}] = \Lambda_x(\cdot) + O(h^2), \quad (8.75)$$

$$\left(\frac{\partial^2(\cdot)}{\partial x^2}\right)_i \approx \frac{1}{h^2} [(\cdot)_{i+1} - 2(\cdot)_i + (\cdot)_{i-1}] = \Lambda_{x^2}(\cdot) + O(h^2), \quad (8.76)$$

$$\begin{aligned}
\left(\frac{\partial^4(\cdot)}{\partial x^4}\right)_i &\approx \frac{1}{h^4} [(\cdot)_{i+2} - 4(\cdot)_{i+1} + 6(\cdot)_i - 4(\cdot)_{i-1} + (\cdot)_{i-2}], \\
&= \Lambda_{x^4}(\cdot) + O(h^2). \quad (8.77)
\end{aligned}$$

For $O(h^4)$, we have

$$\begin{aligned}
\left(\frac{\partial(\cdot)}{\partial x}\right)_i &\approx \frac{1}{12h} [(\cdot)_{i-2} - 8(\cdot)_{i-1} + 8(\cdot)_{i+1} - (\cdot)_{i+2}] \\
&= \Lambda_x(\cdot) + O(h^4), \quad (8.78)
\end{aligned}$$

$$\left(\frac{\partial^2(\cdot)}{\partial x^2}\right)_i \approx \frac{1}{12h^2} [(\cdot)_{i+2} + 16(\cdot)_{i+1} - 30(\cdot)_i + 16(\cdot)_{i-1} + (\cdot)_{i-2}]$$

$$= \Lambda_{x^2}(\cdot) + O(h^4), \quad (8.79)$$

$$\left(\frac{\partial^4(\cdot)}{\partial x^4}\right)_i \approx \frac{1}{h^4} [-(\cdot)_{i+3} + 12(\cdot)_{i+2} - 39(\cdot)_{i+1} + 56(\cdot)_i - 39(\cdot)_{i-1}$$

$$+ 12(\cdot)_{i-2} - (\cdot)_{i-3}] = \Lambda_{x^4}(\cdot) + O(h^4). \quad (8.80)$$

For $O(h^6)$ we have

$$\left(\frac{\partial(\cdot)}{\partial x}\right)_i \approx \frac{1}{60h} [(\cdot)_{i+3} - 9(\cdot)_{i+2} + 45(\cdot)_{i+1} - 45(\cdot)_{i-1}$$

$$+ 9(\cdot)_{i-2} - (\cdot)_{i-3}] = \Lambda_x(\cdot) + O(h^6), \quad (8.81)$$

$$\left(\frac{\partial^2(\cdot)}{\partial x^2}\right)_i \approx \frac{1}{180h^2} [2(\cdot)_{i+3} - 27(\cdot)_{i+2} + 270(\cdot)_{i+1} - 490(\cdot)_i$$

$$+ 270(\cdot)_{i-1} + 27(\cdot)_{i-2} + 2(\cdot)_{i-3}] = \Lambda_{x^2}(\cdot) + O(h^6), \quad (8.82)$$

$$\left(\frac{\partial^4(\cdot)}{\partial x^4}\right)_i \approx \frac{1}{240h^4} [7(\cdot)_{i+4} - 96(\cdot)_{i+3} + 676(\cdot)_{i+2} - 1952(\cdot)_{i+1}$$

$$+ 2730(\cdot)_i - 1952(\cdot)_{i-1} + 676(\cdot)_{i-2} - 96(\cdot)_{i-3} + 7(\cdot)_{i-4}]$$

$$= \Lambda_{x^4}(\cdot) + O(h^6). \quad (8.83)$$

As it can be seen from the reported formulas, the number of out-contour points increases with the approximation order increase: 1 — for $O(h^2)$, 2 — for $O(h^4)$, 3 — for $O(h^6)$.

In order to compute the partial derivatives, we may also apply a more general approach. Consider the following relation

$$b_0 f''(x-h) + b_1 f''(x) + b_2 f''(x+h)$$

$$\approx c_0 f(x-h) + c_1 f(x) + c_2 f(x+h). \quad (8.84)$$

We aim at finding coefficients $b_0, b_1, b_2, c_0, c_1, c_2$ such that the formula (8.84) is satisfied with the highest accuracy order.

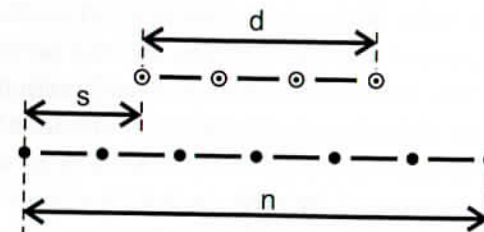


Fig. 8.4 Illustration of a Padé approximation parameters ($s = 3/2$, $d = 3$, $n = 7$).

Let $f(x) = e^{i\omega h}$, then we get

$$-\omega^2(b_0 e^{-i\omega h} + b_1 + b_2 e^{i\omega h})e^{i\omega h} \approx (c_0 e^{-i\omega h} + c_1 + c_2 e^{i\omega h})e^{i\omega h}. \quad (8.85)$$

We are going to find the mentioned coefficients in the neighborhood of $h = 0$. Taking into account $\xi = e^{i\omega h}$ ($\ln \xi = i\omega h$), we get

$$\left\{\frac{\ln \xi}{h}\right\}^2 \approx \frac{c_0 + c_1 \xi + c_2 \xi^2}{b_0 + b_1 \xi + b_2 \xi^2}. \quad (8.86)$$

Formula (8.86) implies that the best approximation in the neighborhood of $\xi = 1$ is yielded by the Padé approximation of the function $\left\{\frac{\ln \xi}{h}\right\}^2$ (see Fig. 8.4)

$$\left\{\frac{\ln \xi}{h}\right\}^2 \approx \frac{(\xi - 1)^2}{h^2(1 + (\xi - 1) + \frac{1}{12}(\xi - 1)^2)} = \frac{12 - 24\xi + 12\xi^2}{h^2(1 + 10\xi + \xi^2)}. \quad (8.87)$$

Parameters of Padé approximations ($s = 3/2$, $d = 3$ and $n = 7$).

The coefficients of implicit difference derivatives are defined by the following Maple-function:

```
with(numapprox);
implicid__fd := proc(n, m, s, d)
local t;
t := pade(x^s * ln(x)^m, x = 1, [n, d]) :
print(coeff(expand(denom(t)), x, i)$i = 0..d);
print(coeff(expand( numer(t)), x, i)/h^m $i = 0..n);
end proc
```


Here, m is the order of the derivative approximation; s is the pattern shift of derivatives; d is the dimension of the pattern derivatives (without 1); n is the dimension of the pattern functions (without 1).

For the explicit difference derivatives, the nominator of the Padé approximation has zero order ($d = 0$) and we may apply a simple Taylor series development. In other words, we have got one more way to estimate the coefficients of the difference derivatives. This is realized by the following Maple-function:

```
fd__ := proc(n, m)
local, df;
l := floor(m/2) + floor((n - 1)/2);
expand(convert(taylor(xl * ln(x)n, x = 1, 2 * l + 1), polynom));
df := simplify(sum(coef
    (% , x, i) * y((i - l) * h)/hn, i = 0..2 * l));
print(df);
print(series(series(df, h, m + n), h, m));
end proc
```

The latter function coincides in full with the classical approach function, and it may also serve for checking of the obtained difference derivative of given parameters. The problem of computations of partial derivatives can be studied from five different points of view:

- (i) *Interpolating approach.* Operator of a partial derivative is the exact derivative of an interpolating polynomial constructed on a certain pattern. This approach is widely used by spectral methods devoted to computations of partial derivatives.
- (ii) *Approximation of differential operators.* The operator of a partial derivative is defined by the finite difference approximation of a differential operator. This approach has been used for checking the results presented in earlier examples.
- (iii) *Correlation approach.* The differential operator can be considered as a correlating filter from the position of frequency filters with the appropriately chosen coefficients to approximate a partial derivative.

- (iv) *Multiplication by a Toeplitz matrix.* Computation of a partial derivative can be viewed algebraically, as the multiplication by a band matrix (Toeplitz matrix). This approach plays the fundamental role while constructing implicit schemes.
- (v) *Spectral methods.* This method is based on the Fourier series. Operator for a partial derivative is presented as an inverse Fourier transformation regarding a direct discrete Fourier transformation and the properly defined coefficients. This approach can be generalized into an arbitrary basis of a space of continuous functions.

However, introduced approximations to continuous differential equations by the difference equations imply a modification of the physical properties of an investigated system. From the point of view of dispersive and diffusion properties, the continuous and discrete solutions are not fully equivalent. This is why we require adequate information on the modification of solutions introduced by discretization. This problem can be solved with the theory of digit filters.

Let us consider the difference approximations of space derivatives from the point of view of the digital filters. They can be classified as linear stationary non-recursive filters. One of the important characteristics of a digital filter is the transition function characterizing the ratio of an output complex signal amplitude and an input complex signal amplitude. In our case for differentiation of a spatial derivative, we deal with the relation of discrete and continuous dispersion. The continuous rule of dispersion should be negligibly perturbed in order to keep possibly "flat" transition function.

We consider an action of the difference operator regarding the fourth derivative using different approximation orders on a harmonic signal. Substituting the harmonic input $w(x) = e^{i\omega x}$ into Eqs. (8.77), (8.80), (8.83), after trigonometric transformations, and division by the dispersion term $\omega^4 e^{i\omega x}$, the following transition functions corresponding to the applied operators of digital filters are obtained

$$\eta_2 = 4 \frac{\cos^2(\pi\varphi) - 2\cos(\pi\varphi) + 1}{\pi^4 \varphi^4}, \quad (8.88)$$

$$\eta_4 = -\frac{4 \cos^3(\pi\varphi) - 6 \cos^2(\pi\varphi) + 9 \cos(\pi\varphi) - 4}{3 \pi^4 \varphi^4}, \quad (8.89)$$

$$\eta_6 = \frac{1}{15} \times \frac{7 \cos^4(\pi\varphi) - 48 \cos^3(\pi\varphi) + 1626 \cos^2(\pi\varphi) - 208 \cos(\pi\varphi) + 87}{\pi^4 \varphi^4}. \quad (8.90)$$

The latter relations have been obtained with the help of the following Maple-function:

```
fd_filter := proc(n, m)
local, df;
l := floor(1/2 * m) + floor(1/2 * n - 1/2);
expand(convert(taylor(xl * ln(x)n, x = 1, 2 * l + 1), polynom));
simplify(sum(coeff(%, x, i) * exp(I * (i - l) * h) / hn,
i = 0..2 * l)) / In;
subs(h = Pi * phi, %)
endproc
```

In the above n is the derivative order, whereas m denotes the approximation order.

In Fig. 8.5, graphs of transition functions of digital filters corresponding to operators (8.77), (8.80), (8.83) are reported. Drawings are given in interval $[0, 1]$, where 0 corresponds to zero frequency, and 1 is the Nyquist frequency $\omega = \pi/h$.

Figure 8.5 shows that for all approximations the transition function is strongly damped in high frequencies interval. However, the transition function of the operator L_4 possesses more "flat" profile than L_2 , i.e. it perturbs less the continuous dispersion rule, in particular on low frequencies, where the fundamental energy localization is expected.

It is clear that the operator L_6 differs from L_4 rather marginally, and hence in many applications we may use L_4 .

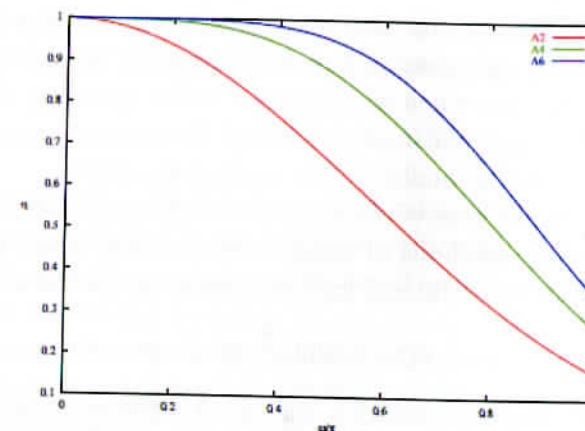


Fig. 8.5 Transition functions for the fourth difference derivative with different approximations.

Approximation of functions and their derivatives on a mesh

From a historical point of view, the fundamental method of investigation of partial differential equations is associated with the use of explicit difference schemes of low orders. These methods are universal and have simple realization. Even today they are used to a general picture of the PDEs behavior, to find the direction of further investigations that emphasize on requirements regarding accuracy, stability and computational speed. Difference schemes are simple in realizations and they can be easily adapted to various forms of the initial and boundary conditions. The latter property is of a particular importance in comparison to the Bubnov-Galerkin approach which depends essentially on the applied boundary conditions. Since the computation of the difference derivatives is carried on a certain narrow mesh interval, the computed values of the derivatives depend only on the values of the neighborhood mesh nodes. It is tempting to expect that the increase in the approximation order and the increase in the difference pattern should solve the problem of localization, but it leads to other problems related to computation requirements. Errors associated with digital accuracy increase, as well as the occurrence of computational complexity.

The validity, reliability and quality estimation of the numerical solution requires a rigorous definition of errors in the computational methods. In the case when we look for a scalar quantity, the estimation of absolute and relative errors allows for adequate monitoring of the evaluation of the quality of the applied algorithm.

However, in the case when a function is the solution, there exist a few alternative methods of error computations, based on various norms. If the error on interval $[a, b]$ is defined in the following way

$$e(x) = \tilde{w}(x) - w(x), \quad (8.91)$$

where $w(x)$ is the exact solution, and $\tilde{w}(x)$ is the numerical solution, then in practice the following definitions of norms are applied

$$\|e\|_{\infty} = \max_{a \leq x \leq b} |e(x)|, \quad (8.92)$$

$$\|e\|_1 = \int_a^b |e(x)| dx, \quad (8.93)$$

$$\|e\|_2 = \sqrt{\int_a^b e(x)^2 dx}. \quad (8.94)$$

All those definitions are particular cases of the so-called p -norm defined as follows

$$\|e\|_p = \sqrt[p]{\int_a^b |e(x)|^p dx}. \quad (8.95)$$

In the case when the numerical solution is in the form of a mesh function, we must compare it with the exact solution. The following vector of errors is introduced

$$e_i = w_i - w(x_i), \quad (8.96)$$

which allows for numerical error estimation with respect to an arbitrarily chosen norm. However, an arbitrary vector norm may increase while increasing the number of mesh points, which can yield erroneous results regarding estimation of the error order.

In order to remove the mentioned drawback one may discretize one of the norms (8.92)–(8.94), for example, in the following way

$$\|e\|_1 = h \sum_a^b |e(x)|. \quad (8.97)$$

Writing programs realizing one of the numerical methods devoted to finding a solution to PDEs requires verification and validation of the applied algorithm and its realization. There are a few approaches to solve the mentioned problem.

In the case when the exact solution of a given problem is known for some initial and boundary conditions, this solution allows not only for validations of the correctness of the written program, but it also allows to follow asymptotic evolution of the error, and even to define a constant of the known asymptotics. Let us assume that we know the exact solution $w(x)$ to a problem. Carrying out the numerical solution on the introduced mesh with step h , we find an approximating solution \tilde{w}^h .

The following error function is introduced:

$$E(h) = \|\tilde{w}^h - w^h\|. \quad (8.98)$$

If the used method has an approximation order p , we may expect that

$$E(h) = Ch^p + O(h^p). \quad (8.99)$$

Then we decrease the step twice to get

$$E(h/2) = \frac{Ch^p}{2^p}, \quad (8.100)$$

and hence

$$\frac{E(h)}{E(h/2)} = 2^p, \quad (8.101)$$

$$p = \log_2 \frac{E(h)}{E(h/2)}. \quad (8.102)$$

Knowing p , one may define the constant of asymptotics of the method:

$$C = E(h)/h^p. \quad (8.103)$$

Therefore, having in hand the exact solution, two series of computations allow to define both order and constant of the asymptotic

method. Even if we monitor a “good behavior” of the numerical solution it is worthy to carry out other computations on a more dense mesh, in order to follow a proper asymptotic error evolution. The latter method allows to exhibit certain small errors introduced while writing a program code.

In the case when the exact solution is not known, one may try to simplify the problem, and in the beginning to solve the counterpart simplified mathematical model, for which the exact solution is known. The latter approach, though not fully sufficient, allows to discover introduced errors in the initial step of the algorithm. Besides, introduction of more dense mesh yields a good estimation of computational errors. Let us assume that we have carried out two series of computations with steps h and $h/2$. Then, taking the solution associated with the dense mesh as exactly one, we get

$$\begin{aligned}\tilde{E}(h) &= \|w^h - w^{h/2}\| = \|w^h - \tilde{w}^h\| + \|\tilde{w}^h - w^{h/2}\| \\ &= E(h) + O\left(\left(\frac{h}{2}\right)^p\right).\end{aligned}\quad (8.104)$$

In other words, the latter approach yields very good approximation of the errors introduced by the applied method. It should be noted, however, that the obtained numerical solution may converge to a function which, in principle, has no relation to the real searched solution.

8.1.3 Solving ODEs in time

Consider a problem with initial conditions

$$y'(t) = f(t, y(t)), \quad y(t_0) = y_0, \quad (8.105)$$

where function $f: [t_0, \infty) \times \mathbb{R}^d \rightarrow \mathbb{R}^d$, and $y_0 \in \mathbb{R}^d$ is a given vector.

The so far stated problem is called the Cauchy problem and, owing to the theorem on existence and uniqueness of the solution to an ordinary differential equation, the solution does exist and it is unique [Hairer *et al.* (1993)]. In order to solve numerically the formulated problem, a series of methods have been developed, but the more popular and useful are the Runge–Kutta methods. There exist

boundary values problems, where the solution values are given in a few points, and they require special methods like shooting, finite differences and collocation. One may say that it is sufficient to solve differential equations of the first-order. Equations of higher order can be reduced to the first-order ODEs by introduction of additional variables. For instance, the second-order equation $y'' = -y$ can be presented in the form of two equations of the first-order: $y' = z$ and $z' = -y$.

8.1.3.1 Euler's method

In Eq. (8.105), we substitute y' by the following difference approximation

$$y'(t) \approx \frac{y(t+h) - y(t)}{h}. \quad (8.106)$$

Hence, the following formula is obtained

$$y(t+h) \approx y(t) + hf(t, y(t)). \quad (8.107)$$

The given formula is applied in the following way. We take the integration step h and we consider a series of time instants $t_0, t_1 = t_0 + h, t_2 = t_0 + 2h, \dots$. By y_n , we denote numerical approximation to the exact solution $y(t_n)$. Owing to formula (8.107), we compute successive approximations to the exact solution via the following recursive scheme

$$y_{n+1} = y_n + hf(t_n, y_n). \quad (8.108)$$

The obtained equation presents the Euler method, proposed in 1798 by L. Euler [Hairer *et al.* (1993)]. Observe that Eq. (8.106) can be also presented in the following way

$$y'(t) \approx \frac{y(t) - y(t-h)}{h}. \quad (8.109)$$

In this case, we deal with the so-called implicit Euler method

$$y_{n+1} = y_n + hf(t_{n+1}, y_{n+1}). \quad (8.110)$$

In the latter approach, it is necessary to solve the equation of type (8.110) on each computation step, and this method is implicit. It can be solved also by the Newton method [Hairer and Wanner (1996)]. It

is obvious that in this case each computational step requires essentially more time in comparison to the explicit method.

In many cases, the Euler method does not have high accuracy, and mathematicians have developed methods of higher order accuracy. It is clear that in order to compute successive values, one may use not only one value from the previous computational step, but also the whole series of the previously obtained values. In practice, all multi-step methods belong to a family of linear multi-step methods, and can be presented in the following form

$$\begin{aligned} \alpha_k y_{n+k} + \alpha_{k-4} y_{n+k-4} + \cdots + \alpha_0 y_n \\ = h(\beta_k f(t_{n+k}, y_{n+k}) + \beta_k f(t_{n+k-1}, y_{n+k-1}) \\ + \cdots + \beta_k f(t_n, y_n)) \end{aligned} \quad (8.111)$$

where α_k, β_k are certain constants. The latter approach yields a series of the Runge–Kutta methods in memory of Karl Runge and Martin Kutta [Hairer and Wanner (1996)]. Mostly known and used is obviously the fourth-order Runge–Kutta (RK4) method.

8.1.3.2 Runge–Kutta methods

We are looking for a solution to problem (8.105) in points $\{t_i\}_0^N$. Then the following formula holds

$$y_{n+1} = y_i + \int_{t_i}^{t_{i+1}} f(t, y(t)) dt. \quad (8.112)$$

We compute the integral using the trapezoid method: $\int_{t_i}^{t_{i+1}} f(t, y(t)) dt = \frac{1}{2} h(f(t_i, y_i) + f(t_{i+1}, y_{i+1}))$. Owing to Euler's formula, we have: $y_{i+1} = y_i + hf(t_i, y_i)$. Therefore, we get

$$y_{i+1} = y_i + \frac{1}{2} h(f(t_i, y_i) + f(t_{i+1}, y_i + hf(t_i, y_i))). \quad (8.113)$$

The method based on formula (8.113) is called the modified Euler method. However, in fact this is the second-order Runge–Kutta (RK2) method. It can be verified describing a solution $y(t)$ in the

vicinity of y_i in the form of the Taylor series up to the terms of order $O(h^3)$:

$$\begin{aligned} y_{i+1} &= y_i + hy'_i + \frac{1}{2} h^2 y''_i + O(h^3) \\ &= y_i + hf(t_i, y_i) + \frac{1}{2} h^2 f'(t_i, y_i) + O(h^3) \\ &= y_i + hf(t_i, y_i) + \frac{1}{2} h^2 (f'_x(t_i, y_i) + f'_y(t_i, y_i) y'_i) + O(h^3) \\ &= y_i + hf(t_i, y_i) \\ &\quad + \frac{1}{2} h^2 (f'_x(t_i, y_i) + f'_y(t_i, y_i) f(t_i, y_i)) + O(h^3). \end{aligned} \quad (8.114)$$

The right-hand side of (8.113) is also developed into Taylor's series:

$$\begin{aligned} y_{i+1} &= y_i + \frac{1}{2} h [f(t_i, y_i) + f(t_{i+1}, y_i + hf(t_i, y_i))] \\ &= y_i + \frac{1}{2} h [f(t_i, y_i) + f(t_i, y_i) + hf'_x(t_i, y_i) \\ &\quad + hf'_y(t_i, y_i) f(t_i, y_i) + O(h^2)] \\ &= y_i + hf(t_i, y_i) + \frac{h^2}{2} (f'_x(t_i, y_i) \\ &\quad + f'_y(t_i, y_i) f(t_i, y_i)) + O(h^3). \end{aligned} \quad (8.115)$$

Comparison of right-hand side of Eqs. (8.114) and (8.115) proves that the modified Euler's method is the RK2.

In Eq. (8.112), we compute the integral by the method of rectangulars $\int_{t_i}^{t_{i+1}} f(t, y(t)) dt = \frac{1}{2} h(f(t_i + \frac{h}{2}, y(t_i + \frac{h}{2})))$. Owing to the Euler formula, we have $y(t_i + \frac{h}{2}) = y_i + \frac{h}{2} f(t_i, y_i)$, and hence

$$y_{i+1} = y_i + hf\left(t_i + \frac{1}{2}h, y_i + \frac{1}{2}hf(t_i, y_i)\right). \quad (8.116)$$

The method based on formula (8.116) is known as the improved Euler method. We show that the latter method also coincides with the Taylor series (8.114) up to the terms of the second-order. We

have

$$\begin{aligned}
 y_{i+1} &= y_i + \frac{1}{2}hf(t_i + \frac{1}{2}h, y_i + \frac{1}{2}hf(t_i, y_i)) \\
 &= y_i + h \left[f(t_i, y_i) + \frac{1}{2}hf'_x(t_i, y_i) \right. \\
 &\quad \left. + \frac{1}{2}hf'_y(t_i, y_i)f(t_i, y_i) + O(h^2) \right] \\
 &= y_i + hf(t_i, y_i) + \frac{1}{2}h^2 [f'_x(t_i, y_i) + f'_y(t_i, y_i)f(t_i, y_i)] + O(h^3),
 \end{aligned} \tag{8.117}$$

and hence we have proved that in fact this is the RK2 method.

In general, the following RK2 method and the following generalized formula are used

$$\begin{aligned}
 y_{i+1} &= y_i + \frac{1}{2}h(f(t_i, y_i) + f(t_{i+1}, y_i + hf(t_i, y_i))), \\
 y_{i+1} &= y_i + hf \left(t_i + \frac{1}{2}h, y_i + \frac{1}{2}hf(t_i, y_i) \right),
 \end{aligned} \tag{8.118}$$

which yields

$$y_{i+1} = y_i + \alpha hf(t_i, y_i) + bhf(t_i + \alpha h, y_i + \beta hf(t_i, y_i)), \tag{8.119}$$

and it can be reduced either to the modified Euler method ($a = 0, b = 1, \alpha = \frac{1}{2}, \beta = \frac{1}{2}$) or to the improved Euler method ($a = \frac{1}{2}, b = \frac{1}{2}, \alpha = 1, \beta = 1$).

The latter formula can be generalized for higher order approximations:

$$\begin{cases} k_1(h) = hf(t_i, y_i), \\ k_2(h) = hf(t_i + \alpha_2 h, y_i + \beta_{21}k_1(h)), \\ \dots \\ k_q(h) = hf(t_i + \alpha_q h, y_i + \beta_{q1}k_1(h) + \dots + \beta_{qq-1}k_{q-1}(h)), \\ y_{i+1} = y_i + \sum_{i=1}^q p_i k_i(h). \end{cases} \tag{8.120}$$

All Runge-Kutta methods are described by formulas (8.120). However, not all formulas yielded by (8.120) define the Runge-Kutta methods. Important question arises: How to choose parameters α, β and p to get a Runge-Kutta method of the given order s ?

The stated question will be solved using an example of the third Runge-Kutta method. Taking $q = s = 3$, the following formula is obtained

$$\begin{cases} k_1(h) = hf(t_i, y_i), \\ k_2(h) = hf(t_i + \alpha_2 h, y_i + \beta_{21}k_1(h)), \\ k_3(h) = hf(t_i + \alpha_3 h, y_i + \beta_{31}k_1(h) + \beta_{32}k_2(h)), \\ y_{i+1} = y_i + p_1k_1(h) + p_2k_2(h) + p_3k_3(h). \end{cases} \tag{8.121}$$

We develop all terms of the right hand part of (8.121) into the Taylor series up to h^3 order, and we get

$$\begin{cases} k_1(h) = hf(t_i, y_i) \\ k_2(h) = hf(t_i + \alpha_2 h, y_i + \beta_{21}k_1(h)) = h[f + h(f'_x \alpha_2 + f'_y \beta_{21}f) \\ \quad + \frac{1}{2!}h^2(f''_{xx}\alpha_2^2 + f''_{xy}\alpha_2\beta_{21}f + f''_{yy}\beta_{21}^2f^2) + O(h^3)] \\ k_3(h) = hf(t_i + \alpha_3 h, y_i + \beta_{31}k_1(h) + \beta_{32}k_2(h)) = h[f + f'_x \alpha_3 h \\ \quad + f'_y \{\beta_{31}hf + \beta_{32}h(f + f'_x \alpha_2 h + f'_y \beta_{21}hf)\} \\ \quad + \frac{1}{2!}h^2(f''_{xx}\alpha_3^2 + 2f''_{xy}\alpha_3(\beta_{31} + \beta_{32})f \\ \quad + f''_{yy}(\beta_{31} + \beta_{32})^2f^2) + O(h^3)] \\ y_{i+1} = y_i + p_1k_1 + p_2k_2 + p_3k_3. \end{cases} \tag{8.122}$$

On the other hand, developing $y(t)$ in a vicinity of point t_i into Taylor series up to terms of order h^3 , the following formula is obtained

$$y_{i+1} = y_i + hy'_i + \frac{1}{2}h^2(f'_x + f'_y f) + \frac{1}{6}h^3(f'_x + f'_y f)' + O(h^4)$$

$$= y_i + fh + \frac{1}{2}h^2(f'_x + f'_y f) + \frac{1}{6}h^3(f''_{xx} + 2f''_{xy}f + f''_{yy}f^2 + f'_x f'_y + (f'_y)^2 f) + O(h^4). \quad (8.123)$$

We compare the coefficients standing by h , h^2 , h^3 , and we get

$$\begin{aligned} h: p_1 f + p_2 f + p_3 f &= f, \\ h^2: p_2 (f'_x \alpha_2 + f'_y \beta_{21} f) + p_3 (f'_x \alpha_3 + f'_y (\beta_{31} + \beta_{32}) f) \\ &= \frac{1}{2} (f'_x + f'_y f), \\ h^3: \frac{1}{2} p_2 [f''_{xx} \alpha_2^2 + 2f''_{xy} \alpha_2 \beta_{21} f + f''_{yy} \beta_{21}^2 f^2] \\ &\quad + p_3 \left[f'_y \beta_{32} (f'_x \alpha_2 + f'_y \beta_{21} f) \right. \\ &\quad \left. + \frac{1}{2} \{ f''_{xx} \alpha_3^2 + 2f''_{xy} \alpha_3 (\beta_{31} + \beta_{32}) f \right. \\ &\quad \left. + f''_{yy} (\beta_{31} + \beta_{32})^2 f^2 \} \right] \\ &= \frac{1}{6} (f''_{xx} + 2f''_{xy} f + f''_{yy} f^2 + f'_x f'_y + (f'_y)^2 f). \end{aligned} \quad (8.124)$$

We carry out the same operation, but this time with respect to other coefficients:

$$\begin{aligned} f: p_1 + p_2 + p_3 &= 1, \\ f'_x: p_2 \alpha_2 + p_3 \alpha_3 &= \frac{1}{2}, \\ f'_y f: p_2 \beta_{21} + p_3 (\beta_{31} + \beta_{32}) &= \frac{1}{2}, \\ f'_y f: p_2 \beta_{21} + p_3 (\beta_{31} + \beta_{32}) &= \frac{1}{2}, \\ f''_{xx}: \frac{1}{2} p_2 \alpha_2^2 + \frac{1}{2} p_3 \alpha_3^2 &= \frac{1}{6}, \end{aligned} \quad (8.125)$$

$$\begin{aligned} f''_{yy} f: p_2 \beta_{21} + \frac{1}{2} p_3 (\beta_{31} + \beta_{32}) &= \frac{1}{3}, \\ f''_{yy} f^2: \frac{1}{2} p_2 \beta_{21}^2 + \frac{1}{2} p_3 (\beta_{31} + \beta_{32})^2 &= \frac{1}{6}, \\ f'_x f'_y: \frac{1}{2} p_3 \alpha_2 \beta_{32} &= \frac{1}{6}, \\ (f'_y)^2 f: \frac{1}{2} p_3 \beta_{32} \beta_{21} &= \frac{1}{6}. \end{aligned}$$

We have got eight equations, but only six of them are linearly independent. We take β_{21} and β_{32} as parameters, and the remaining parameters are derived in the following form

$$\begin{aligned} \alpha_2 &= \beta_{21}, \quad \alpha_3 = \frac{\alpha_2}{2} \pm \sqrt{\frac{\alpha_2^2}{4} - \frac{1}{p_3} \left(\frac{\alpha_2}{2} - \frac{1}{3} \right)}, \\ p_1 &= 1 - (p_2 + p_3), \quad p_2 = \frac{1}{p_3} \left(\frac{1}{2} - p_2 \beta_{21} \right) - \beta_{32}, \quad p_3 = \frac{1}{6\beta_{32}\beta_{21}}, \end{aligned} \quad (8.126)$$

Therefore, an infinite set of solutions depending on the choice of free variables β_{21} and β_{32} is obtained. It is suitable to take rational coefficients, therefore, the most popular RK3 method is that with $\beta_{21} = \frac{1}{2}$ and $\beta_{32} = 2$. Hence, $\alpha_2 = \frac{1}{2}$, $p_3 = \frac{1}{6}$, $\alpha_3 = 1$, $p_2 = \frac{2}{3}$, $\beta_3 = -1$, $p_1 = \frac{1}{6}$. It means that the following one-step formula is obtained:

$$\begin{aligned} k_1 &= f(t_i, y_i), \\ k_2 &= hf \left(t_i + \frac{1}{2}h, y_i + \frac{1}{2}k_1 \right), \\ k_3 &= hf(t_i + h, y_i - k_1 + 2k_2), \\ y_{i+1} &= y_i + \frac{1}{6}k_1 + \frac{2}{3}k_2 + \frac{1}{6}k_3 + O(h^4). \end{aligned} \quad (8.127)$$

The so far described technique can be applied to find formulas with higher order approximations. We rewrite the most popular

and widely used Runge-Kutta methods [Abramowitz and Stegun (1978)]:

Alternative RK3 method

$$\begin{aligned} k_1 &= f(t_i, y_i), \\ k_2 &= hf \left(t_i + \frac{1}{3}h, y_i + \frac{1}{3}k_1 \right), \\ k_3 &= hf \left(t_i + \frac{2}{3}h, y_i + \frac{2}{3}k_2 \right), \\ y_{i+1} &= y_i + \frac{1}{4}k_1 + \frac{3}{4}k_3 + O(h^4). \end{aligned} \quad (8.128)$$

Classical RK4 method

$$\begin{aligned} k_1 &= f(t_i, y_i), \\ k_2 &= hf \left(t_i + \frac{1}{2}h, y_i + \frac{1}{2}k_1 \right), \\ k_3 &= hf \left(t_i + \frac{1}{2}h, y_i + \frac{1}{2}k_2 \right), \\ k_4 &= hf(t_i + h, y_i + k_3), \\ y_{i+1} &= y_i + \frac{1}{6}k_1 + \frac{1}{3}k_2 + \frac{1}{3}k_3 + \frac{1}{6}k_4 + O(h^5). \end{aligned} \quad (8.129)$$

Improved RK4 method

$$\begin{aligned} k_1 &= f(t_i, y_i), \\ k_2 &= hf \left(t_i + \frac{1}{3}h, y_i + \frac{1}{3}k_1 \right), \\ k_3 &= hf \left(t_i + \frac{2}{3}h, y_i - \frac{1}{3}k_1 + k_2 \right), \\ k_4 &= hf(t_i + h, y_i + k_1 - k_2 + k_3), \\ y_{i+1} &= y_i + \frac{1}{8}k_1 + \frac{3}{8}k_2 + \frac{3}{8}k_3 + \frac{1}{8}k_4 + O(h^5). \end{aligned} \quad (8.130)$$

Runge-Kutta Cash-Karp method [RKCK]

$$k_1 = f(t_i, y_i),$$

$$k_2 = hf \left(t_i + \frac{1}{5}h, y_i + \frac{1}{5}k_1 \right), \quad (8.131)$$

$$k_3 = hf \left(t_i + \frac{3}{10}h, y_i + \frac{3}{40}k_1 + \frac{9}{40}k_2 \right),$$

$$k_4 = hf \left(t_i + \frac{3}{5}h, y_i + \frac{3}{10}k_1 - \frac{9}{10}k_2 + \frac{6}{5}k_3 \right),$$

$$k_5 = hf \left(t_i + h, y_i - \frac{11}{54}k_1 + \frac{5}{2}k_2 - \frac{70}{27}k_3 + \frac{35}{27}k_4 \right),$$

$$\begin{aligned} k_6 &= hf \left(t_i + \frac{7}{8}h, y_i + \frac{1631}{55296}k_1 + \frac{175}{512}k_2 + \frac{575}{13824}k_3 \right. \\ &\quad \left. + \frac{44275}{110592}k_4 + \frac{253}{4096}k_5 \right), \end{aligned}$$

$$y_{i+1} = y_i + \frac{37}{378}k_1 + \frac{250}{621}k_3 + \frac{125}{594}k_4 + \frac{512}{1771}k_6 + O(h^6).$$

Fehlberg method [RK45]

$$k_1 = f(t_i, y_i),$$

$$k_2 = hf \left(t_i + \frac{1}{4}h, y_i + \frac{1}{4}k_1 \right),$$

$$k_3 = hf \left(t_i + \frac{3}{8}h, y_i + \frac{3}{32}k_1 + \frac{9}{32}k_2 \right),$$

$$k_4 = hf \left(t_i + \frac{12}{13}h, y_i + \frac{1932}{2197}k_1 - \frac{7200}{2197}k_2 + \frac{7296}{2197}k_3 \right),$$

$$k_5 = hf \left(t_i + h, y_i + \frac{8341}{4104}k_1 - \frac{32832}{4104}k_2 + \frac{29440}{4104}k_3 - \frac{845}{4104}k_4 \right),$$

$$\begin{aligned} k_6 &= hf \left(t_i + \frac{1}{2}h, y_i - \frac{6080}{20520}k_1 + \frac{41040}{20520}k_2 - \frac{28352}{20520}k_3 \right. \\ &\quad \left. + \frac{9295}{20520}k_4 - \frac{5643}{20520}k_5 \right), \end{aligned}$$

$$y_{i+1} = y_i + \frac{1}{7618050}(902880k_1 + 3953664k_3 + 3855735k_4 - 1371249k_5 + 277020k_5) + O(h^6). \quad (8.132)$$

It should be emphasized that there exist even higher order Runge–Kutta methods. For example, the Prince–Dormand method is nothing but the RK8PD method [Bader and Deuffhard (1983)]. For this method, $q = 13$ and computational complexity of one-step in time is much higher than while applying low order Runge–Kutta methods. The increase in the integration step does not play a crucial role, and hence in majority of applications the methods with high order approximations attract attention rather from a purely scientific side, since they do not give any essential benefits from the point of view of computations.

8.1.3.3 Results obtained by different order Runge–Kutta methods

Since we have a set of various Runge–Kutta methods, a question appears as to which one among them is the most effective to solve our problem. In order to get an answer, we compare the results obtained by different methods with different integration steps in time. We study a solution to problem (8.46) with boundary initial conditions (8.47) solved with the FDM with difference derivatives of order $O(h^4)$. We compute parametric vibrations of the beam-strip subjected to harmonic excitation $P_x(t) = P_0 \sin(\omega_0 t)$, where $\omega_0 = 3$ is the frequency closely located to the fundamental beam frequency. Amplitude of excitation is chosen in a way that the vibrations are regular $P_0 = 2.5$. As a pattern result, we take that of the RK8PD method with the integration step $dt = 2^{-13}$.

Since during vibrations a stable regime has been observed, it was possible to get the case when stationary vibrations coincide with the pattern with accuracy up to a sign. Therefore, instead of trajectories, the frequency power spectra, i.e. integral characteristics, should be compared.

In Fig. 8.6, a comparison of the beam-strip center vibrations and frequency power spectra for numerical integrations of the RK2 and RK8 method, is given. Stationary vibrations coincide up to the sign,

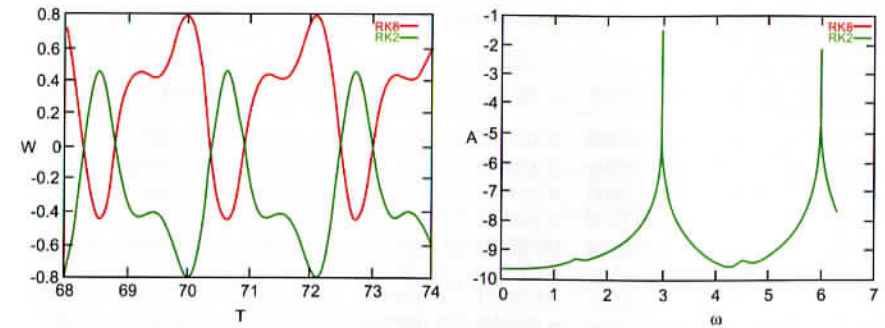


Fig. 8.6 Comparison of the beam-strip center point vibrations and frequency power spectra for different Runge–Kutta methods.

Table 8.1 Error of integration of simply supported beam via different Runge–Kutta methods in %, formula (8.125).

DT	RK2	RK2IMP	RK4	RK4IMP	RKF45	RKCK	RK8PD
2^{-8}	0.054002	0.056899	0.053990	0.053990	∞	∞	0.053989
2^{-9}	0.026166	0.026890	0.026164	0.026164	0.026164	0.026164	0.026164
2^{-10}	0.012219	0.012400	0.012219	0.012219	0.012219	0.012219	0.012219
2^{-11}	0.005240	0.005284	0.005240	0.005240	0.005240	0.005240	0.005240
2^{-12}	0.001748	0.001759	0.001748	0.001748	0.001748	0.001748	0.001748

whereas frequency power spectra coincide with the accuracy up to a constant component (zero frequency). Power spectra have been truncated up to frequency $2.1\omega_0$, and the relative errors for all methods in comparison to the pattern result have been computed. In Table 8.1 comparison of the relative error for different Runge–Kutta methods and different time steps has been carried out. The following notation has been used: *RK2* is the modified Euler method (RK2 second-order Runge–Kutta method); *RK2IMP* is the improved Euler method (RK2 second-order Runge–Kutta method), formula (8.115); *RK4* is the classical fourth-order Runge–Kutta RK4 method, formula (8.129); *RK4IMP* is the improved RK4 fourth-order Runge–Kutta method, formula (8.130); *RKF45* is the Fehlberg method (fifth-order Runge–Kutta method), formula (8.132); *RKCK* is the Cash–Karp method (fifth-order Runge–Kutta method), formula (8.131); *RK8PD* is the Prince–Dormand method (eight-order Runge–Kutta method).

Table 8.2 Errors introduced by integration of \cos via different Runge-Kutta methods in %.

DT	RK2	RK2IMP	RK4	RK4IMP	RKF45	RKCK	RK8PD
2^{-2}	9.499220	10.164300	9.461320	9.461320	13.477200	0.991611	1.522040
2^{-3}	10.149400	11.566600	7.976540	7.976540	0.532819	0.604951	0.636559
2^{-4}	7.148090	19.016600	0.834543	0.834543	0.285462	0.288984	0.289736
2^{-5}	1.016780	17.917600	0.148066	0.148066	0.137571	0.137675	0.137695
2^{-6}	0.158051	9.929830	0.067255	0.067255	0.066866	0.066869	0.066870
2^{-7}	0.042727	3.145560	0.032769	0.032769	0.032748	0.032748	0.032748
2^{-8}	0.017180	0.850096	0.016011	0.016011	0.016010	0.016010	0.016010
2^{-9}	0.007865	0.218204	0.007722	0.007722	0.007722	0.007722	0.007722
2^{-10}	0.03615	0.055427	0.003598	0.003598	0.003598	0.003598	0.003598
2^{-11}	0.001543	0.014103	0.001541	0.001541	0.001541	0.001541	0.001541
2^{-12}	0.000514	0.003573	0.000513	0.000513	0.000513	0.000513	0.000513

The carried out numerical experiments show that the numerical scheme is unstable for the time step $dt = 2^{-7}$ for all methods. Furthermore, the table implies that the numerical algorithm is divergent also for $dt = 2^{-8}$ for the Fehlberg and Cash-Karp methods. The obtained results show that the obtained error practically does not depend on the method used but it depends on the chosen time step. This is motivated by a complex part of the right-hand side of the integrated differential equations, and in result by the multi-mode vibrational regimes.

For comparison purpose, in Table 8.2 a similar comparison of results for the integration of differential Eq. (8.133) is conducted, whose solution is the function $y(t) = \cos(t)$:

$$y''(t) = -y(t), \quad y(0) = 0, \quad y'(0) = 1. \quad (8.133)$$

Right-hand side of this differential equation is very simple and does not introduce any errors into the numerical scheme. Resultant function has very simple form of one-frequency oscillator. Numerical scheme is sufficiently stable and does not diverge even if large time steps are applied. Here, we clearly see the advantage of the Runge-Kutta methods of higher orders. Observe also that the improved Euler's method is more suitable for computation compared to the modified Euler method though both have the same approximation order. It is clear that the improved Euler method yields reliable

results for steps less than $dt = 2^{-8}$, whereas the modified Euler method exhibits computational error of 1% for the step $dt = 2^{-5}$.

After getting the required approximation, further increase in accuracy does not introduce any qualitative changes into the results. Therefore, a key role in the choice of a method of integration plays not only on its computational accuracy, but also on its computational complexity, i.e. the time needed to achieve reliable results. In the model problem of integration of Eq. (8.133) via the Cash-Karp method we deal with the smallest error, and the duration of computational results is only 15% slower than the (fastest) modified Euler method. It is obvious that the Cash-Karp method is more suitable to solve this problem since already for the step $dt = 2^{-2}$ the error is less than 1%. Therefore, owing to the choice of a sufficiently large computational step, the given method essentially overcomes the modified Euler's method from the point of view of computational complexity.

However, the so far obtained results are not applicable to the problem of vibrations of the beam-strip. Errors of all methods are in practice equal for equal steps. The remaining methods give reliable results with an error of 0.5%. For the given problem, the modified Euler method is remarkable owing to its simplicity. Contrary to the studied model problem, in our case the majority of computational time deals with the computation of the right-hand side of the differential equation. In this case, for the same time step, the Runge-Kutta methods of higher order require a few times longer computational time than the modified Euler method. One time step in the modified Euler method requires three times computations of the right-hand side of the equation, whereas computations carried out by the improved Euler method, RK4 method, RK4IMP method, Fehlberg method and Cash-Carp method requires 4, 4, 7, 6 and 13 times, respectively. For the model's problem, computation of the right-hand side has been carried out practically at once, therefore the higher order methods require typically 15% more computation time. In the case of analysis of the beam-strip vibration, the Cash-Karp method is beaten by the modified Euler method in two times. Reported results of the remaining methods have been

used only to compare and estimate the reliability of the obtained results.

8.1.4 LE

8.1.4.1 Computation of the LEs spectrum

The LEs play an important role in the theory of dissipative dynamical systems. They allow to compute a quantitative measure of chaotization. Besides, there is a link between LEs and other characteristics of the chaotization, like the Kolmogorov entropy and the dynamical dimension. The theory of LEs has been developed by Oseledec [Oseledec (1968)]. Here, we aim at presenting relations between LEs and mechanical vibrations of structural members.

Linkage between LEs and Kolmogorov entropy has been studied by Benettin *et al.* [Benettin *et al.* (1980)] and rigorously analyzed by Pesin [Pesin (1976)]. In the literature for chaotic oscillations of various dynamical system, the Benettin *et al.* algorithm [Benettin *et al.* (1980)] has been widely applied. In what follows, we give a background of the algorithm emphasizing on the problems devoted to direct numerical realization.

We take an arbitrary system composed of n -dimensional vector x (n -dimensional phase space), and an input system of differential equations is integrated on a certain interval. Further, we consider the linearized system for the initial point of the integration interval. We get a new system composed of n vectors. Then this system is orthonormalized via the Gramm-Schmidt algorithm, and serves to get a new system of vectors x_i for the next computation step. Logarithms of the normalization coefficients for each of the vectors are averaged on sufficiently large number of iterations, and the obtained limits of the digital sequences define a spectrum of LEs. It should be emphasized that the initial system should be in a certain stationary state, and the phase point at the end of each integration step serves as the initial condition for the next computational interval.

In the work Benettin *et al.* [Benettin *et al.* (1980)], it has been shown that a choice of the initial system of vectors x_i can be realized

in an arbitrary manner, and does not influence the limiting values of LEs.

In practice, the numerical integration of the linearized systems should be carried out using the same method as it is done for a non-linear system. It means that the computational complexity of the algorithm is of $n + 1$ times larger than for the integration of the original input system. In practice, the orthogonalization of the system should be carried out at each step of the Runge-Kutta method in order to achieve the required accuracy. Small angles between the vectors χ_i , and the orthonormalization process causes high error rates. It means that the computational complexity of the algorithm increases. For a system with small dimension of the linearized equations, the problem can be solved analytically.

For example, for the elastic beam-strip the Jacobi matrix of the system (8.144) has the following form

$$I(A_1, t) = \begin{pmatrix} 0 & 1 \\ -\pi^2(\lambda\pi^2(1 + 9A_1^2) - P_x(t)) & -\varepsilon \end{pmatrix}. \quad (8.134)$$

Let χ_1, χ_2 be eigenvalues of the matrix (8.134), then a solution to the differential equation $\frac{dA}{dt} = I \times A$ with the initial condition

$$A(0) = \begin{pmatrix} A_1(0) \\ A'_1(0) \end{pmatrix}, \quad (8.135)$$

has the following form

$$A(t) = \begin{pmatrix} \frac{1}{\chi_1 - \chi_2} \{ [-\chi_2 A_1(0) + A'_1(0)] e^{\chi_1 t} \\ - [-\chi_1 A_1(0) + A'_1(0)] e^{\chi_2 t} \} \\ \frac{1}{\chi_1 - \chi_2} \{ \chi_1 [-\chi_2 A_1(0) + A'_1(0)] e^{\chi_1 t} \\ - \chi_2 [-\chi_1 A_1(0) + A'_1(0)] e^{\chi_2 t} \} \end{pmatrix}. \quad (8.136)$$

Observe that in general χ_1, χ_2 are complex, and in practice the formula has different representation for complex and real χ . Therefore, solutions of the linearized system can be found directly without applying the numerical integration formula (8.136). It essentially decreases the computational time and increases the obtained accuracy. Comparison of these two ways shows that they are practically equivalent (the difference is of 0.1%).

Solution (8.136) character is associated with the second method of determining the LE. The formula implies that the length of vectors x_i exponentially increases/decreases according to the real parts of χ_1, χ_2 . Therefore, computation of LEs can be carried out by the direct averaging of the real parts of the eigenvalues of the Jacobi matrix along a phase curve. The latter method yields a qualitative picture of LEs contrary to the classical approach aimed at the approximate numerical approach.

Therefore, for the beam-strip [from (8.134)], the following characteristic equation is obtained

$$\chi(\chi + \varepsilon) + \pi^2(\lambda\pi^2(1 + 9A_1^2) - P_x(t)) = 0, \quad (8.137)$$

which yields the eigenvalues

$$\chi_{1,2} = -\frac{\varepsilon}{2} \pm \sqrt{\frac{\varepsilon^2}{2} - \pi^2(\lambda\pi^2(1 + 9A_1^2) - P_x(t))}. \quad (8.138)$$

The spectrum of LEs (χ_1, χ_2) has following properties $\chi_1 + \chi_2 = -\varepsilon$ and $\chi_2 < 0$. It is also relatively easy to formulate a criterion of chaos:

$$\chi_1 \geq 0 \Rightarrow \lim_{t \rightarrow \infty} \frac{1}{t} \int_0^t \operatorname{Re} \left(\sqrt{\frac{\varepsilon^2}{2} - \pi^2(\lambda\pi^2(1 + 9A^2) - P_x(t))} \right) dt \geq \frac{\varepsilon}{2}. \quad (8.139)$$

From the point of view of computational complexity, this method is the most suitable, since the number of additional actions is minimal, and majority of time is spent in the numerical integration of the nonlinear system (here the problem is solved directly). Furthermore, the speed of convergence of the method is higher compared to methods based on numerical integrations.

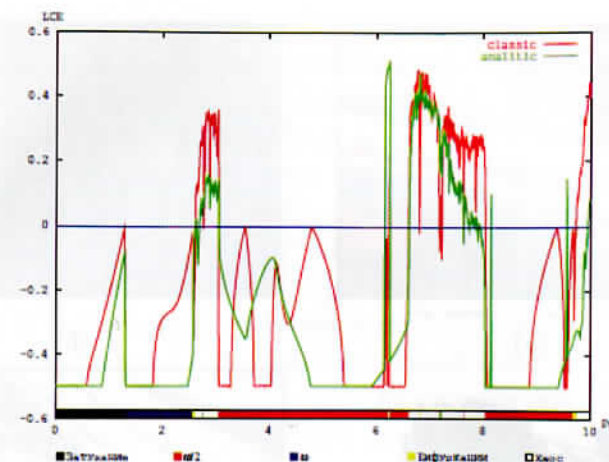


Fig. 8.7 Comparison of two computational methods to estimate the largest LE (the BGM).

However, although both methods give the same qualitative results, they differ with respect to the quantitative results. For instance, Fig. 8.7 shows a comparison of the largest LEs versus the external P_x for the fixed frequency u being equal to the fundamental system frequency. The first curve is obtained via the classical Benettin method, the second curve is computed by formula (8.139). The picture consists of the “color scale” defining the vibrations character, and it has been obtained on the basis of analysis of the power spectra of system vibrations.

8.1.4.2 Results reliability and LEs

Numerical experiment shows that the LEs coincide with the “color scale”, i.e. periodic vibrations correspond to negative/positive value at the largest LE, whereas bifurcations correspond to χ_1 close to zero.

The problem of comparison of different characteristics is important while investigating reliability of the obtained results. This is why we have not limited ourselves to compare the characteristics associated with the change of one control parameter, but we have carried out a multi-scaled numerical experiment. The obtained results

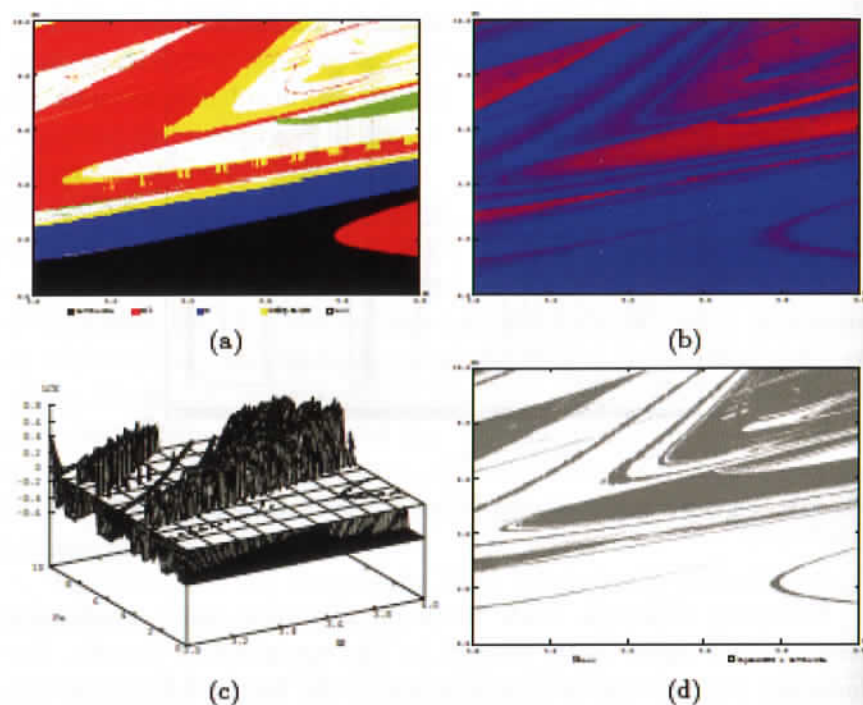


Fig. 8.8 Comparison of the largest LE and "chart" obtained through analysis of the power spectrum (BGM): (a) character of oscillations; (b) LEs; (c) maximal characteristic exponent depicted as 3D surface; (d) maximal characteristic exponent depicted as gray gradient (minimal LE (white), maximal LE (black)).

are reported in Fig. 8.8. Figure 8.8(a) is constructed for $\omega \in [3; 4]$, $P_0 \in [0; 10]$. Remaining three figures refer to three different ways of visualization of the maximum LE. Figure 8.8(c) corresponds to the largest characteristic exponent presented in the form of a 3D surface. The cross-section close to zero level (-0.05) is shown. Output of the surface above the cross-sectional plane denotes a transition of the LE into the space of positive values, i.e. chaotic vibrations. It is interesting to consider this plane in zones where bifurcations appear. For instance, let us study the line of first bifurcation. It is seen how the surface tends to zero level but never crossing it. Right-hand side Fig. 8.8(b) exhibits the largest exponent in the form

of grey color. The increase in darkness yields the increase in the characteristic exponent magnitude. Minimum value of the LE (-0.5) corresponds to the white color, and the maximum value corresponds to black color. Drops of bifurcation, zones and periodic vibrations in chaotic zones are visible. There are clearly visible curves of stiff bifurcations, whereas within bifurcation zones there is a border between the first and the second period doubling bifurcation. Inside there are drops of periodic vibrations and bifurcations. Furthermore, different zones of chaos have different measures of chaotization. In darker zones, the maximum LE is a little bit larger than in other chaotic zones. The last Fig. 8.8(d) deals with the cross-section of the surface of LEs by the plane close to (-0.05) and boundary of a zone where the exponent tends to zero. This figure is less informative than the previous one, but it allows to distinguish zones of regular and chaotic vibrations.

Comparison of the first figure with remaining ones gives the possibility to estimate the validity of the analysis on the basis of the power spectrum. It is clear that "charts" coincide with each other and mutually supplement each other [Awrejcewicz *et al.* (2002)]. First "chart" yields additional information on the character of one-frequency vibrations, allows to separate zones with vibrations with excitation frequencies and vibrations with frequency $\omega/2$. "Charts" of LEs allow to trace the evolution in transitional zones, give a possibility to estimate the measure of chaotization in different zones of chaos. Coincidence of boundaries of fundamental zones allows to conclude that the analysis of vibrations on the basis of power spectrum yields the results being in agreement with other methods, and can be applied to estimate the general chart of system behavior.

8.1.4.3 Stability versus maximal deflection

In order to describe scenarios of the system behavior with respect to its regular/chaotic dynamics it is useful to consider LEs and scales obtained on the basis of analysis of the power spectra together with purely mechanical characteristics like for instance maximal deflection. The latter quantity plays an important role in monitoring

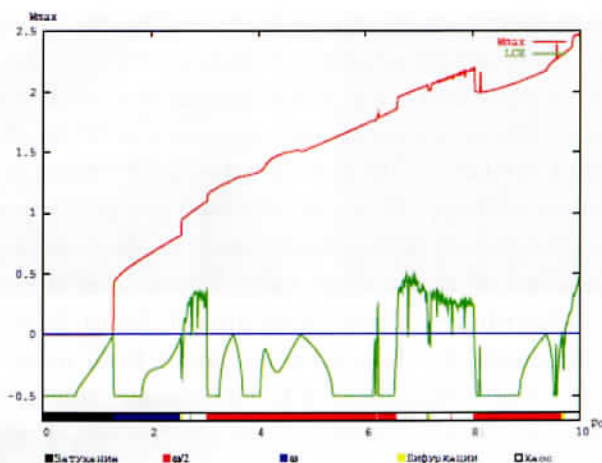


Fig. 8.9 Comparison of the maximum deflection, maximum LE and a “scale” constructed using analysis of the power spectrum (the BGM).

mechanical properties of the analyzed system. Figure 8.9 shows all three parameters.

Comparison of all three characteristics implies that all of them are coupled and mutually supplement each other. On the graph of maximum deflection, boundaries of the fundamental zones are visible. They are characterized by jump-type changes of the maximum deflection, i.e. the system suffers from a sudden stability loss associated with quantitative changes in mechanical regimes.

Zones of chaos differ remarkably from zones of periodic vibrations. In the periodic vibration zones, the maximal deflection increase occurs smoothly contrary to chaotic zones where the jumps appear. In comparison to the scale, the maximum deflection yields additional information for periodic vibrations. For example, for $P_0 = 4.8$ and $P_0 = 9.4$ the maximum deflection exhibits smooth jumps, which are not visible on the scale. Comparison of the maximum deflection with the maximum LE gives a picture of a “strange” system behavior. The LE points tend to zero, i.e. the system is on the threshold of transition into a new regime. These jumps remarkably differ from the changes in the maximum deflection on the boundaries of zones, since they are more smooth and do not change the smoothness of

the curve. Consideration of all exponents allows to yield wider and deeper conclusions regarding the system behavior. Non-homogeneity of one-frequency zones of vibrations and existence of the internal border are clearly visible on the curves of maximum deflection and maximum LE. It should be emphasized that the obtained dependencies of maximum deflection can be compared with estimation of the maximum LE. In many cases, when a computation of the LE spectrum is difficult owing to the complex form of the right-hand side of the differential equation, one may take into account only the maximum deflection.

8.1.5 Vibrations of flexible panels with infinite length

8.1.5.1 The BGM

In order to verify the reliability of the numerical realization of the BGM a series of the numerical experiments has been carried out. At first, we define the fundamental frequency of the system. We consider the free vibration of the beam-strip for $\varepsilon = 0$ and with $P_x(t) = q(t) = 0$ for the initial boundary conditions (8.47)–(8.50) (simple support). We get the particular case of the Duffing equation (8.62) and hence

$$\bar{A}_1 = -(1 + 3A_1^2) \lambda \pi^4 A_1. \quad (8.140)$$

For small vibrations, we can neglect the nonlinear term influence, and the fundamental frequency can be defined by the following linearized equation

$$\bar{A}_1 = -\lambda \pi^4 A_1. \quad (8.141)$$

Its solution is $A_1 = \cos(\omega_0 t + \varphi_0)$, and the frequency $\omega_0 = \pi^2 \sqrt{\lambda}$.

The numerical experiment has been carried out for Poisson's coefficient $\nu = 0.3$. The fundamental frequency is $\omega_0 = 2.9866$. The following parameters are fixed within the numerical experiment: $\varepsilon = 0$, amplitude of initial deflection $a_0 = 0.01$, time step $dt = 2^{-7} = 0.0078125$, and the integration is carried out by the RK2 method. In Fig. 8.10, time history of the beam-strip central point and the power spectrum are reported. As it can be seen from

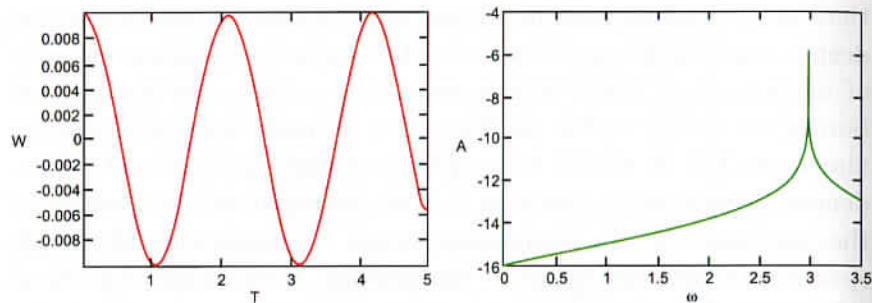


Fig. 8.10 Free vibrations ($\varepsilon = 0$) of the beam-strip (the BGM).

the figure, the amplitude of the harmonic vibration is 0.01, whereas its non-dimensional, period $T = 2.10156$ and the angular frequency $\omega = \frac{2\pi}{T} = 2.9897$. Therefore, the introduced numerical error is less than 1%. This simple experiment verifies the validity of the first approximation of BGM.

Additional verification of the result can be yielded by a solution to the static problem via the “set up” method. Static problems of structural members are widely described and investigated. Here, we aim only at the so-called problem of buckling. For this purpose, we consider the problem of longitudinal beam strip loading.

Let the longitudinal load $P_x(t) = P_1$ be an infinite length impulse. Depending on the value of the external load, the beam-strip will deflect up to a certain amplitude. For small values of the external force the deflection is zero, but after a certain critical value the deflection will be different from zero and starts to increase with the increase in P_1 . In order to solve the static problem via the set-up method, we consider the beam-strip with the small initial deflection $a_0 = 0.01$ in the strongly dissipative medium ($\varepsilon = 10$) under the action of the infinite length impulse. As a result, for each value of the external force we can obtain the curve shown in Fig. 8.11(a). The threshold value of the deflection corresponds to a solution of the static problem for the given load (in our example, $P_1 = 2.5$). Therefore, the function $W_s(P_1)$ is constructed [Fig. 8.11(b)]. Integration has been carried out by the second, RK2 method. Integration has been with time step $dt = 2^{-8} = 0.00390625$.

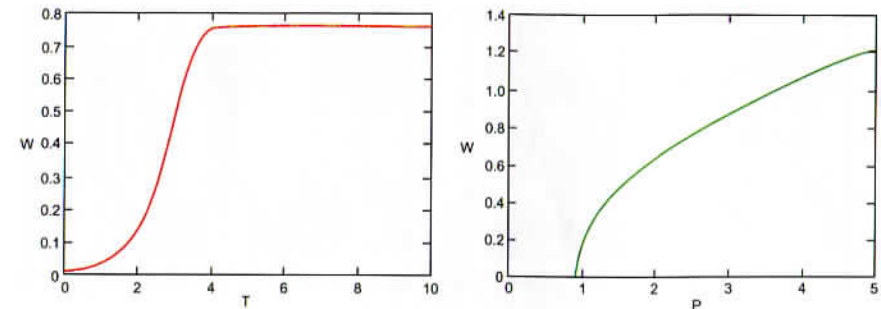


Fig. 8.11 Buckling effect while solving the static problem via the set-up method (BGM).

In order to get the analytical form of this dependence, the stationary solution of Eq. (8.62) should be considered

$$(\lambda\pi^2(1 + 3A_1^2) - P_1)A_1\pi^2 = 0, \quad (8.142)$$

$$A_1 = \pm \sqrt{\frac{1}{3} \left(\frac{P_1}{\lambda\pi^2} - 1 \right)}. \quad (8.143)$$

It is clear that in the interval $P_1 \in [0; \lambda\pi^2]$, solution (8.143) has no physical meaning, and hence zero solution is obtained. In interval $P_1 \in [0; \infty]$, the results of the numerical experiment coincide in full with the analytical solution. The sign of the numerical solution is defined by a sign of the initial deflection. For a positive (negative) initial deflection, the positive (negative) deflection branch is realized.

One of the important questions in the BGM is the choice of an approximation order that would guarantee a sufficient reliability level. The first approximation has a simple character and opens the door for another class of problems. Solution in higher approximations yields a system with a large system of degrees of freedom (DOFs), and a more complex behavior in comparison to the first approximation arises. In this work, we aim at a determination of the order of the series guaranteeing qualitative reliable results. The stream convergence consequence principally cannot be achieved in the problem of nonlinear dynamics owing to the dynamical instability of the input problem.

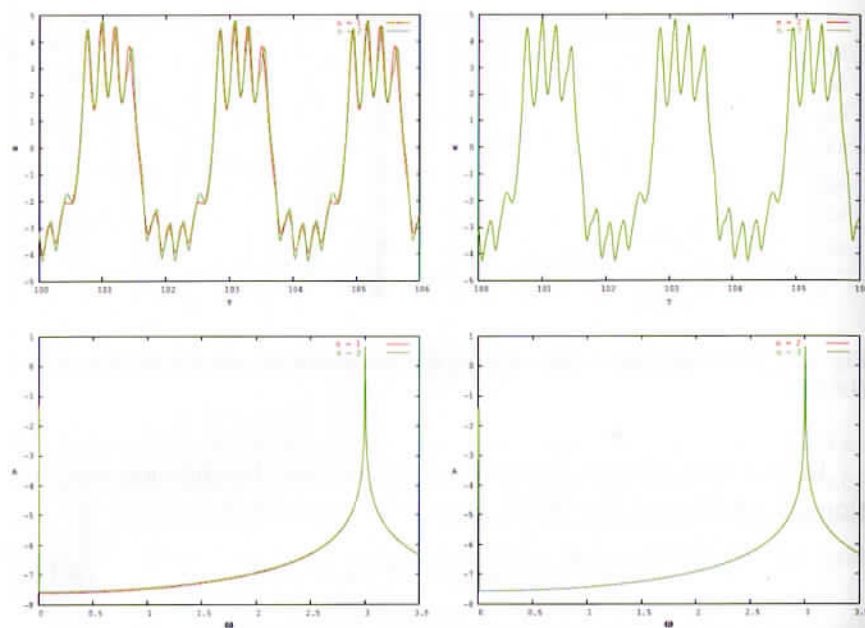


Fig. 8.12 Stream and integral convergence in a zone of harmonic vibration (BGM).

In Figs. 8.12 and 8.13, different orders of approximation has been applied. The beam-strip subject to harmonic load $q(t) = q_0 \sin(\omega_0 t)$ has been studied, where ω_0 stands for the system fundamental frequency.

We have considered two characteristic points: $q_0 = 900$ — the system is in a harmonic regime (Fig. 8.12) and $q_0 = 1200$ — the system is in a chaotic regime (Fig. 8.13). In each of the pictures, a comparison of vibrations of the central beam point for different orders of approximation and comparison of integral characteristics (power spectra) are carried out. Vibrations in the chosen beam points have sufficiently large amplitudes (order of 5–6 beam thickness), i.e. nonlinear terms play a key role in Eq. (8.61). Integration has been carried out by the RK2 method with the step in time $dt = 2^{-8} = 0.00390625$.

One of the aims of this work is to investigate scenarios of transition from periodic to chaotic vibrations. It is important to have a general imagination of the system behavior regarding the external excitation parameters. Therefore, it is necessary to construct the

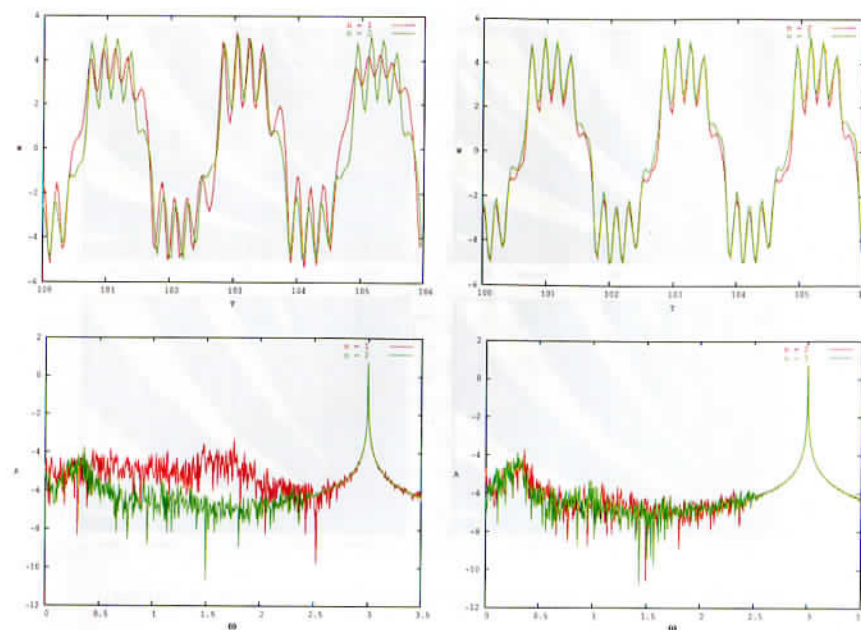


Fig. 8.13 Stream and integral convergence in chaotic vibrations (BGM).

so-called charts of plate vibrations for each type of the boundary conditions and external load excitation. A chart represents the plane (A, ω) , where A is the control parameter and P_0 stands for the excitation amplitude. Each point of the chart is denoted by a color characterizing the regime of vibrations. Therefore, we get informative visual representation of the system behavior. Character of vibrations is defined in full by the beam center point vibrations ($x = 0.5$), since all of the remaining points move in a synchronized manner. For each pair of the parameters (A, ω) , on the basis of analysis of the Fourier spectrum of the beam center point vibrations, the vibration character is defined. While constructing the chart, the frequency interval ω from $\frac{1}{2\omega_0}$ to $\frac{1}{32\omega_0}$ where ω_0 is the plate fundamental frequency for the given boundary conditions, is analyzed. Interval of changes of A has been chosen in a way that the maximum beam deflection does not achieve the value of seven beam thickness. Hence, the hypothesis of the average deflection taking into account the geometric nonlinearities has been satisfied.

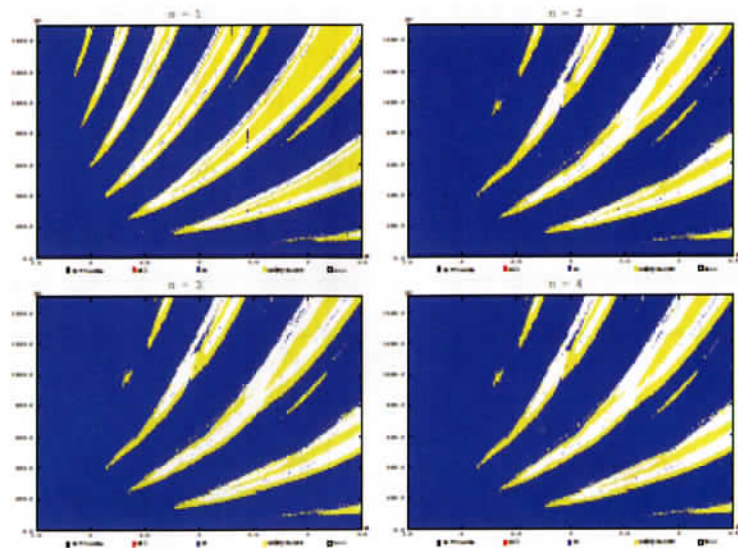


Fig. 8.14 Charts of vibrations for the transversal load (BGM).

We have already considered the problem regarding the BGM convergence for fixed characteristic pairs (q_0, ω) corresponding to periodic and chaotic vibrations. We should ensure that the results of different approximations coincide for whole choice of the considered parameters. Therefore, the vibration charts have been computed for the transversal load. In Fig. 8.14, the charts for the first four series of BGM have been presented. The integration has been carried out via the RK2 method with time step $dt = 2^{-8} = 0.00390625$. One may distinguish the difference between the first and the second approximation, where further increase in the approximation terms does not bring any quantitative changes in the chart.

The obtained results allow to conclude that in order to get qualitative results it is sufficient to consider only three terms of the series. This is enough to separate zones of periodic, chaotic or quasi-periodic dynamics.

We have also analyzed the problem of convergence regarding time step and the applied integration method. The given numerical experiments with application of the second-order Runge-Kutta method (RK2IMP), fourth-order Runge-Kutta method (RK4,

RK4IMP), fourth-order modified Runge-Kutta method (Fehlberg method (RKF45) and Cash-Karp method RKCK), eighth-order Runge-Kutta method (Prince method-Dormand method RK8PD) of the accuracy order and implicit Gear methods (GEAR1 and GEAR2). Steps in time have been chosen from 2^{-7} to 2^{-11} uniformly along the logarithmic scale.

Principle differences between the results obtained through different methods have not been found, hence in the fundamental numerical experiments the RK2 method with time step $dt = 2^{-8} = 0.00390625$ has been used (it is most suitable one from the point of computations). We have also constructed the chart for the transversal load $P_x(t) = P_0 \sin(\omega t)$. As it has been mentioned earlier, in this case we may take only the first term of the series and we get the Duffing Eq. (8.62). Then, changing the variables $A_j(t) = \dot{A}_j(t)$ we reduce the problem to the following one

$$\begin{aligned} \dot{A}_1 &= A'_1, \\ \dot{A}_1 &= -\varepsilon A'_1 - ((\lambda \pi^2 (1 + 3A_1^2) - P_x(t)) A_1 \pi^2) \pi^2 A_1. \end{aligned} \quad (8.144)$$

In Fig. 8.15, the chart obtained via BGM is presented for the initial boundary conditions (8.47)–(8.50). Integration has been carried out by the RK2 method with time step $dt = 2^{-8} = 0.00390625$.

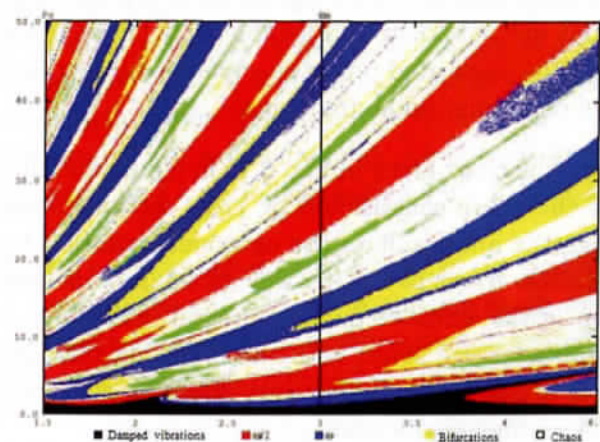


Fig. 8.15 Chart of vibrations for the longitudinal load (BGM).

The chart investigation allowed to separate the following characteristic regimes:

- (i) This vibration character cannot be exhibited while applying the transversal load, and hence the variant of the longitudinal load is of a particular interest. In this case, we can observe a stiff bifurcation, i.e. the jump-type transition from damped to periodic vibrations while negligibly increasing the amplitude of the external load. Two characteristic cases of vibrations have been observed after the stiff bifurcations: stationary one-frequency vibrations with the synchronized frequency equal to excitation frequency, and the subharmonic vibrations with $\omega_p/2$.
- (ii) After the first stiff bifurcation, a further increase in the excitation amplitude shifts the system dynamics into a periodic regime. As it has been already mentioned, either harmonic or a subharmonic motion with $\omega_p/2$ has been exhibited. There are also narrow subharmonic zones with frequency equal to $\omega_p/4$.
- (iii) Chaotic zones are of particular interest. Here we apply only frequency power spectrum to measure chaotic dynamics and the vibration zones.
- (iv) In between zones of different dynamics one may observe small transitional zones associated with soft type bifurcations. Vibrations in those zones are still regular ones, but the trajectories of vibrations are not so strongly stable as it happened in periodic regimes. The associated power spectrum exhibits the occurrence of peaks on subharmonic frequencies.

We analyze the chart given in Fig. 8.15 in a more detailed manner. We consider the chart constructed by cross-sections along the axis P_x , we change the amplitude of the external excitation but keeping a fixed excitation frequency. This way of analysis is based on the consideration of the whole frequency interval, which can be divided into three characteristic zones with the following magnitude of the frequencies: [1.5; 2.2] — low frequencies, [2.2; 3.8] — average frequencies, [3.8; 4.5] — high frequencies.

For small amplitudes of the excitation force the delivered energy is not sufficient to generate undamped vibrations. The bottom part

of the chart is associated with damped vibrations. The upper border of this zone corresponds to the first stiff bifurcation. In other words, a small increase in the external excitation amplitude changes qualitatively the picture of vibrations, i.e. there is a transition from damped to periodic vibrations. We may distinguish two characteristic cases after the stiff bifurcation: either the vibration frequency is equal to ω_p or $\omega_p/2$. For zones of low and high frequencies we have periodic vibrations with $\frac{\omega_p}{2}$, whereas in a zone of average frequencies we have ω_p . It has been observed numerically that the beam vibrations are realized with three frequencies $\omega_p/4$, $\omega_p/2$, ω_p . We consider the scenario of successive bifurcations in a zone of average frequencies. After the stiff bifurcation we have periodic vibrations of frequency ω_p . Successive increase in P_x implies a series of bifurcations and a transition to chaotic vibrations. Similar scheme of the frequency switching is also characteristic for two other zones, but instead of ω_p , we have $\omega_p/2$, i.e. subharmonic vibrations appear. On the chart, there are separated zones where there is subharmonic vibration with $\omega_p/4$, and zones without bifurcations. Zones with bifurcations exhibit two characteristic cases either a transition from periodic to chaotic vibrations or associated with zones located within periodic zones.

In what follows, we consider separately particular cases on boundaries between frequency zones. Here jump-type frequency switching is observed without any series either of bifurcations or a transition through a chaotic regime. The mentioned zones of frequencies are located in intervals [2.1; 2.2] and [3.8; 4.2]. After the first stiff bifurcation periodic vibrations appear. Further, on a short interval of P_x , values of vibrations are again damped. After that, stiff bifurcation takes place again, and a periodic solution with a different frequency occurs.

More careful attention allows to distinguish the similarity between the chart's parts. In general, all three frequency zones are self-similar. This is particularly exhibited in a zone of small amplitude of excitations. Shapes of areas are repeated in three zones; the larger the frequency, the larger is the area. As it has been already mentioned, the neighborhood zones differ from each other by an order of the frequency switching for periodic vibrations. Therefore, similar zones

may have the same qualitative character of vibrations but they may differ in quantitative characteristics.

Since in certain parts a transition into chaos is associated with a series of bifurcations, we have investigated a correspondence of the observed series behavior to the Feigenbaum scenario [Awrejcewicz *et al.* (2002); Krysko *et al.* (2002)].

We have carefully studied the first cascade of bifurcations while transiting into chaos in a zone of averaged frequencies. We have detected eight bifurcations. For example, we report here the case of the Feigenbaum constant computation for the fundamental frequency $\omega_0 = 3$ (Table 8.3). Values of C_i are obtained from the following relation

$$C_i = \frac{P_x^n - P_x^{n-1}}{P_x^{n+1} - P_x^n}. \quad (8.145)$$

These results correspond well to the theoretical values

$$C_\infty = \lim_{n \rightarrow \infty} \frac{P_x^n - P_x^{n-1}}{P_x^{n+1} - P_x^n} \approx 4.6692 \dots \quad (8.146)$$

In Fig. 8.16, the spectrum for $\omega = 3$, $P_x = 2.616819$ associated with nine bifurcations is shown.

It is interesting to follow how the largest LE behaves in the series of Hopf bifurcations. In Fig. 8.17, the largest LE behavior while approaching to the critical point of a transition to chaos is shown. On the axis Ox , we have logarithmic scale and the first four Hopf bifurcations are visible. After achieving the successive bifurcation, the largest LE tends to zero and then decreases again.

Process of chaotic vibrations in the parameters plane (P_x , ω) begins with a period doubling bifurcation. Series of these bifurcations is easily observed on the power spectrum (see Fig. 8.16). Up to eight bifurcations have been monitored. The process of chaotization

Table 8.3 Amplitude of the external load in the first series of bifurcations.

	1	2	3	4	5	6	7	8
P_x	2.5732	2.6036	2.6136	2.61615	2.616679	2.616790	2.616814	2.616819
C_i		3.028	3.975	4.770	4.759	4.708	4.683	

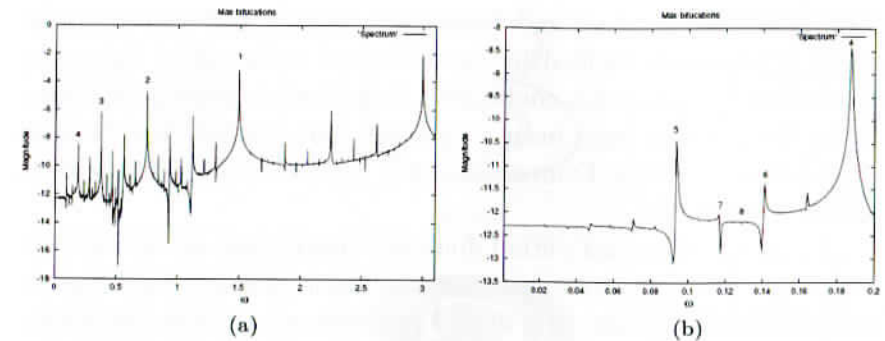


Fig. 8.16 Power spectra with eight bifurcations (BGM) for $\omega_p = 3$, $P_x = 2.616819$ (a) and a part of the graph a (b).

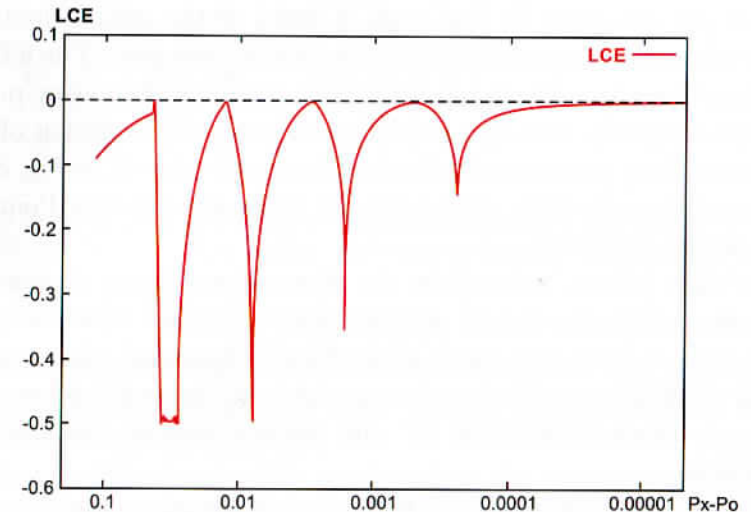


Fig. 8.17 Largest LE exhibited by the series of Hopf bifurcations.

observed via the frequency spectrum is characterized by a smooth noising of the spectrum base. Sharp peaks remain on the fundamental frequencies and their harmonics.

A series of the period doubling bifurcations implies occurrence of the infinite cascade of the period doubling bifurcations as the mechanism of transition into chaotic vibrations [Afraimovich *et al.* (1986);

Arnold (1979); Astahov and Bezruchko (1987)], and also fits properties of similarity yielded by the theory of universality. For many dynamical systems with continuous time, five or more period doubling bifurcations have been illustrated and studied in references [Franceschini (1980); Franceschini and Tabaldi (1979); Grutchfield and Farmer (1980)].

A route to chaos via period doubling bifurcations and occurrence of chaotic (Smale) attractors (see [Shilnikov (1956)]) yield the so-called Smale horseshoe structure. The obtained attractors are either called Feigenbaum attractors or strange attractors [Arneodo and Collet (1985); Arneodo and Thual (1985)]. Particular feature of the Smale attractor relies on keeping maximum harmonic value associated with the fundamental frequency after the occurrence of the broadband spectrum. In Fig. 8.18, a series of the period doubling bifurcations tending to the Smale attractor is presented. The following time histories $w(t)$, Poincaré sections $w(\dot{w})$ and frequency power spectra are given. It is also important to trace the evolution of the attractor along parameter P_0 for eigenfrequency $\omega_0 = 3$. In Fig. 8.19, the most characteristic attractors and the corresponding Poincaré sections are presented.

In what follows, we explain the observed nonlinear phenomena using the qualitative theory of differential equations. When a stable limit cycle is born as a result of the Hopf bifurcation, the previous stable equilibrium point becomes unstable of the saddle-focus type with one-dimensional stable W^s and two-dimensional unstable W^u manifolds.

Then two multipliers of the limit cycle become complex conjugated. Now W^u starts wrapping on the limit cycle creating configurations similar to [Shilnikov (1956)]. Increase in the load over the criticality may lead to the following behavior. W^s and W^u approach each other up to the occurrence of a homoclinic curve of the saddle-focus type. In this case, the complex structure is created which implies the existence of a chaotic attractor (the name of this attractor is not uniquely defined). In references [Arneodo and Collet (1985); Arneodo and Thual (1985)] it is called the *screw-type attractor*. In Shilnikov's work [Shilnikov (1956)], it is called the *spiral attractor*. The typical

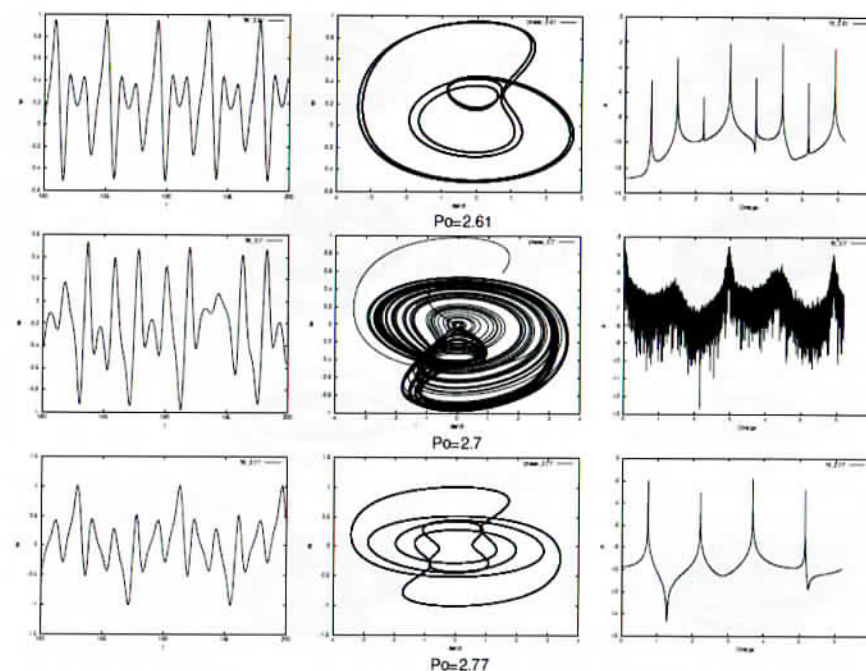


Fig. 8.18 Time histories, phase portraits and frequency power spectra for different P_0 : (a) 2.61, (b) 2.7, (c) 2.77 in the neighborhood of the smale attractor.

situation occurs when period doubling bifurcations take place before the occurrence of Shilnikov's attractor, and then a transition to the Smale attractor takes place.

On the other hand, while moving along the parameter the following situation is possible: there is no loop, but Shilnikov's attractor does exist. In other words, there is a special type of attractor which can be identified only by its vicinity to the bifurcation manifold with the saddle-focus loop. The existence of an attractor with defined properties being characteristic for the Shilnikov attractor has been illustrated in the reference [Arneodo and Thual (1985)]. Therefore, criteria are needed allowing to distinguish Smale attractors from other attractors located in the vicinity of a saddle-focus loop. One of such criteria is motivated by a fact that in chaos associated with the Smale attractor, time instants for which maxima of oscillations are

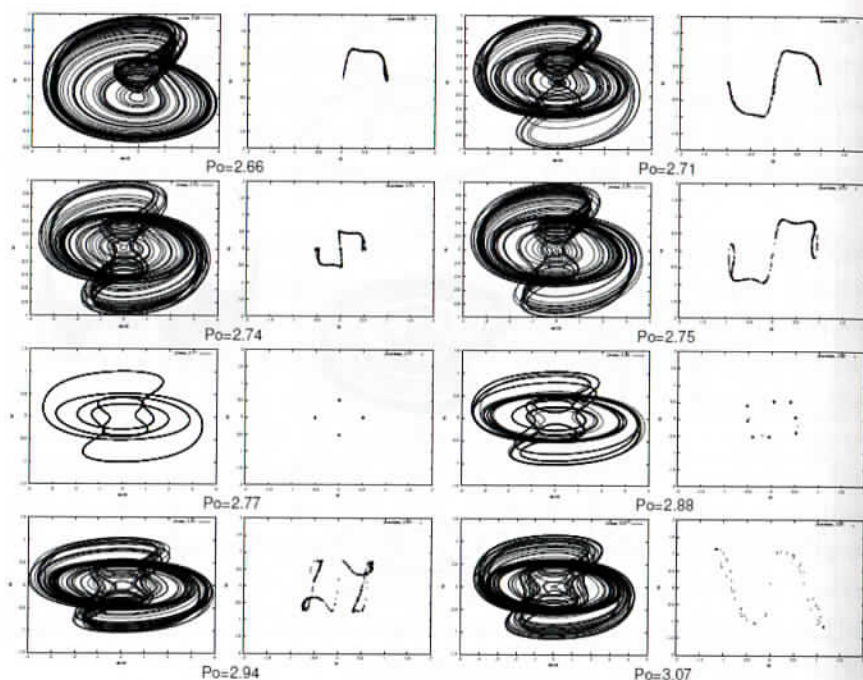


Fig. 8.19 Evolution of attractors and Poincaré maps.

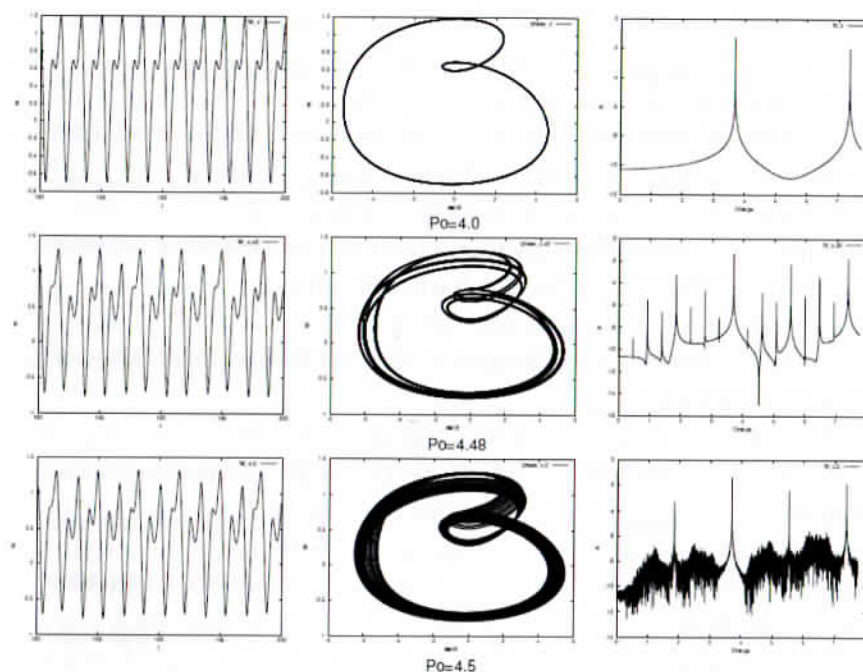
regularly distributed, whereas within Shilnikov's type chaotic attractor they constitute a stochastic sequence.

Besides the Smale and Shilnikov attractors, we have also Rössler type attractors. We demonstrate Rössler type attractors occurred after a series of period doubling bifurcations. In Fig. 8.20 a scenario yielding its birth for the values $P_0 = 4; 4.48; 4.5$ is reported. The last of the phase portraits is the Rössler attractor. In Fig. 8.20 $w(t)$, $w(\dot{w})$ and the power spectrum are shown.

8.1.5.2 Numerical experiment (FDM)

Convergence of the difference scheme

We study a convergence of the explicit scheme of problem (8.71) and (8.72) versus an order of approximation of the difference derivatives. As the pattern problem we consider the case of parametric vibrations

Fig. 8.20 Time histories, phase portraits and frequency power spectra for different P_0 : (a) 4.0, (b) 4.48, (c) 4.5 in the neighborhood of the Rössler attractor.

with the external load $P_x(t) = P_0 \sin(\omega_0 t)$, where ω_0 is the fundamental frequency of the system, $q(x, t) = 0$ and with the boundary/initial condition (8.49)–(8.52). In comparison to the boundary/initial condition (8.47)–(8.50) and (8.48)–(8.51) the considered problem is not symmetric, and hence we analyze the difference scheme convergence.

We are aimed at an estimation of the vibrations character versus the excitation amplitude. From a point of view of applied mechanics it is important to define zones of changes of the excitation amplitude where vibrations are chaotic. Therefore, we tried to achieve the integral convergence of the method. For this purpose scales for various partitions, used approximations order and integration methods have been constructed. A “scale” presents a color representation of a vibration character versus the excitation amplitude P_0 . These

scales have been constructed on the basis of analysis of the vibration power spectra of the beam center. Namely, for each value of P_0 simulation has been carried out, then the power spectrum of vibrations of the beam center has been obtained, and finally the vibration beam regime has been defined. Each regime is marked with a different color. The following characteristic regimes have been detected: damped vibrations — energy introduced by external force is too small to beat the dissipative forces; harmonic vibrations with frequency ω_0 — synchronization between the system and external force; sub-harmonic vibrations with frequency $\frac{\omega_0}{2}$; period doubling bifurcations; chaotic vibrations.

In Fig. 8.21 scales regarding the explicit method are reported. For the boundary initial conditions (8.49)–(8.52) the fundamental frequency $\omega_0 = 5$, whereas for the interval of P_0 variations $[0; 50]$ this corresponds to the boundaries, where assumptions regarding applicability of theory of shallow plates are valid, i.e. deflection of the beam should not be larger than its 6–7 thickness. As a pattern result we consider the scales obtained for $n = 32$, $dt = 2^{-11}$, whereas the numerical integration has been carried out via the eighth-order method RK8PD. Analysis of the obtained results yields a conclusion that the integral convergence is achieved for partition $n = 16$, $dt = 2^{-8}$ for the applied RK2 method. Approximation of order $O(h^2)$ smoothes higher frequencies of the signals, and hence for large values of the excitation amplitude the difference scheme does not properly enough present the real system behavior. On the other hand, in the case of sufficient flat transition, functions of $O(h^6)$ (Fig. 8.25) amplify high frequencies input, and in result the difference scheme is divergent ($n = 16$, $dt = 2^{-8}$ for integration via the RK2 method). Finally, the results obtained by the RK2 method are reliable, and there is no need to apply higher orders Runge–Kutta methods.

In Fig. 8.21, for comparison purpose, numerous results obtained via the implicit method with different values of the weight coefficient σ are reported. Implicit difference schemes are more stable, which allows to apply larger steps in time than for explicit schemes for the same partitions of the space coordinates. Stability of the implicit difference scheme is guaranteed by a strong smoothing of

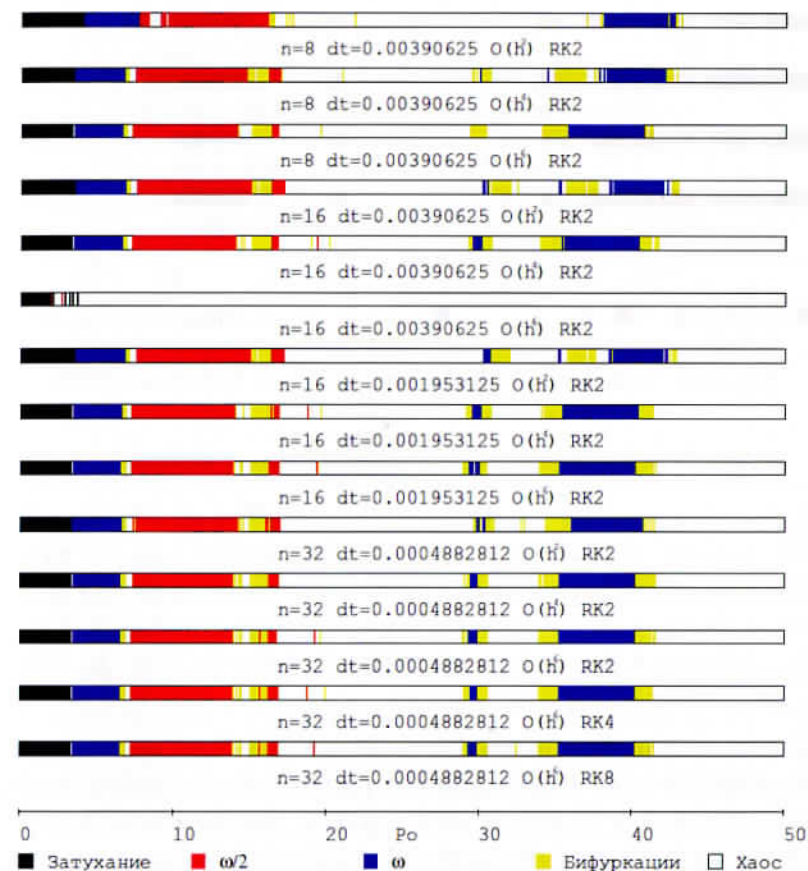


Fig. 8.21 Convergence of explicit difference methods with various approximation orders.

high frequencies, but simultaneously frequencies associated with the fundamental system energy are also smoothened. This is why for the weight coefficient $\sigma = 0.5$, the stability of the difference scheme has not been achieved. The result being close to the pattern ones can be only achieved for the weight coefficient $\sigma \approx 1$, which in fact reduces the problem to that of integration via the Euler method. Besides, the implicit scheme for equivalent partitions has larger computational complexity than the associated explicit scheme. Only for $\sigma = 0$ the method yields a computational benefit, since the computation of the operator Z on the previous layer can be avoided. In Fig. 8.22 the

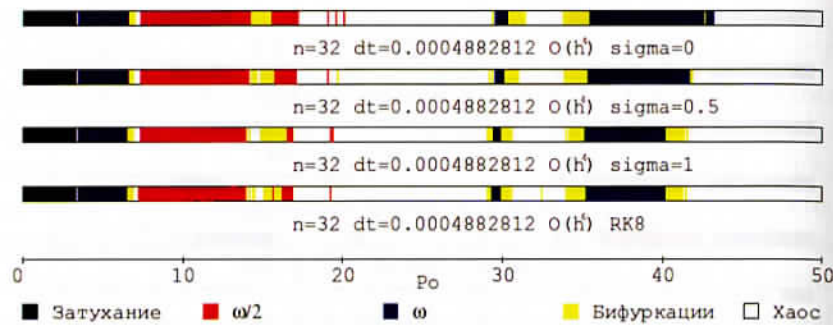


Fig. 8.22 Comparison with the implicit Crank–Nicholson scheme.

Table 8.4 Square average errors of different methods.

n	8	12	14	16	18	20	32
$O(h^2)$	1.14e+2	5.12e+1	3.76e+1	2.88e+1	2.28e+1	1.84e+1	7.17e+0
$O(h^2)$	1.18e+1	2.41e+0	1.31e+0	7.69e-1	4.81e-1	3.16e-1	4.82e-2
$O(h^2)$	1.29e+0	1.20e-1	4.82e-2	2.18e-2	1.08e-2	5.75e-3	3.45e-4
PS	1.88e+0	1.90e-3	3.20e-5	2.46e-7	2.36e-5	3.11e-5	7.12e+1

scales for the implicit method $n = 32$, $dt = 2^{-11}$ of approximation order $O(h^4)$ $\sigma = 0$; 0.5; 1, and the pattern result, explicit method of $n = 32$, $dt = 2^{-11}$ as well as integration via the RK8PD method with approximation of the spatial derivatives $O(h^6)$ are reported.

A pseudo-spectral method with a Chebyshev mesh strongly differs from the explicit and implicit methods since points of the mesh have an influence on the values of the partial derivatives, not only on the neighboring ones. The latter fact should theoretically increase an accuracy of the being computed derivatives, but the high order interpolating polynomials oscillate on the interval ends (the Gibbs effect). This causes a lack of accuracy of the computed derivatives. In order to demonstrate this effect we consider the model problem devoted to computation of the fourth derivative. For the boundary conditions of the Dirichlet–Neumann problem (8.48) we take the function $w(x) = 1 - \cos(2\pi x)$, which satisfies the boundary conditions. In Table 8.4 the values of the square averaged numerical error of the 4th derivative computed either by the pseudo-spectral method

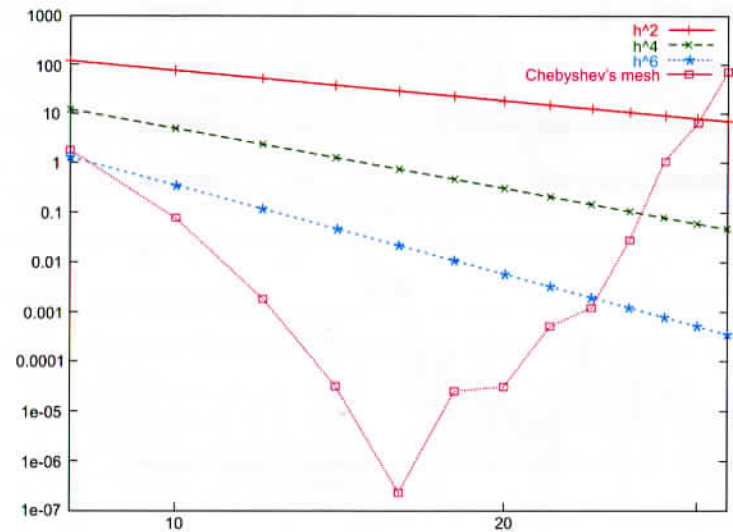


Fig. 8.23 Square average errors in computation of the fourth derivative.

or via the analytical value $w^{IV}(x) = 16\pi^4 \cos(2\pi x)$ are given. In this table, also data for difference derivatives of orders $O(h^2)$, $O(h^4)$ and $O(h^6)$ are reported. The data allow to get the following conclusion: the pseudo-spectral method yields higher order accuracy than the difference methods, but the error increases when the number of partitions increases. The table shows that for $n = 16$ the optimal partition for the pseudo-spectral method is obtained, and the increase in n implies a stability loss of the computational scheme. For the difference method the dependence of the error on a number of partitions yields a linear function in the logarithmic coordinates, and it monotonously decreases with the increase in n (Fig. 8.23). In order to get an imagination of the relative error of the method, it should be emphasized that the interval of the fourth derivative changes $[-1560; 1560]$, i.e. the same average error of order 1 corresponds to quantities of 0.01. For the first and second derivatives, the dependence of the error on n has the same character as in all considered cases.

As in the case of the implicit method, in Fig. 8.24 a comparison of the pattern result of the implicit method ($n = 32$, $dt = 2^{-11}$,

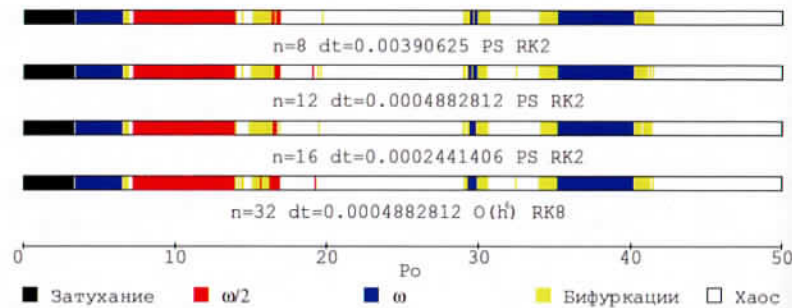


Fig. 8.24 Comparison of the pseudo-spectral method versus the Chebyshev mesh.

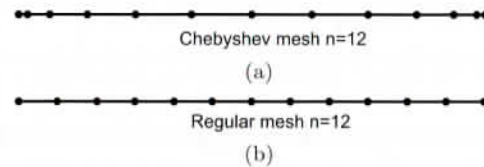


Fig. 8.25 The Chebyshev mesh (a) versus the regular mesh (b).

with integration of the RK8PD method and approximation of the spatial derivatives $O(h^6)$ with the results obtained via the pseudo-spectral method for various partitions is presented. Observe that steps of integration in time have been chosen smaller than in the case of analogous partition and the same integration method regarding the regular mesh. For $n = 8$, $dt = 2^{-9}$ (for regular mesh we have $dt = 2^{-8}$). This paradoxal phenomenon can be explained in the following manner: boundary layer points of the Chebyshev mesh are located essentially closer to the edge than in the case of the regular mesh (Fig. 8.25), and these points are most sensitive to the scheme errors, since their absolute values are always small (owing to the edges fixation — Dirichlet condition), whereas, on the contrary, the fourth derivative has the maximum value. Therefore, the error of the derivatives computation implies divergence of the difference scheme. We separately consider the problem of vibrations convergence for the explicit method.

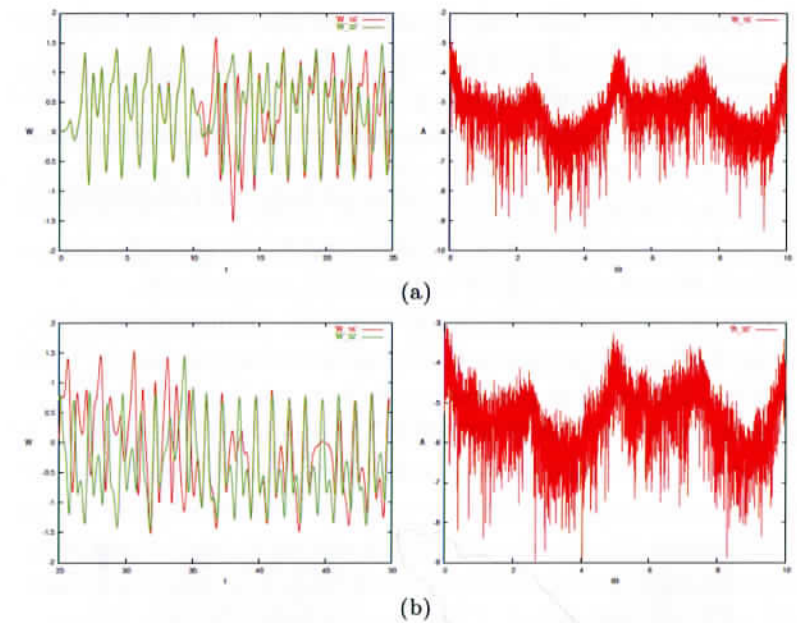


Fig. 8.26 Integral convergence in chaos: time histories and frequency power spectra for $n = 16$, $dt = 2^{-8}$ (a) and $n = 32$, $dt = 2^{-11}$ (b).

For example, in Fig. 8.26 vibrations of the beam center for various spatial partitions, as well as the power spectra of these signals (parameters of the external load $P_0 = 7$, $\omega_0 = 5$, partitions $n = 16$, $dt = 2^{-8}$ and $n = 32$, $dt = 2^{-11}$, integration has been carried out by the RK4 method, spatial derivatives are approximated by order of $O(h^4)$ are reported. It is obvious that the integral convergence is achieved (it is exhibited by the power spectra), but a full coincidence of the trajectories is not achieved. For both partitions the results qualitatively coincide, which means that the further increase in the spatial partition will not change the so far obtained result, i.e. chaotic zones are reliable and not introduced by the computational errors. The figure clearly shows that the signals coincide in full on a short initial time interval, but then they diverge and after that no correlation exists.

The influence of this problem is similar to that of simple supports of the edges considered earlier, and it can be solved with the BGM

with higher approximations. However, we use only the FDM since it is the most general and does not allow to introduce additional mathematical constructions on the contrary to the Bubnov–Galerkin approach. Fundamental frequency of the studied system essentially depends on the used boundary condition. For instance, for simple support and clamping (8.47)–(8.50) and (8.48)–(8.51) we may derive analytical formulas to define the fundamental frequency value: $\omega_0 = \pi^2 \sqrt{\lambda} \approx 2.98$ and $\omega_0 = (\frac{3}{2})^2 \pi^2 \sqrt{\lambda} \approx 6.705$, respectively.

The fundamental frequency has been also defined numerically. We take the dissipation term $\varepsilon = 0$, and we introduce the initial buckling $a_0 = 0.01$. Integration parameters follow: spatial partition $n = 16$, time step $dt = 2^{-8} = 0.00390625$. In Fig. 8.27 vibrations of the beam center are shown as well as the power spectrum of these vibrations. Time history indicates the periodic vibrations, and the power spectrum exhibits only one frequency vibrations, i.e. $\omega = 6.761$. The error magnitude introduced by numerical integration is less than 1%, which validates reliability of the obtained results.

Initially, the problem of the convergence of the difference scheme has been investigated. The Runge principle has been used to define the minimum partition required to get the reliable results regarding a chart construction. In Fig. 8.28 scales of the vibrations character constructed for different partitions ($\omega = 6.7$, $0 < P_0 < 50$) are reported.

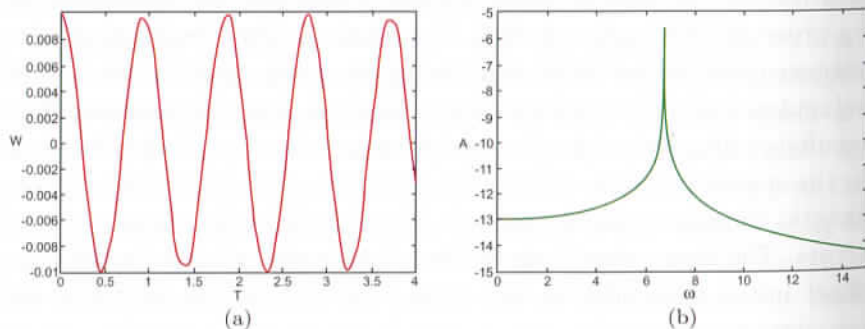


Fig. 8.27 Free vibrations in problem with clamping (FDM): time histories (a) and frequency power spectrum (b).

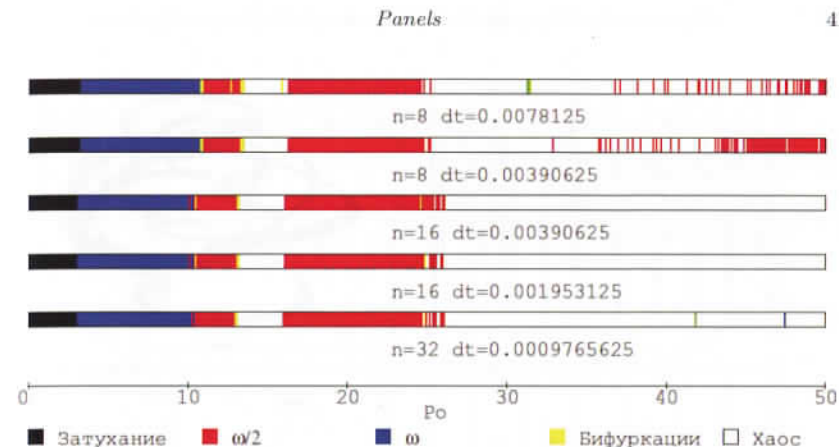


Fig. 8.28 Convergence of the explicit difference methods for various approximations for problems with clamping.

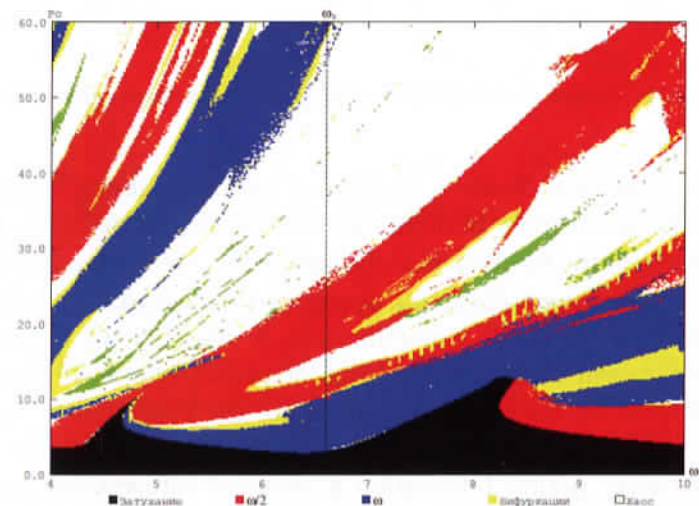


Fig. 8.29 Chart of vibrations for the problem with clamping (FDM).

It can be seen that the necessary computational accuracy is achieved for $n = 16$, $dt = 2^{-7} = 0.0078125$. This partition has been used to construct the chart given in Fig. 8.29. The fundamental frequency $\omega_0 = 6.7$, and hence the considered interval for ω is $[4.0; 10.0]$. The general behavior of the system is similar to that previously studied for the simply supported beam, but there exist also

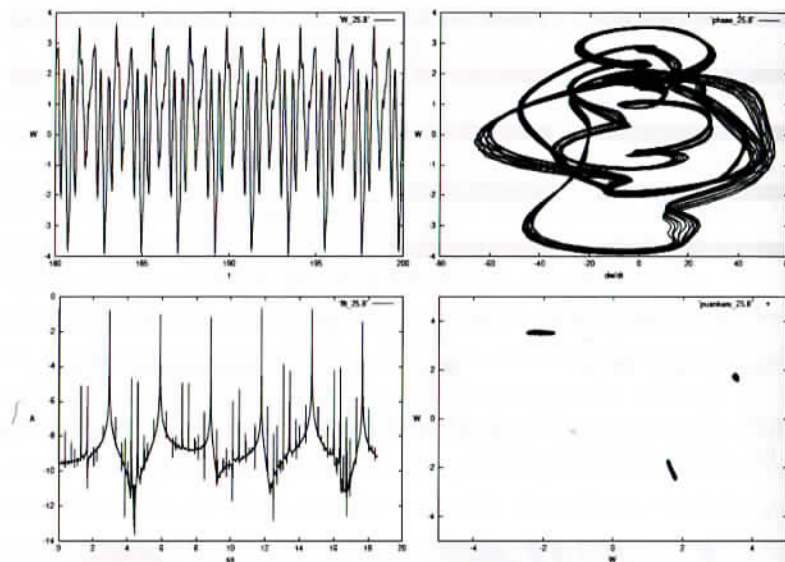


Fig. 8.30 Period doubling bifurcation (see text for more description).

a few peculiarities. Namely, in spite of period doubling bifurcation also the period tripling bifurcations have been obtained (Fig. 8.30).

In Fig. 8.30 the fundamental characteristics are shown: time histories $w(t)$, phase portraits $w(\dot{w})$, power spectrum and Poincaré maps ($\omega = 8.75$, $P_0 = 25.8$). Unfortunately, it was difficult to estimate borders between zones in the series of period tripling bifurcation, and therefore we were unable to estimate the Feigenbaum constant for this case. As it has been seen from the power spectrum, after the first triple period bifurcation a series of bifurcations appears, but they are different from either period doubling or period tripling bifurcations. This phenomenon requires further investigation.

For the studied problem a transition to chaos via period doubling bifurcations through the Feigenbaum scenario has been detected. In Table 8.5 the data used for the Feigenbaum constant computation associated with the fundamental frequency is given. The obtained results coincide well with the theoretical value $C_\infty \approx 4.6692$ (formula (8.146)). As in previous case, we have observed a series of eight Hopf bifurcations.

Table 8.5 P_x (amplitude of excitation) corresponding to the first series of bifurcations in the problem with clamping (FDM).

	1	2	3	4	5	6	7	8
P_x	14.6836	14.8441	14.9027	14.9150	14.9178	14.9184	14.9185	14.9186
C_i		2.7395	4.7368	4.5069	4.5705	4.4971	4.6358	

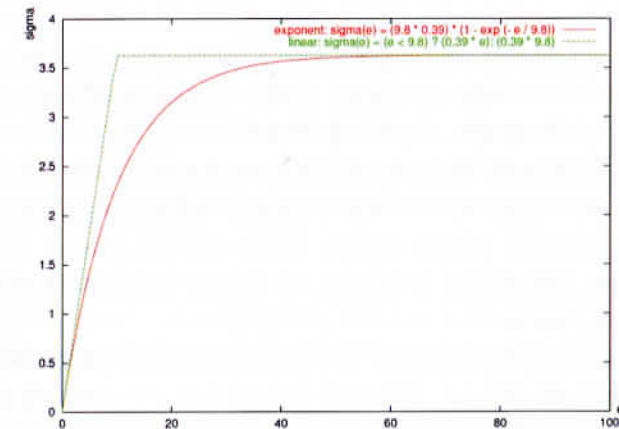


Fig. 8.31 Two-piece wise linear (a) and exponential (b) stress-strain dependence.

8.1.6 Geometric and physical nonlinearities

We consider the problem with physical nonlinearity for two variants of stress-strain relations: linear dependence of two linear pieces and the exponential transition into a plastic zone. These possibilities are presented in Fig. 8.31. Important role plays here a ratio of the linear beam with the ratio $\frac{a}{h} = 100$. Hence, the following variants of the dependence $\sigma(e)$ has been considered:

- (i) Two piece-wise linear dependence:

$$\sigma(e) = \begin{cases} ke_i, & \text{for } e \leq e_s, \\ ke_s, & \text{for } e > e_s. \end{cases} \quad (8.147)$$

- (ii) Exponential dependence

$$\sigma(e) = ke_s \left(1 - \exp\left(-\frac{e}{e_s}\right) \right). \quad (8.148)$$

The common point of two straight lines e_s corresponds to the critical deformation, after which a plastic zone appears. The coefficient of a slope of two piecewise linear characteristics has been chosen in a way that on the linear part of the dependence $\sigma(e)$ the governing equations should coincide in full with the equations taking into account only the geometric nonlinearity. All numerical experiments have been carried out for the following fixed parameters: $k = 0.39$ and $e_s = 9.8$.

For the problems with physical nonlinearity the fundamental experiments have been given in frame of the nonlinear geometrical problem statement: charts of vibrations types, the spectrum of LEs, as well different variants of the beam support. Besides, we have added one more parameter: beam deflection for frozen time instants taking into account plastic zones. Their analysis allows to estimate the plasticity level of the beam, i.e. to define, which part of the beam cross-section moved to a zone of plasticity.

In Fig. 8.32 a comparison of the fundamental characteristics (maximum deflection, largest LE and scales) for the excited longitudinal vibrations with the fundamental frequency (problem with simple support (8.47)–(8.50)) is shown. For small amplitudes of excitation

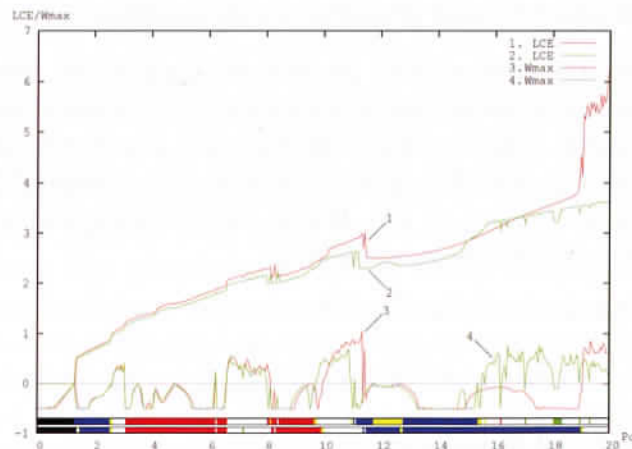


Fig. 8.32 Comparison of four dynamical characteristics for longitudinal excitation with the fundamental frequency (see text for more details).

amplitude, the deformations do not achieve plastic zones and solutions coincide in full. The increase in the amplitude of excitation yields the increase in the amplitude of vibrations of the beam, and hence its deformation is increased. For deflections of order of two beam thickness a zone of plastic deformation is visible in the central area of the beam. From this time instant solutions of geometrical nonlinear problem do not coincide with the physical solution of nonlinear problem. It should be emphasized that for a physically nonlinear problem we should consider essentially smaller interval of the external amplitude changes. As it can be seen from the figure, after a certain value the beam achieving the maximum deflection finally transits into a chaotic zone, and the maximum deflection rapidly increases. For this deflection magnitude the applied equations are not useful.

It is interesting to compare the charts of vibrations for the problem of physical nonlinearity and more simple modeling variant taking into account the geometric nonlinearity. In Fig. 8.33 the charts regarding the simple support of two edges are shown. The left chart presents a solution to geometrically nonlinear problem (a part of the chart (8.26)), whereas the right corresponds to the problem with two piece-wise characteristics (8.26). As it has been seen the charts fully coincide for small amplitudes of the external load, but the increase in the excitation amplitudes introduces the difference, and for large displacements the charts are clearly different. For a comparison, in Fig. 8.34 a chart for the exponential nonlinearity is reported. Obviously

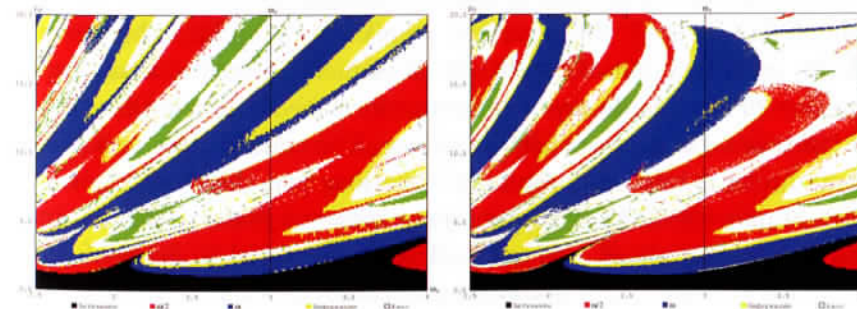


Fig. 8.33 Comparison of vibration charts.

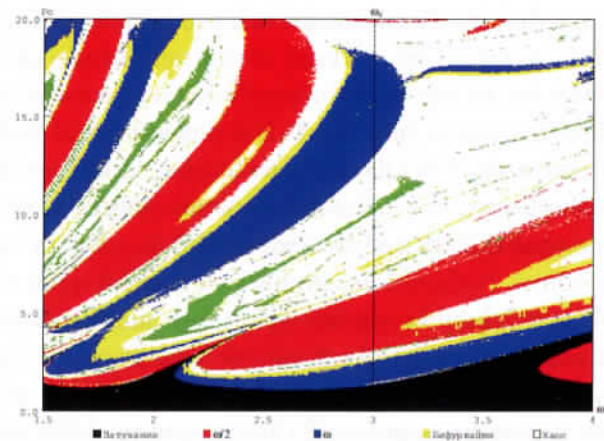


Fig. 8.34 Chart of vibration types for a physical nonlinearity in exponential form.

the nonlinearity influences the chart of vibrations, and for different types of nonlinearities considered we expect an occurrence of new effects.

In order to distinguish a difference between the geometric and physical nonlinearities and only the geometric nonlinearity more deeply, it should be observed that the beam transits from a zone of elastic deformations to a zone of plastic deformations. For this reason we have applied beam cross-sections for different time instants to follow beam deflection for different values of the amplitude of the external load for the cases of clamping (Fig. 8.35). In this figure the beam cross-section corresponding to its maximum deflection are presented for $P_0 \in [7; 20]$ with the step of $\Delta P_0 = 0.2$. This variant of the boundary initial conditions is of more interest comparing to the case of the simple beam support, since the beam has three zones of transitions into plastic deformations. The central zone and points of clamping exhibit maximum deformations and therefore beginning with amplitudes $\Delta P_0 = 7$ we observe zones of plastic deformations. For the amplitude of the external force $P_0 = 12,5$ zones of plastic deformations begin contacting with each other, and the beam exhibits the continuous strip of plasticity. One may say that about of 50% of the beam length is passed to the plastic zone. The beam

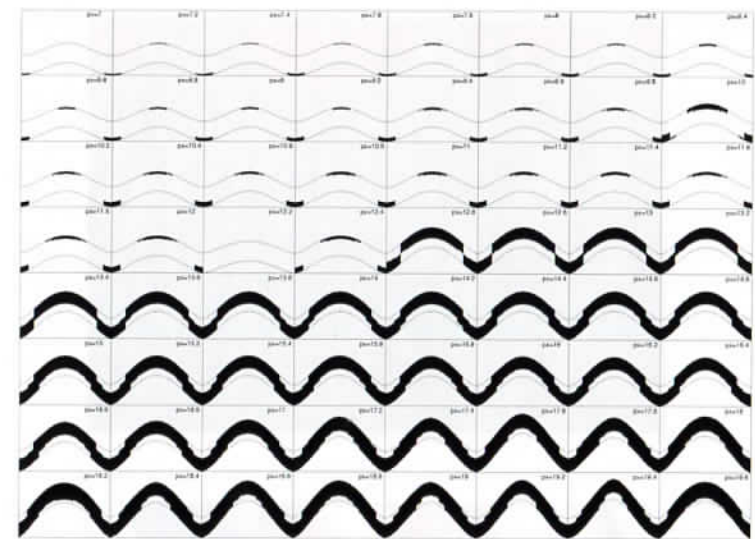


Fig. 8.35 Cross-sections of the beam deflection for various amplitudes of the external load.

cross-section can be treated in the figure symbolically, since a ratio of the linear beam dimension and its thickness equals 100. In the problems of simply supported beam the only one plastic zone is located in a neighborhood of the beam center.

The increase in the external load amplitude implies the increase in this zone and for $P_0 = 20$ the beam fully transits into the plastic zone.

In Fig. 8.36 the vibration chart for the boundary conditions (8.48) and the physical piece-wise linear characteristic is presented. In the upper chart a plasticity order in the form of color intensity of the beam is shown. White color corresponds to plastic deformations, and the chart of vibrations in these zones repeats in full the chart of the problem devoted to only geometric nonlinearities (Fig. 8.28). A chart of the plasticity order gives a possibility of estimating visually the influence of a physical nonlinearity. Plasticity zones play an important role and the given chart can be considered together with the cross-section of the beam deflections shown in Fig. 8.35. As it has been seen from the upper chart, for $P_0 = 20$ the beam practically is

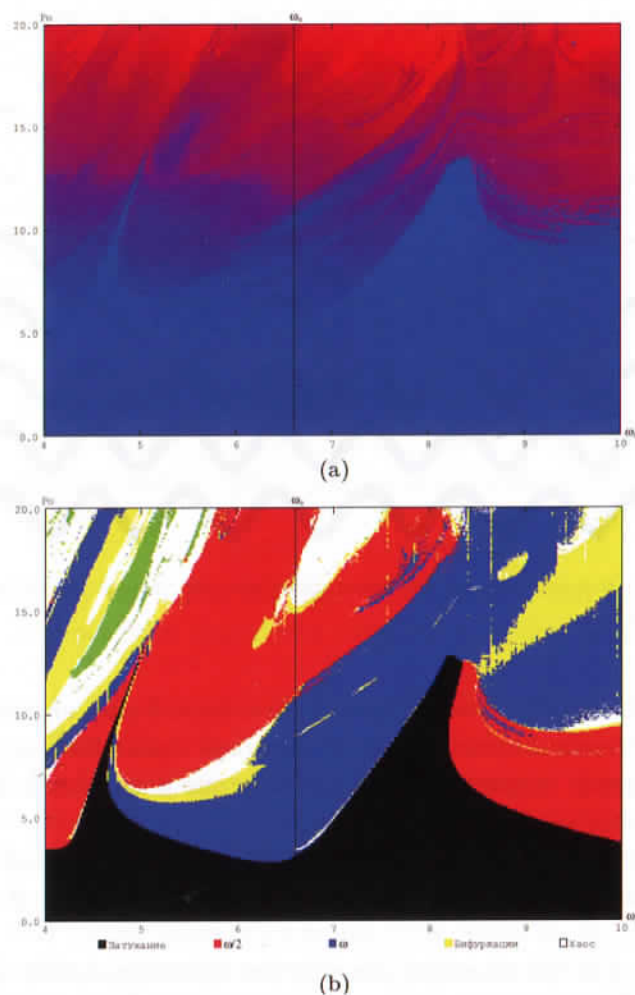


Fig. 8.36 Chart of vibrations (a) and chart of plasticity order (b).

transited in full to a plastic zone on all frequencies and vibrations for large loading amplitudes are not predicted by the applied theory.

8.1.7 On the Sharkovsky's periodicity

Investigation of chaotic regimes in models with a 3D phase space began with investigation of the Lorenz system, and nowadays

includes numerous mathematical models. They include objects from hydro- and aerodynamics, radio-physics, mechanics, chemistry, biology, economy. In addition, each branch of the mentioned sciences generates its own peculiar mathematical model being not coupled with the so far known and investigated ones. Occurrence of novel models exhibits the rich behavior of nonlinear dynamics which require classification of the detected phenomena. In fact, the rules of changes of dynamical regimes regarding local changes of the parameters can be reduced to a few typical bifurcations. If we consider a route to chaos, then the problem is reduced to a few typical scenarios of transitions or a combination of these transitions. On the other hand, global bifurcational structures of the dynamic regimes, even for the same mechanical system, but for different boundary conditions, may differ completely from each other. In other words, analyzing the bifurcation diagrams require a study of the particular mosaic elements which describe local scenarios of the transitions between different of regimes.

From the mathematical point of view, local scenarios of transition into chaos correspond to the local bifurcations or sets of such bifurcations. Then, a complex mathematical object is created, composed of hyperbolic non-trivial sets, as well as stable periodic motions. The mentioned sets are called quasi-periodic. In the above we gave an example of transition of the mechanical system into chaotic state via the Feigenbaum scenario, and we have estimated the universal Feigenbaum constants for the boundary conditions (8.48)–(8.51).

We consider a scenario of transition of the mechanical system into a chaotic state for the boundary conditions (8.49)–(8.52). We have detected not only period doubling and period tripling bifurcations, but also period quintuple, period septuple, period ninefold bifurcation phenomena. The given results are shown in Figs. 8.37 and 8.38 while partitioning of the space into parts $n = 16$ and $n = 32$, respectively. In these figures time histories $w(t)$, phase portraits $w(\dot{w})$, power spectrum, Poincaré maps $w_{t+T}(w_t)$, where T is a period of excitation (amplitudes of the exciting force are shown in the figures) are presented. In Fig. 8.37(a) in the power spectrum one

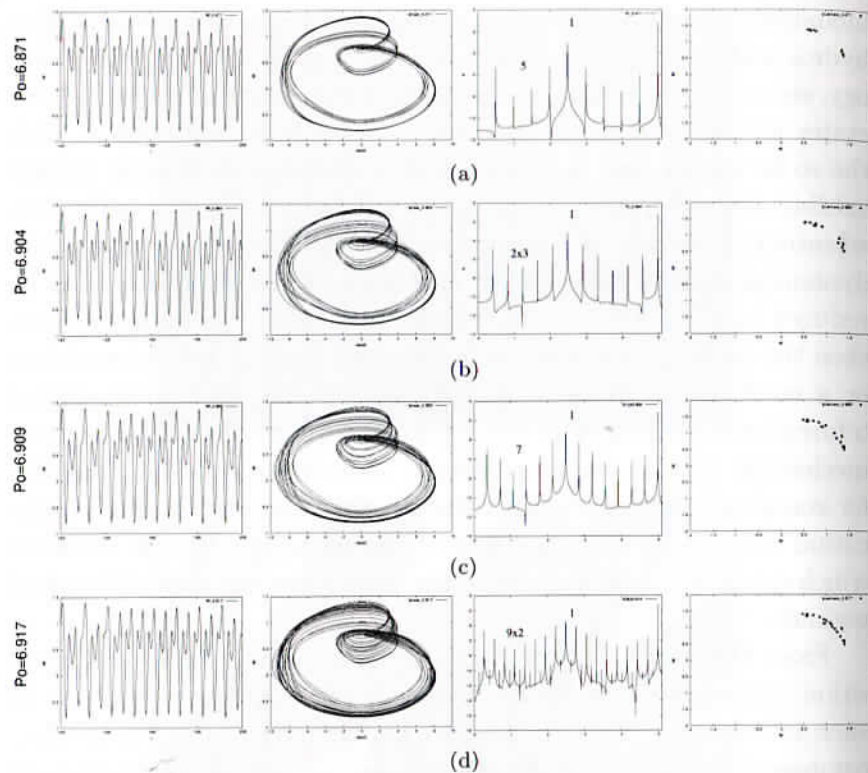


Fig. 8.37 Following Sharkovsky's periodicity: time histories, phase portraits, frequency power spectra and Poincaré maps for different P_0 : 6.871 (a), 6.904 (b), 6.909 (c), 6.917 (d) ($n = 16$).

period doubling bifurcation is clearly visible, after which the period fivefold bifurcation takes place.

In Fig. 8.37(b) in the power spectrum two period doubling bifurcations are shown (denoted by 1 and 2, respectively), and then the period tripling bifurcation occurs. Figure 8.37(c) shows one period doubling bifurcation with the following sevenfold bifurcation. Finally, in Fig. 8.37(d) after a period doubling bifurcation, the period ninefold bifurcation appears. In the latter case, in the Poincaré section, two areas of the gathered points have been transited into one area. We consider an analogous chart for the partition $n = 32$ (Fig. 8.38). Results have been presented for only one excitation frequency $\omega = 5$. Here, after first period doubling bifurcation (it is denoted by 1 in the

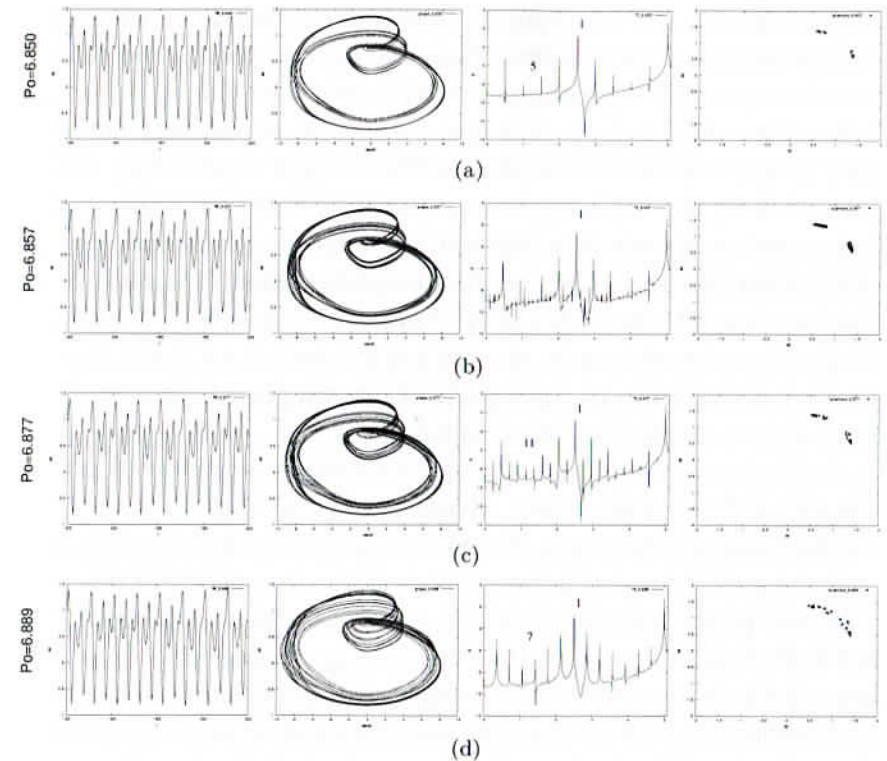


Fig. 8.38 Following Sharkovsky's periodicity: time histories, phase portraits, frequency power spectra and Poincaré maps for different P_0 : 6.850 (a), 6.857 (b), 6.877 (c), 6.889 (d) ($n = 32$).

figures), we have period fivefold and period sevenfold bifurcations [Fig. 8.38(d)] as well as a partition of the spectrum into 11 equal parts is observed [Fig. 8.38(c)].

The novel phenomenon, when the spectrum is divided not into either 2 or 3 parts, but also for more parts with creation of a strange attractor (SA), has been reported. This phenomenon is presented in the Poincaré map in the form showing collapsing of two local spaces. The interval of the parameter variation (with a step of 0.001) has been studied. The following characteristic features have been monitored. During transition from periodic vibrations to chaotic ones, a series of bifurcations appear which has more complicated scenario than that exhibited by occurrence of the amplitude peak

associated with the frequency $\frac{\omega}{2}$. This space is relatively wide. Further, a sudden transition into chaos occurs, and then a transitional zone into another regime appears. The series of bifurcations occurs before the system transits into chaos, which are of particular interest. The bifurcation interval consists of the series of short zones, and in each of them the further spectrum partition takes place into rather large number of parts. The common phenomenon for all zones is that of existence of the first period doubling bifurcation. The most dominating zones are: spectrum parts from 0 to $\frac{\omega}{2}$ and from $\frac{\omega}{2}$ to ω are divided into 5 equal parts; spectrum parts from 0 to $\frac{\omega}{2}$ and from $\frac{\omega}{2}$ to ω are divided into 11 equal parts; spectrum parts from 0 to $\frac{\omega}{2}$ and from $\frac{\omega}{2}$ to ω are divided into 7 equal parts.

In the transitional zones the spectra have non-chaotic structure, but they exhibit peaks, which are not exactly rational with respect to the fundamental frequency. The most dominating characteristic zone is that 5 and 11 located between bifurcations the spectra of this zone have two peaks associated with $\frac{\omega}{10}$ and $\frac{4\omega}{10}$, i.e. peaks corresponding to the fivefold bifurcations, but the peaks associated with $\frac{2\omega}{10}$ and $\frac{3\omega}{10}$ are substituted by pairs of the equally distant peaks [Fig. 8.38(b)].

It should be emphasized that nowadays simple models of chaotic dynamics, i.e. discrete dynamical systems are relatively well studied. For such systems a series of the theorems have been formulated, in particular, the window of period three, which corresponds to the most interesting part of the 1D map $f(x) = x^2 + c$. The following question occurs: Do other non-periodic orbits exist? The answer is given by the Sharkovsky theorem [Sharkovsky (1964)]:

Let J be the finite or infinite interval in R . We assume that the map is continuous. If there is a point of period n , then there exist a point of period k , $k > n$ belonging to the following series

$$3, 5, 7, 9, \dots \\ \dots, 2^n, \dots, 2^2, 2^1, 1.$$

Sharkovsky's theorem is applied only to the real function given in the real interval. Ten years after the work [Sharkovsky (1964)] another work has been published [Li and Yorke (1975)] for the particular case of the orbit with period-3.

One of the important achievements of this work referring to flexible beams is detection and illustration of the bifurcations sequence, which follows the Sharkovsky's rule of order.

8.1.8 Chaos — hyperchaos—hyper—hyperchaos phase transitions

We consider the evolution of the vibration regime while increasing the amplitude of the exciting force P_0 after occurrence of a strange chaotic attractor (SA). Evolution of the strange chaotic attractor with the increase in the parameter P_0 inside of a chaotic space and its associated qualitative changes are not fully investigated for mechanical systems. A general tendency of stochasticity development of chaotic set and the increase in the attractor dimension are known. A full description of chaotic dynamics governed by a system of differential equations is bounded by their number. Qualitative changes in structure of chaos exhibited by mechanical systems is not investigated in full. Analysis of the transition "chaos—chaos" does not include bifurcations in chaos associated with the increase in the LD of the analyzed attractor. Intuitively, an occurrence of the qualitative changes of the physical characteristics of an attractor due to occurrence of the positive LE is more realistic way of study than a change induced by the LD successive integer. In fact, in the case of occurrence of additional positive LE, a new unstable direction on the system trajectory appears, which should either change the system dynamics or its physical characteristics. On the other hand, Lyapunov's dimension of the local volume preserves its quantity, i.e. it is neither compressed nor extended. Note that the LD includes not only positive and zero value but also negative exponents. The latter ones are responsible for stability of various types of motion. They represent the metric properties of an attractor. In the reference [Li and Yorke (1975)] it has been shown that negative LEs are not associated with any physical characteristics of the dynamic regimes, and in general they cannot be estimated via physical experiment.

We consider a transition from a SA with one positive LE to chaos with two and three LEs, which will be called as chaos—hyperchaos and "hyperchaos—hyper—hyperchaos" transition. Moving

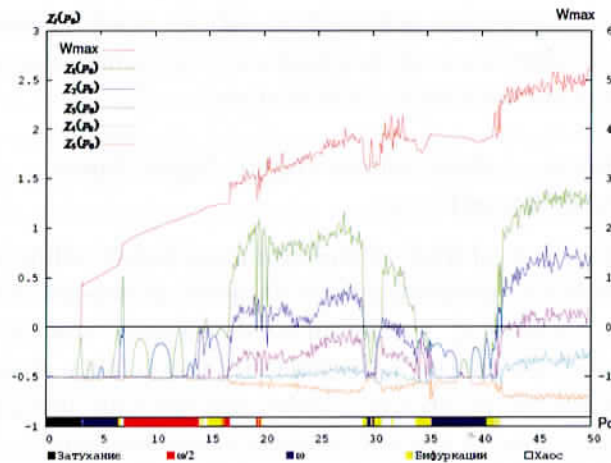


Fig. 8.39 Maximum beam deflection, power spectrum of LEs, and the vibrations scale (mixed boundary conditions).

in the hyperchaos space along the parameter P_0 two scenarios are possible: a soft transition of “chaos–hyperchaos”, when a smooth increase in the second LE does not imply any jump-type qualitative changes of the chaotic process. On the other hand a stiff transition “chaos–hyperchaos” is associated with the so far mentioned jump-type changes. It is interesting to investigate mutual dependence of the various vibration characteristics. In Fig. 8.39 the whole spectrum of parameters is presented including: $w_{\max}(P_0)$ — maximum deflection of the beam center, LEs spectrum $\{\chi_i(P_0)\}_{i=1}^5$ and a scale, characterizing the vibrations character. Analyzing simultaneously curves $w_{\max}(P_0)$ and $\{\chi_i(P_0)\}_{i=1}^5$ their mutual correspondence is observed. A change of sign of the maximum LE is associated with a series of stiff bifurcations exhibited by the curve $w_{\max}(P_0)$ and the associated color change of the attached scales. Vibrations are damped up to $P_0 = 3.3$. It is well seen on the deflection curve $w_{\max}(P_0)$. All LEs are negative, since the vibrations are stable, and they are approximately equal to $-\frac{\varepsilon}{2}$. While approaching the amplitude load value $P_0 = 3.3$, the maximum LE $\chi_1(P_0)$ begins to increase and it tends to 0. It means that the system is on a border between two regimes, and a small increase in the external amplitude of the load yields periodic vibrations. The system exhibits a first stiff bifurcation, and the maximum LE is equal

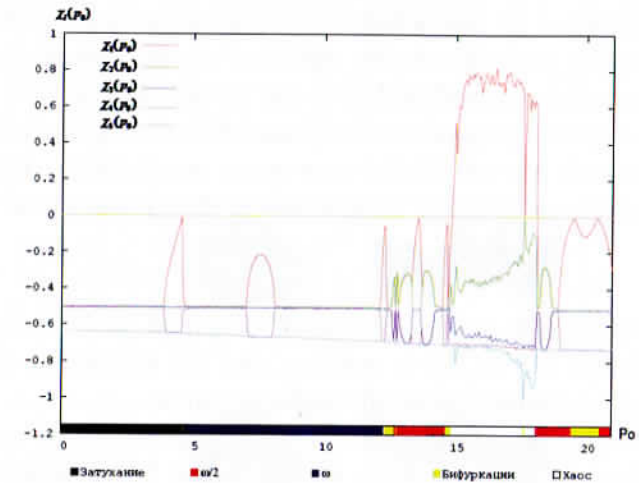


Fig. 8.40 Spectrum of the LEs in the case of clamping.

$-\frac{\varepsilon}{2}$ again. Further, an increase in the amplitude P_0 of the external load implies occurrence of a zone of periodic vibrations [3.3; 6.9]. On this interval the maximum deflection $w_{\max}(P_0)$ smoothly increases, and the maximum LE oscillates in a zone of negative values. The latter zone is finished by a series of bifurcations, and then a transition into chaos takes place. Series of bifurcations are visible on the maximum LE $\chi_1(P_0)$. Beginning of a new bifurcation is associated with the increase in $\chi_1(P_0)$ up to 0. Sudden jump on both dependence $\chi_1(P_0)$ and $w_{\max}(P_0)$ indicates the first transition of the system into a chaotic state. Positive values $\chi_1(P_0)$ in interval [6.9; 7.2] imply the system instability. This interval is presented in the scale. The next interval $P_0 \in [17.2; 29.2]$ begins with a stiff stability loss, which is well indicated on the curves $w_{\max}(P_0)$ and $\chi_i(P_0)$. Two largest LEs are positive, whereas the remaining LEs are negative, and the system exhibits hyperchaos. Finally, the hyper–hyperchaos regime takes place for $P_0 \in [42.5; 50]$. Beginning of this zone is associated with a zone of a stiff stability loss. The system transits via a series of stiff bifurcations into a hyper–hyperchaos ($\chi_1 > 0$, $\chi_2 > 0$, $\chi_3 > 0$, χ_4 increases, remaining negative, whereas χ_5 oscillates around the value of $-\frac{\varepsilon}{2}$).

Comparison of all characteristics taken into account so far yields an observation, that the results obtained via analysis of the vibration spectrum corresponds in full to the results obtained via the LEs spectrum. This correspondence has been observed on the whole considered interval. We emphasize once more peculiarities and mutual relations of the considered parameters in the characteristic system points:

- (i) In zones with stable vibrations (damped and periodic) the maximum LE $\chi_i(P_0)$ is positive, and the maximum deflection $w_{\max}(P_0)$ changes smoothly without jumps.
- (ii) In bifurcation zones (denoted on a scale by black color) the maximum LE $\chi_i(P_0)$ tends to zero value, but does not achieve a positive quantity.
- (iii) The change of regime is associated with a jump effect ($\chi_i(P_0)$ and $w_{\max}(P_0)$). Points of the system reconstruction are well visible on the vibrations scale.
- (iv) In zones with chaotic vibrations the maximum LE $\chi_i(P_0)$ is positive, and the maximum deflection $w_{\max}(P_0)$ increases via small jumps.
- (v) High correspondence between the results obtained via FFT (scale) and graphs of the maximum LE $\chi_i(P_0)$ is evident. Periodic vibrations and damped vibrations correspond to negative $\chi_i(P_0)$, whereas chaotic zones are associated with positive LE.

It should be emphasized that the so far described phase transitions “chaos–hyperchaos–hyper–hyperchaos” have been observed only in the case of the applied non-symmetric boundary conditions [Krysko *et al.* (2006)]. In Fig. 8.41 dependences $\chi_i(P_0)$ are presented for the boundary conditions of clamping type. Here a transition from the state of bifurcation into chaotic state takes place, and from the whole LEs only χ_1 changes its sign. In the chaotic regime only χ_1 and χ_2 increase, whereas the remaining LE oscillate around $-\frac{\varepsilon}{2}$. On the borders of transition from regime of bifurcations into chaos and *vice versa* all LEs oscillate. In dissipative systems with chaotic dynamics versus the control parameters and initial conditions, an

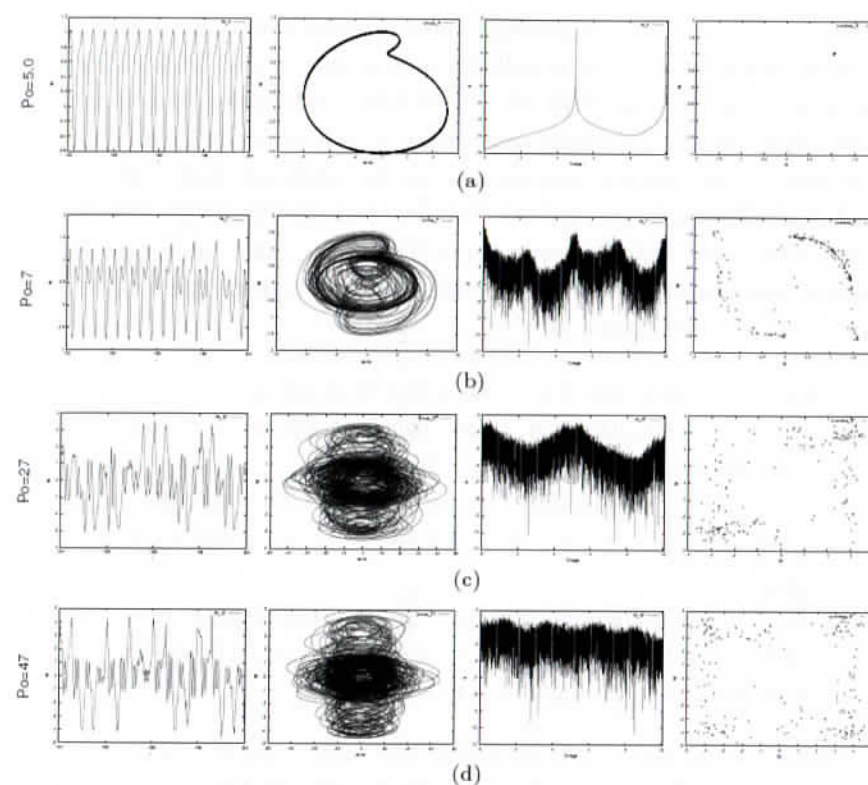


Fig. 8.41 Time histories, phase portraits, power spectra and Poincaré showing the following regimes: (a) periodic vibrations, (b) chaos, (c) chaos–hyperchaos, (d) hyper–hyperchaos.

infinite set of attractors are realized with different structures. Fixation of one of the control parameters does not change the picture: there is an infinite set of attractors and their pools of attraction are divided in the phase space by separatrix surfaces. Since in the phase space there exists a set of regular periodic regimes together with the SA, a theoretical description of the dynamics of dissipative systems is difficult.

Numerical results show that attracting pools and existence of periodic regimes in the phase space with respect to parameters decrease with the increase in their periods. It is because the cycles of large periods are not registered due to fluctuations, and an attractor does

not include periodic trajectories and becomes almost hyperbolic one. The latter attractors are called quasi-attractors, whereas the systems are called quasi-hyperbolic systems. It seems that a lack of sufficient number of rigorous results of the stochastic and ergodic theories of the quasi-attractors should be supplemented with numerical and physical experiments. In Fig. 8.41 the following dependencies are shown: time histories $w(t)$ ($180 < t < 200$), phase portraits, power spectra and Poincaré sections for the following values of the amplitude of external load:

- (i) $P_0 = 5$ — periodic vibrations, the first LE $\chi_1 > 0$;
- (ii) $P_0 = 7$ — chaotic vibrations, the first LE $\chi_1 > 0$, whereas the remaining are negative ($\chi_2 < 0$);
- (iii) $P_0 = 27$ — chaos-hyperchaos; the first and the second LE is positive ($\chi_1 > 0$, $\chi_2 > 0$), and the remaining ones are negative ($\chi_3 < 0$);
- (iv) $P_0 = 47$ — chaos-hyperchaos-hyper-hyperchaos; first, second and third LEs are positive ($\chi_1 > 0$, $\chi_2 > 0$, $\chi_3 > 0$); the remaining one is negative ($\chi_4 < 0$).

Analysis of the mentioned characteristics implies that periodic vibrations are characterized via the Poincaré map by a point, whereas the Poincaré cross sections for $P_0 = 7$ shows two independent attractors localized in different pools of the phase space without any intersection. These attractors are robust since they preserve their structure and statistical properties for small changes of the control parameters. The associated power spectrum has a broadband basis with two extrema on the excitation frequency and first subharmonic. The Poincaré map exhibits a symmetry regarding a diagonal, and the points are concentrated in two fundamental groups. Transition of the system into chaos-hyperchaos state yields a birth of the unified SA composed of both previous chaotic regimes. Independently of the initial condition choice, the unified attractor attracts trajectories of beginning in initial points, which means that the separatrix plane does not exist more. In other words, creation of unified attractor implies unification of the attraction pools of both previously separated attractors. In the Poincaré map “splashes” appear,

which means that either a new stochastic set has been born or a development of a new stochastic set in directions previously being compressed. In the power spectrum, we also observe a broadband base, but exhibiting only one extremum associated with the excitation frequency. Movement along the parameter P_0 up to $P_0 = 47$ pushes the system into *chaos-hyperchaos-hyper-hyperchaos* state. Here more dense unification of the SA is presented, and on the power spectrum there is a lack of clearly manifested local extrema. The power spectrum corresponds to the white noise and has no local extrema. Detailed investigation of the time histories $w(t)$ as well as other characteristics shows, that the system stays regularly on two attractors for $P_0 = 7$. Transition of the system into chaos-hyperchaos state ($P_0 = 27$) is realized via splashes of the positive deflections, i.e. the system exhibits the following dynamical state: stiff stability loss for negative deflections, vibrations around the equilibrium configuration and stiff stability loss for positive deflections. While the system transiting into chaos-hyperchaos state ($P_0 = 47$), vibrations are fully chaotic, i.e. the “turbulent” phenomena are observed, and there is a lack of laminar splashes. Besides of the so far mentioned characteristics, each regime can be analysed using the AF (see Fig. 8.42).

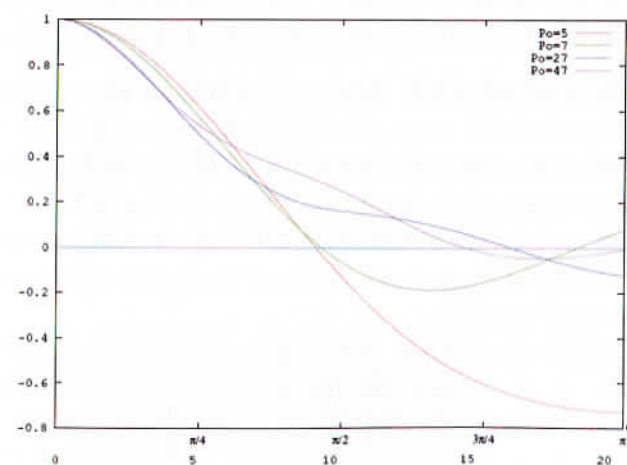


Fig. 8.42 Autocorrelation function (AF) for various dynamic regimes.

In the case of periodic regime the AF is periodic, whereas for chaotic regime the AF is fastly damped and tends to zero.

Sets of finite and non-finite dimensions having chaotic dynamics include systems with 1.5 DOFs on one end, and partial differential equation of the Navier–Stokes type on the other end [Landford (1982)]. In between both ends there are dynamical systems with increasing number of DOFs, including also the von Kármán equations considered in this book. Investigation of the mentioned dynamical systems should yield an answer to the following fundamental problem: Does any border exist in the system chaotic dynamics, where on one side the system dynamics can be called chaotic, whereas from the other side we deal with a real turbulent dynamics?

Observe that in the considered paradigm, the real turbulence does not mean any hydrodynamic phenomenon, but rather a common picture of the typical behavior of continuous systems [Landford (1982)].

8.1.9 Reliability of chaotic zones

One of the important problems regarding existence of either hyperchaotic or hyper-hyperchaotic deals with their verification. We should be sure that the discovered nonlinear effects are not yielded by peculiarity of the difference scheme or by error of the introduced method of computation of the LEs. For the problem of mixed boundary conditions, the following numerical methods have been used:

- (i) Explicit method with different partitions of n , with different computational steps dt , and with approximation of spatial derivatives of orders $O(h^2)$, $O(h^4)$, $O(h^6)$, as well as the Runge–Kutta methods RK2, RK4, RK9 have been applied.
- (ii) Implicit method with different partition n regarding space, time steps dt , and with approximation of spatial derivatives of orders $O(h^2)$, $O(h^4)$, $O(h^6)$.
- (iii) Pseudo-spectral method with different partitions n , with different time step dt , and the Runge–Kutta methods RK2, RK4, RK9 have been used.

Algorithm of estimation of the LE spectrum is applicable to the applied method being based on solutions to differential equations,

and it assumes integration of additional vectors along a phase curve. Therefore, in order to verify the explicit method we have chosen a pseudo-spectral method. Further comparison of the results obtained by these methods for different partitions regarding space and time has been carried out. All results have been obtained via RK2 method with approximation of the space derivatives with accuracy of $O(h^4)$. The choice of these parameters has been illustrated and discussed earlier, and it seems that we achieved a compromise between the speed and accuracy of the computations. In Fig. 8.43 spectra of LEs have been presented, obtained via explicit and pseudo-spectral methods for different partitions regarding spatial and timing steps. In the figures there are given also scales, obtained via the same numerical method as that used for computation of LEs spectra. Explicit method yielded results A–D, whereas the pseudo-spectral yielded the resulated denoted by E, F, G. Parameters of computations follow:

- A — explicit method; spatial partition $n = 8$, time step $dt = 2^{-8}$, derivatives approximation $O(h^4)$.
- B — explicit method; spatial partition $n = 16$, time step $dt = 2^{-8}$, derivatives approximation $O(h^4)$.
- C — explicit method; spatial partition $n = 16$, time step $dt = 2^{-9}$, derivatives approximation $O(h^4)$.
- D — explicit method; spatial partition $n = 32$, time step $dt = 2^{-11}$, derivatives approximation $O(h^4)$.
- E — pseudo-spectral method; spatial partition $n = 8$, time step $dt = 2^{-8}$.
- F — pseudo-spectral method; spatial partition $n = 32$, time step $dt = 2^{-11}$.
- G — pseudo-spectral method; spatial partition $n = 16$, time step $dt = 2^{-12}$.

Qualitative correspondence of the results obtained via various methods approves reliability of existence of hyper-hyperchaotic zones and allows to conclude that the observed phenomenon characterizes the dynamical system properly and does not depend on the applied difference scheme. One more important observation follows: maximum deflection curve $w_{\max}(P_0)$ yields information regarding the

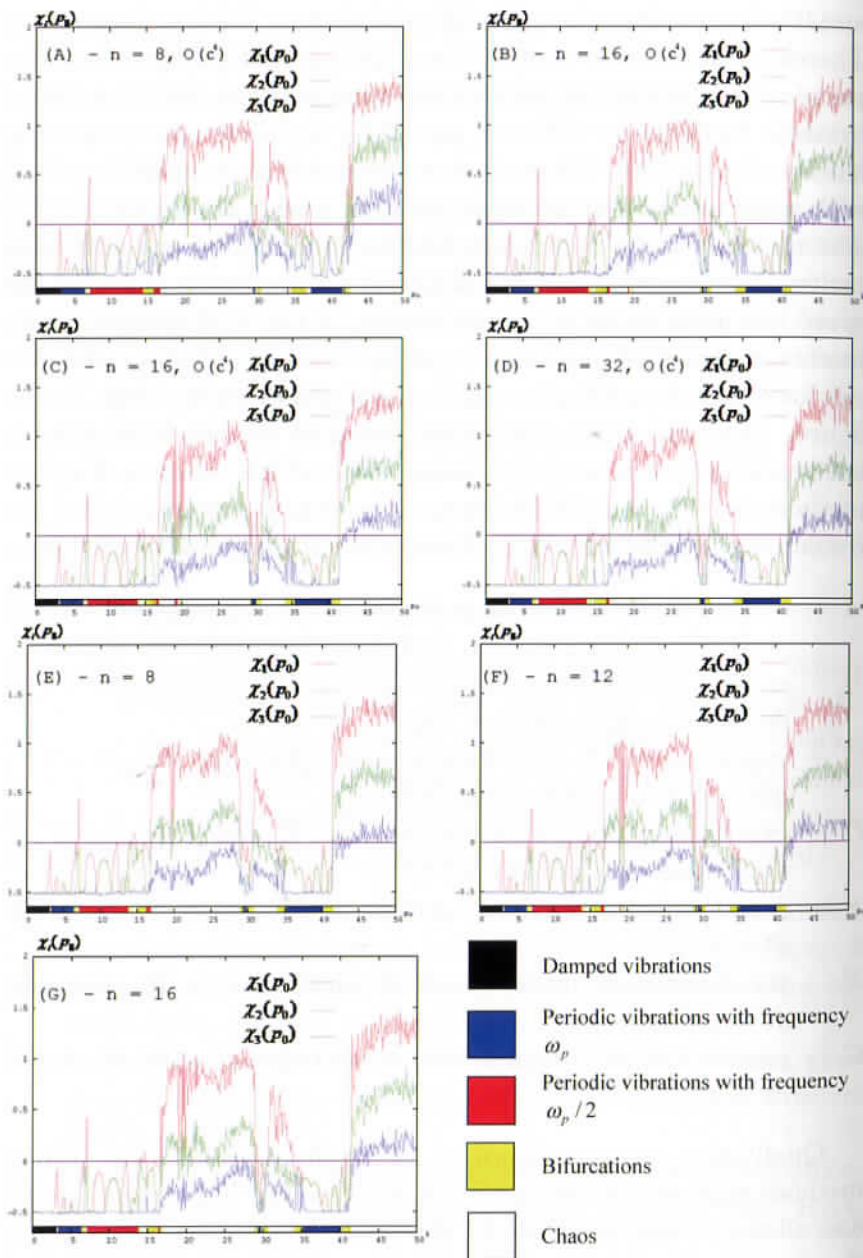


Fig. 8.43 Comparison of LE spectra for different numerical methods applied.

vibration character. This characteristic does not need any additional algorithms and it can be obtained in a rather simple manner. Simplicity in construction of a given characteristics allows to apply it from the beginning of the carried out analysis. More detailed picture can be obtained by adding additional “scale” characteristic constructed on the basis of FFT and LE spectrum.

We have also compared a chart of vibrations with a chart of chaotic, hyper-chaotic and hyper-hyperchaotic zones, based on the LE spectrum (see Fig. 8.44). Observation of the charts yields

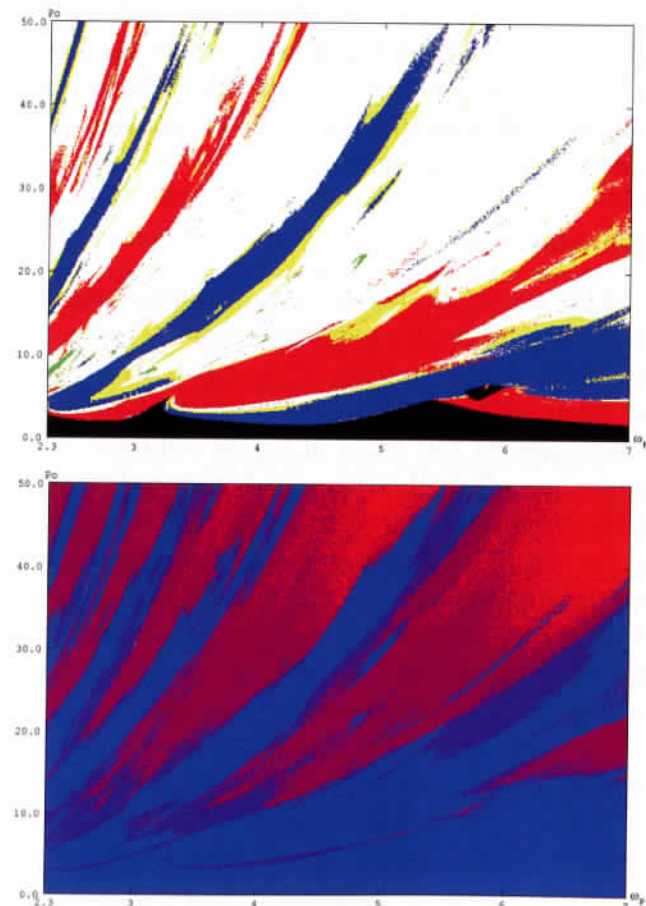


Fig. 8.44 Charts of vibrations: chaotic, hyperchaotic and hyper-hyperchaotic zones.

the following conclusion. Chaotic zone is the widest and zones of hyper-chaos and hyper-hyperchaos are located in it. The hyper-hyperchaos phenomenon occurs for large amplitudes of the external force for high excitation frequencies. Comparison of both charts allows to validate the carried out analysis of the basis of FFT, since zones with chaos correspond to zones with positive LE. It is obvious that charts coincide with each other. The first chart brings the additional information on the periodic vibrations, and it allows to divide zones with separate harmonic and subharmonic $\frac{\omega}{2}$ zones. Chart of the LE yields more detailed picture of chaotic zones putting emphasis on the chaotization strength that they are the parameters (P_0, ω) . Coincidence of the borders of the fundamental zones allows to conclude that the analysis carried out on a basis of FFT yields the results being in agreement with other methods, and can be applied to estimate the general chart of the system dynamics.

8.1.10 Conclusions

This part yields results of the numerical computation of the vibrations of infinitely long flexible panels subjected to the external parametric load. At first, the problem of the reliability of the numerical results has been addressed. For the problem of simply supported beam we have applied the BGM in higher approximations for two physical processes — free vibrations and buckling phenomenon. Coincidence of the experimental and analytical results implies the results reliability. For the BGM it is required to estimate a number of the series terms to get the reliable results. The experience has shown that we may achieve only the integral convergence. Therefore, the whole further analysis is carried out on a basis of the vibrations power spectrum associated with the beam center. Owing to the so far described approach a methodology of the charts construction has been developed. Note that for the problem regarding the parametric transversal load the practical convergence of the BGM is achieved already for two terms of the series. The beam parametric vibrations have served as an example to study the charts of vibrations, the fundamental vibration regimes, and to investigate a transition into chaos and the

system evolution within a chaotic dynamics. We have detected a transition into chaos through the Feigenbaum scenario, and we have traced eight period doubling bifurcations. In the chaotic zone we have distinguished Smale, Shilnikov and Rössler attractors.

The BGM has been used to control the validity and reliability of the pseudo-spectral method on Chebyshev's mesh. In particular, the problems regarding convergence for the different approximations, spatial partitions, and time steps have been addressed. Results yielded by all methods have been compared with each other on a basis of the integral 3D charts. Good correspondence of all results obtained through the applied methods has been presented. Particular attention has been paid to the problem of integral convergence of the difference scheme with respect to the approximation order of the difference derivatives, i.e. $O(h^2)$, $O(h^4)$ and $O(h^6)$. Optimality of the approximation $O(h^4)$ to solve PDEs governing problems in mechanics has been demonstrated. The problem of a usage of explicit versus implicit schemes has been outlined.

FDM has been used to solve problems with the beam clamping. As in the case of the beam simple support, the period doubling route to chaos has been illustrated, and the system dynamical peculiarities in a chaotic regime has been investigated. A period tripling bifurcation has been also demonstrated.

Besides the problem of parametric vibrations of the flexible panels of infinite length with the geometric nonlinearity, we have included into considerations also the physical material nonlinearity. We have considered two variants of the stress-strain relation, i.e. in the form of two piece-wise linear characteristic and in the form of the exponential transition into a plastic zone. For both variants the vibration charts for the problem of clamped beam have been constructed. In the case of the simply supported beam wider spectrum of the characteristics has been applied: maximum deflection, maximum LEs and scales. While solving the problems with physical nonlinearities, we have added a novel parameter — plastic zone.

Owing to analysis of the plastic zone, a notion of plasticity global order of the beam has been introduced. Namely, we have investigated beam vibrations up to its transitions into a plastic zone.

In this chapter part novel results of theory of nonlinear mechanical systems have been presented. At first, a route to chaos due to Sharkovsky's smooth scenario has been illustrated and discussed. On the contrary to the Feigenbaum scenario, our dynamical system transits into chaos via a cascade of the period doubling bifurcation, and via the sequence governed by Sharkovsky's order. Earlier the similar transitions have been discovered only for discrete maps, and hence the reported result is novel from a point of view of nonlinear dynamics. For the case with non-symmetric boundary conditions, we have detected the unique phenomenon not exhibited by other nonlinear dynamical systems. Namely, three LEs have got positive values (hyper-hyperchaos). Each of the regimes have been analyzed using the fundamental characteristics. Simultaneous analysis of LE, maximum deflection, vibrations of the beam center, phase portraits, power spectra, Poincaré maps and the AF imply the increase in the chaotization process corresponding to the increase in a number of positive LE. We have paid attention to the reliability of the obtained results. Comparison of the results of the explicit method, with different space partition as well as the pseudo-spectral method on a Chebyshev's mesh approves that the chaos-hyperchaos phenomenon is the real property of our studied system, and not the error introduced by the applied numerical method. The simultaneous analysis of the charts of vibrations and charts of chaotic, hyperchaotic and hyper-hyperchaotic zones has been carried out.

Numerical experiments showed a larger efficiency of the applied numerical methods and the used algorithms. The obtained results are new from a point of view of nonlinear mechanics and they await experimental improvement.

8.2 Cylindrical Panels of Infinite Length

8.2.1 Problem formulation

We consider elastic isotropic shells of infinite length, i.e. a shell material satisfies the Hooke's law. In addition, we take into account the

geometric nonlinearity, i.e. the relation between deformations of middle surface and displacements has the following form

$$\varepsilon_x = \frac{\partial u}{\partial x} - k_x w + \frac{1}{2} \left(\frac{\partial w}{\partial x} \right)^2. \quad (8.149)$$

Full deformations of an arbitrary point ε_x^z is a sum of deformations in middle surface ε_x and bending deformation ($\varepsilon_x^z = \varepsilon_x + \varepsilon_{x,u}$), which owing to the Kirchhoff-Love hypothesis, is as follows

$$\varepsilon_{x,u} = -z \frac{\partial^2 w}{\partial x^2}. \quad (8.150)$$

Let us consider a process of shell motion in time interval t_0 and t_1 . We compare different trajectories of system points between the initial t_0 and final t_1 positions. Real trajectories are defined by the following relation

$$\int_{t_0}^{t_1} (\delta K - \delta \Pi + \delta' W) dt = 0. \quad (8.151)$$

Here K stands for the system kinetic energy, Π is the potential, whereas $\delta' W$ is the sum of elementary works of the external forces. In the case when all forces acting on the system have a potential, Eq. (8.151) takes the form

$$\delta S = \delta \int_{t_0}^{t_1} (K - \Pi) dt = 0, \quad (8.152)$$

where $S = \int_{t_0}^{t_1} (K - \Pi) dt$ is the Hamilton action. After standard transformations, the non-dimensional counterpart form of equations regarding displacements follows

$$\begin{aligned} \frac{\partial^2 u}{\partial x^2} - k_x \frac{\partial w}{\partial x} + \frac{\partial w}{\partial x} \frac{\partial^2 w}{\partial x^2} + p_x - \frac{\partial^2 u}{\partial t^2} = 0, \\ - \frac{1}{12} \frac{\partial^4 w}{\partial x^4} + \frac{\partial w}{\partial x} \left(\frac{\partial^2 u}{\partial x^2} - k_x \frac{\partial w}{\partial x} + \frac{\partial w}{\partial x} \frac{\partial^2 w}{\partial x^2} \right) \\ + \left(k_x + \frac{\partial^2 w}{\partial x^2} \right) \left(\frac{\partial u}{\partial x} - k_x \frac{\partial w}{\partial x} + \frac{1}{2} \left(\frac{\partial w}{\partial x} \right)^2 \right) \\ + q - \frac{1}{12} \frac{\partial^2 w}{\partial t^2} - \varepsilon \frac{\partial w}{\partial t} = 0. \end{aligned} \quad (8.153)$$

The following relation between dimensional and non-dimensional quantities holds

$$\bar{k}_x = \frac{a}{R_x} \frac{1}{\lambda}, \quad p_x = \frac{E}{1-\nu^2} \lambda^3 \bar{p}_x, \quad q = \frac{E}{1-\nu^2} \lambda^4 \bar{q}, \quad \lambda = \frac{h}{a},$$

$$t = a \sqrt{\frac{(1-\nu^2)\gamma}{Eg}} \bar{t}, \quad u = \bar{u} \lambda^2, \quad x = a \bar{x}, \quad (8.154)$$

where parameters with bars correspond to non-dimensional quantities. In Eq. (8.153) the bars are already omitted. In relations (8.154) the following notation is applied: E is the elasticity modulus, ν is the Poisson's coefficient, γ is the material density, g is the Earth acceleration, q is the transversal load (function of x and t), h and a are thickness and linear shell dimension, respectively, w and u stand for deflection and displacement of the middle surface, respectively, and $k_x = \frac{1}{R_x}$ is the shell curvature.

System of PDEs (8.153) should be supplemented by boundary and initial conditions.

Boundary conditions are as follows:

1. Pinned support

$$u = w = \frac{\partial^2 w}{\partial x^2} = 0, \quad \text{for } x = 0; 1. \quad (8.155)$$

2. Fixed support

$$u = w = \frac{\partial w}{\partial x} = 0, \quad \text{for } x = 0; 1. \quad (8.156)$$

3. Pinned-fixed (mixed) support

$$\begin{aligned} \text{for } x = 0 \quad u = w = \frac{\partial^2 w}{\partial x^2} &= 0, \\ \text{for } x = 1 \quad u = w = \frac{\partial w}{\partial x} &= 0. \end{aligned} \quad (8.157)$$

Initial conditions for $t = 0$ follow:

$$u = f_1(x), \quad \dot{u} = f_2(x), \quad w = f_3(x), \quad \dot{w} = f_4(x). \quad (8.158)$$

8.2.2 Solution and its reliability

We approximate the partial derivatives regarding x in system (8.153) by difference relations with the error of $O(h_1^4)$ using the Taylor series in vicinity of the point x_i of order h_1 , where h_1 is the partition step of $x \in [0, 1]$:

$$G_{h_1} = \left\{ 0 \leq x_i \leq 1, x_i = ih_1, i = 0, \dots, N, h_1 = \frac{1}{N} \right\}. \quad (8.159)$$

In this case PDEs (8.153) are reduced to second-order ODEs with respect to time for an i th point of the interval $[0, 1]$:

$$\begin{aligned} \ddot{u}_i &= \Lambda_{x^2}(u_i) - \Lambda_x(w_i)(k_x - \Lambda_{x^2}(w_i)) + p(ih_1, t), \\ \ddot{w}_i + \varepsilon \dot{w}_i &= \lambda^2 \left(-\frac{1}{12} \Lambda_{x^4}(w_i) + \Lambda_x(w_i)(\Lambda_{x^2}(u_i) \right. \\ &\quad \left. - \Lambda_x(w_i)(k_x - \Lambda_{x^2}(w_i))) \right) + (\Lambda_{x^2}(w_i) + k_x)(\Lambda_x(u_i) \\ &\quad \left. - k_x w_i + 0.5(\Lambda_x(w_i))^2) + q(ih_1, t). \end{aligned} \quad (8.160)$$

The following difference operators are introduced:

$$\begin{aligned} \Lambda_x(\cdot)_i &= \frac{-(\cdot)_{i+2} + 8(\cdot)_{i+1} - 8(\cdot)_{i-1} + (\cdot)_{i-2}}{12h_1} = \left(\frac{\partial(\cdot)}{\partial x} \right)_i + O(h_1^4), \\ \Lambda_{x^2}(\cdot)_i &= \frac{-(\cdot)_{i+2} + 16(\cdot)_{i+1} - 30(\cdot)_i + 16(\cdot)_{i-1} - (\cdot)_{i-2}}{12h_1^2} \\ &= \left(\frac{\partial^2(\cdot)}{\partial x^2} \right)_i + O(h_1^4), \\ \Lambda_{x^4}(\cdot)_i &= \frac{-(\cdot)_{i+3} + 12(\cdot)_{i+2} - 39(\cdot)_{i+1} + 56(\cdot)_i - 39(\cdot)_{i-1} \\ &\quad + 12(\cdot)_{i-2} - (\cdot)_{i-3}}{6h_1^4} \\ &= \left(\frac{\partial^4(\cdot)}{\partial x^4} \right)_i + O(h_1^4). \end{aligned} \quad (8.161)$$

The difference forms of the boundary and initial conditions follow

1. Pinned support

$$u_i = w_i = \Lambda_{x^2}(w_i) = 0, \quad i = 0; N. \quad (8.162)$$

2. Fixed support

$$u_i = w_i = \Lambda_x(w_i) = 0, \quad i = 0, \dots, N. \quad (8.163)$$

3. Mixed support (8.157) is a combination of boundary conditions (8.162) and (8.163). Initial conditions have the form

$$u_i = w_i = \Lambda_{x^2}(w_i) = 0, i = 0; N(x = 0), \quad (8.164)$$

$$u_i = w_i = \Lambda_x(w_i) = 0, i = 0; N(x = 1),$$

$$u_i = f_1(ih_1), \dot{u}_i = f_2(ih_1), w_i = f_3(ih_1), \dot{w}_i = f_4(ih_1). \quad (8.165)$$

System of second-order ODEs (8.160) is then transformed to a system of first-order ODEs, and then it is solved with the RK4 method. Numerical convergence of the method with respect to the space coordinate x and time t has been investigated. In Table 8.6 a time history $w(0.5; t)$, phase portrait $w(\dot{w})$ and power spectrum $S(\omega)$ for different partitions of spatial coordinate x and with respect to time t and action of harmonic transversal load $q(x, t) = q_0 \sin \omega_q t$, $q_0 = 500$, $\omega_q = 0.46$ ($k_x = 48$, $\varepsilon = 0.1$) are reported.

Analysis of the given results shows that in order to get practically the exact solution it is sufficient to use interval $[0, 1]$ partition with $N = 16$. Applying the Runge principle and observing the

Table 8.6 Time histories, phase portraits and power spectra for different N (periodic vibrations).

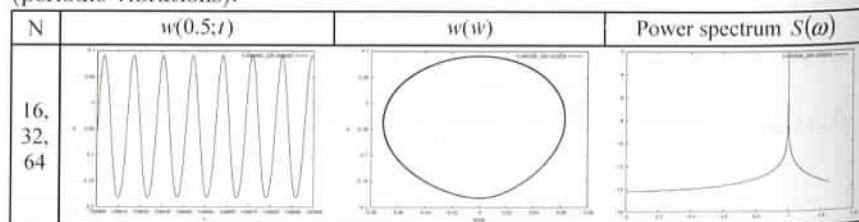
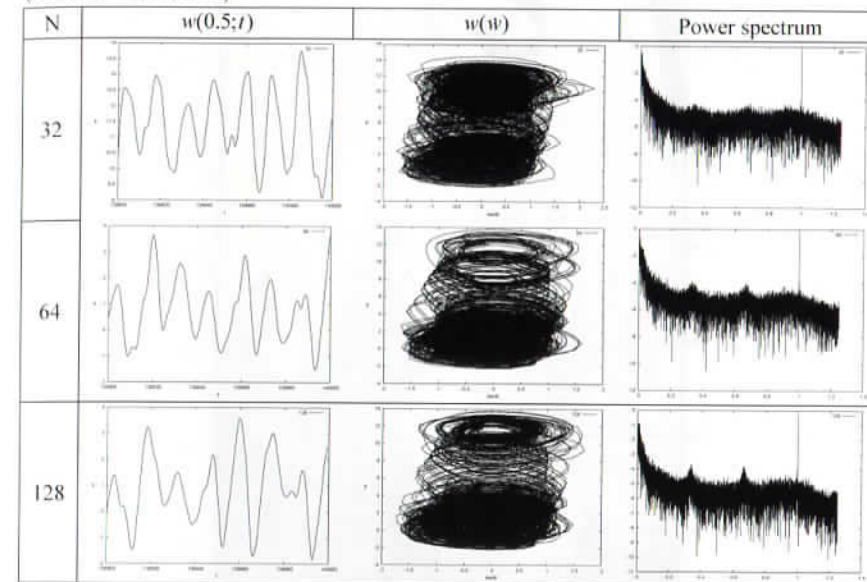


Table 8.7 Time histories, phase portraits and power spectra for different N (chaotic vibrations).



results given in Table 8.6, one may conclude that taking different $N = 32; 64; 128$ does not introduce any changes to the time histories $w(0.5, t)$, phase portraits $w(\dot{w})$ and power spectra $S(\omega)$.

A similar investigation is carried out when the system exhibits a chaotic regime. In Table 8.7 the same characteristics as in Table 8.6 for $q_0 = 3,500$ and $\omega_p = 0.46$ are presented.

It is clear that though the signals for different partitions do not coincide, their integral characteristics, phase portraits and power spectra practically coincide. Therefore, the further numerical computations have been carried out for $N = 32$.

8.2.3 LEs

In order to detect particularities of the cylindrical panel vibrations we construct the charts on control parameters $\{q_0, \omega_p\}$ plane (Figs. 8.45 and 8.46). The method of charts construction has been based on the power spectrum analysis and the largest LE. Figure 8.45 reports the chart in full, whereas in Fig. 8.46 only its part marked as A

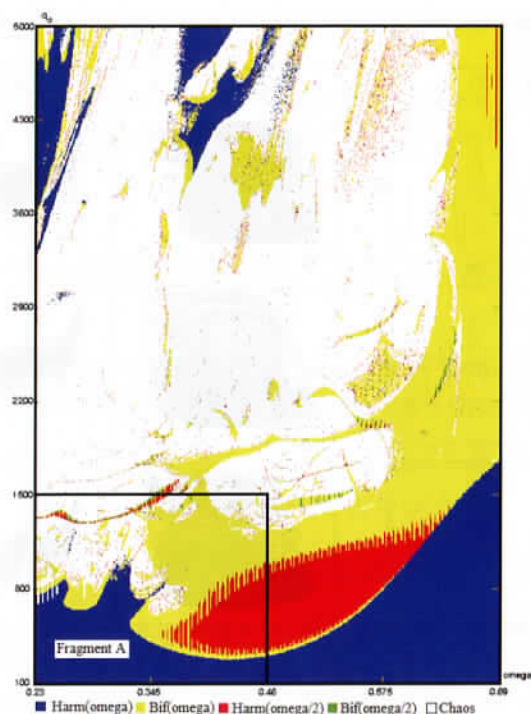


Fig. 8.45 Charts of panel vibrations.

is shown. In order to construct the chart shown in Fig. 8.45 the plane of $\{q_0, \omega_p\}$ parameters have been divided by a mesh of steps $\{4, 0.00115\}$.

Application of the LE computation plays an important role in theory of Hamilton and dissipative dynamical systems, since they allow to measure stochasticity magnitude. In addition, there exist a dependence of LE on other dynamical characteristics like the Kolmogorov entropy or a fractal dimension.

It should be emphasized that LEs characterize the averaged velocity of the exponential divergence of the neighborhood trajectories (see [Wolf *et al.* (1985)]). We follow here the method developed by Benettin *et al.* [Benettin *et al.* (1976, 1980)]. We transform Eq. (8.161) to its normal counterpart form:

$$\frac{du_i}{dt} = U_i, \quad \frac{dw_i}{dt} = W_i,$$

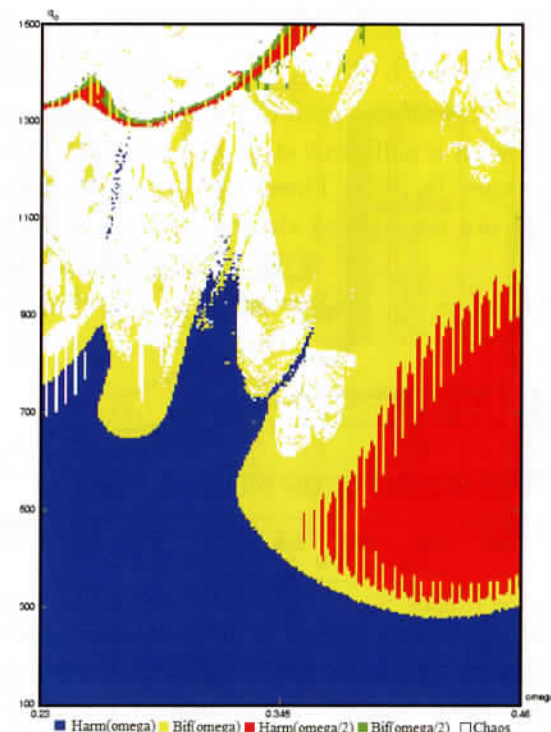


Fig. 8.46 Charts of panel vibrations (window A).

$$\begin{aligned} \frac{dU_i}{dt} &= \Lambda_{x^2}(u_i) - \Lambda_x(w_i)(k_x - \Lambda_{x^2}(w_i)) + p(ih_1, t), \\ \frac{dW_i}{dt} &= -\varepsilon W_i + \lambda^2 \left(-\frac{1}{12} \Lambda_{x^4}(w_i) + \Lambda_x(w_i)(\Lambda_{x^2}(u_i) \right. \\ &\quad \left. - \Lambda_x(w_i)(k_x - \Lambda_{x^2}(w_i))) + (\Lambda_{x^2}(w_i) + k_x)(\Lambda_x(u_i) \right. \\ &\quad \left. - k_x w_i + 0.5(\Lambda_x(w_i))^2) + q(ih_1, t), \right. \\ &\quad \left. i = 1, \dots, N-1. \right. \end{aligned} \quad (8.166)$$

For the given problem the method of finding all $4(N-1)$ LE relies on the following approach. We take orthonormal system of $4(N-1)$ vectors of dimension $4(N-1)$:

$$\{v_i^0, \|v_i^0\| = 1, (v_i^0, v_j^0) = \delta_{ij}, i, j = 1, \dots, 4(N-1)\}. \quad (8.167)$$

For simplicity, we take the following vectors:

$$(1, 0, \dots), (0, 1, 0, \dots), (0, 0, 1, \dots), \dots, (0, 0, 0, \dots, 1). \quad (8.168)$$

Along a trajectory of the system motion we compute a differential of the map with a sufficient step, given by Eq. (8.167), regarding each of vectors (8.168). Then, the obtained vectors $\{\bar{v}_i^k, i = 1, \dots, 4(N-1)\}$ are normalized via the Gramm–Schmidt procedure

$$\alpha_1^k = \|\bar{v}_1^k\|, v_1^k = \frac{\bar{v}_1^k}{\alpha_1^k}, \quad \alpha_i^k = \left\| \bar{v}_i^k - \sum_{j=1}^{i-1} (v_j^k, \bar{v}_i^k) v_j^k \right\|, \quad (8.169)$$

$$v_i^k = \frac{\bar{v}_i^k - \sum_{j=1}^{i-1} (v_j^k, \bar{v}_i^k) v_j^k}{\alpha_i^k}, i = 2, \dots, 4(N-1).$$

Finally, LEs are defined by the following formula

$$\lambda_i = \lim_{k \rightarrow \infty} \frac{1}{k \delta t} \sum_{j=1}^k \ln \alpha_i^j. \quad (8.170)$$

In what follows we investigate a problem of dynamical stability loss of the shell subjected to harmonic load and uniformly distributed along the shell surface, whose natural frequency is $\omega_0 = 0.46$.

In Fig. 8.47 the dependence $w_{\max}(q_0)$ for the shell center ($x = 0.5$) — point A and for ($x = 0.75$) — point B are shown. In addition, two characteristics $\lambda_1(q_0)$ for the shell center ($x = 0.5$) — point A are reported. Besides, in Fig. 8.47, in window E, there is the vibration scale part versus q_0 and $\lambda_i(q_0)$, ($i = 1, 2, 3$) regarding the interval $4,000 \leq q_0 \leq 5,000$. In the scale showing the vibration type versus q_0 zones a, b, c, d, e, f are distinguished, which should be analyzed in a more detailed manner (we deal with so-called peculiar zones). In the interval $0 \leq q_0 \leq 1,247.3223$ the shell exhibits periodic vibrations with ω_0 and $\omega_0/2$, transiting into a zone of bifurcations. Period doubling bifurcations have been monitored up to $q_0 = 1,247.3223$ (see Table 8.8). Increasing q_0 up to $5 \cdot 10^{-5}$ the mechanical system is transited into chaos owing to the Ruelle–Takens–Newhouse scenario on the two frequencies for $q_0 = 1,247.32235$ (see point A). Owing to the Ruelle–Takens–Newhouse theorem, chaos appears after two Hopf bifurcations, and then a SA exhibiting a complex topology and bounded by non-smooth manifolds occurs.

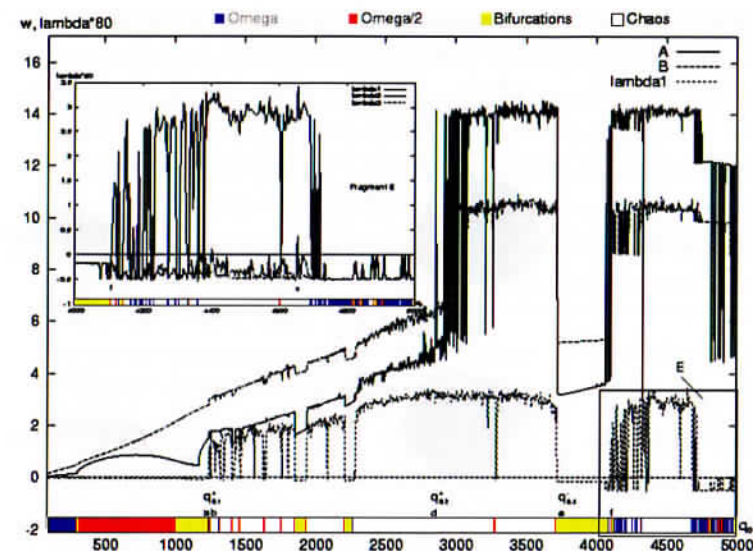
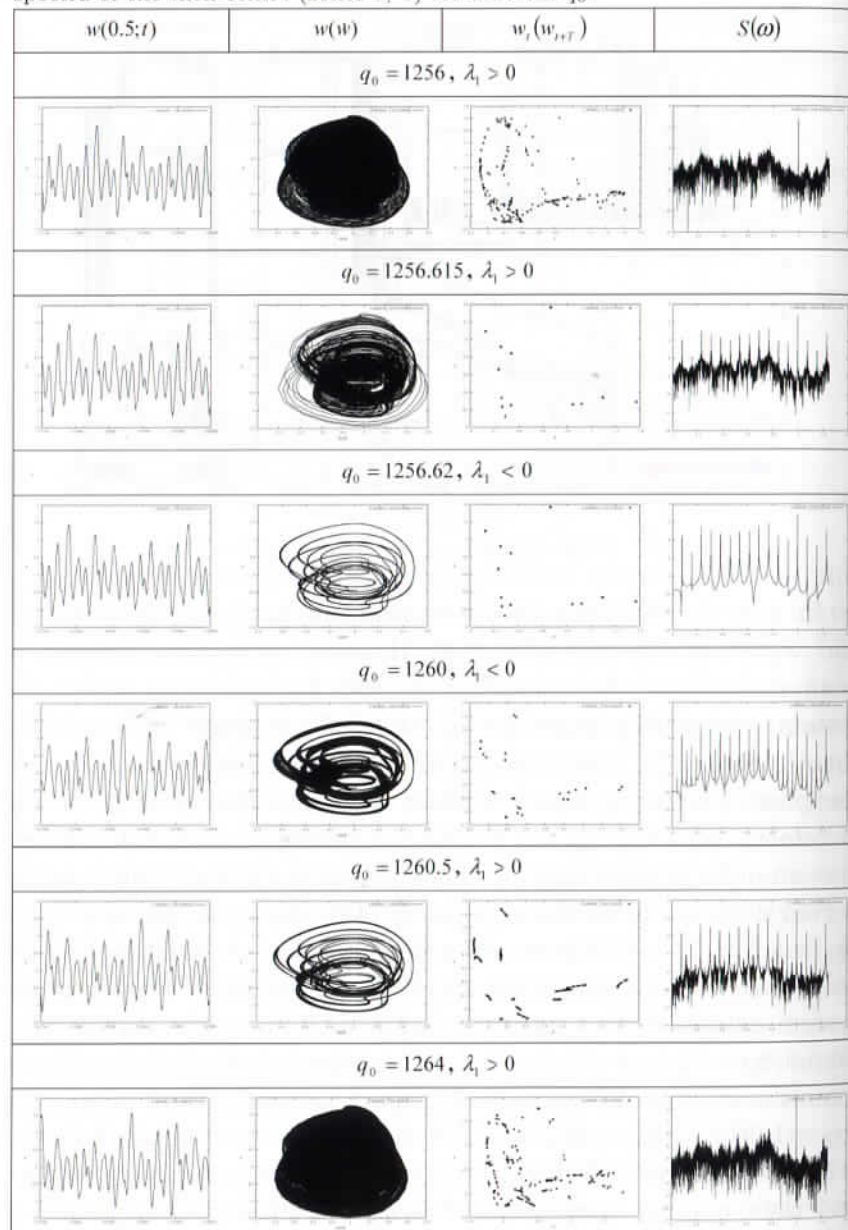


Fig. 8.47 Dependence $w_{\max}(q_0)$ and $\lambda_i(q_0)$, $i = 1, 2, 3$.

In zone a, the first-order discontinuity in $\lambda_1(q_0)$ is observed, and $\lambda_1 > 0$, $\lambda_2 < 0$, $\lambda_3 < 0$. However, a sudden increase in beam deflections is not observed. Further increase in q_0 pushes the system into a deep chaos for $q_0 = 1,256$ — signal $w(t)$ exhibits chaotic character, power spectrum has a broadband base, whereas the phase portrait presents a black spot. The change of q_0 on the increment of 0.615 ($q_0 = 1,256.615$) pushes the shell vibrations into an ordered deterministic chaos, which is built via thirteen-fold period doubling bifurcation ($\lambda_1 > 0$). The change of q_0 on $5 \cdot 10^{-3}$ ($q_0 = 1,256.62$) yields more ordered vibrations exhibited by the signal, phase portrait and power spectrum. A particular feature of the system exhibited by a narrow window of bifurcations of the mentioned type ($\lambda_i(q_0) < 0$, ($i = 1, 2, 3$)) is reported. Further increase in q_0 on the amount of 0.4 causes the occurrence of the Hopf bifurcation ($q_0 = 1,260$, $\lambda_i(q_0) < 0$, $i = 1, 2, 3$), and hence the Sharkovsky order of $2 \cdot 13$ takes place. SA illustrated by Poincaré map begin to increase, and their number increase too. For $q_0 = 1,260.5$ (i.e. increasing q_0 an amount of 0.5), the shell transits again into the chaotic regime on the frequencies of the last Hopf bifurcation, i.e. Sharkovsky's order of

Table 8.8 Time histories, phase portraits, Poincaré maps and frequency power spectra of the shell centre (zones a, b) for different q_0 .



2.13 is exhibited. Step by step the chaos is transited into deep chaos, which is manifested by signal $w(t)$, dark spot in the phase portrait as well analogous picture of the power spectrum as it happened for $q_0 = 1,256$ ($\lambda_1 > 0$, $\lambda_2 < 0$, $\lambda_3 < 0$). The so far given description is related to zone *b* (see Table 8.7). Maximum shell deflection in zones *a* and *b* is practically the same, i.e. no sudden increase in shell deflection is observed in comparison to that regarding the static stability loss. The value $q_{0,1}^+ = 1,256$ estimates the occurrence of the first dynamical critical load.

8.2.4 Chaos–hyperchaos transition

We investigate the evolution of the vibrational regime of the shell increasing amplitude q_0 of the harmonic load. It should be mentioned that the problem of chaotic attractor evolution with the increase in the parameter q_0 is rather rarely investigated.

Our investigations allowed to discover rich nonlinear dynamical features of the investigated shell, including that the smoothing of the power spectrum is bounded due to the system characteristics, in particular, due to a number of governing differential equations, the attractor dimension computation, as well as synchronization processes. It is known that qualitative changes in a chaotic structure can already appear in systems with 1.5 DOFs. In the theory of shells, though D_L (LD) [Awrejcewicz *et al.* (2004)] is computed via LPE, there is no unique relation between the signature of the LPE spectrum and the D_L of a SA.


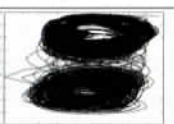


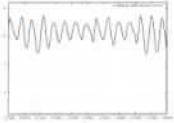
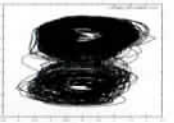
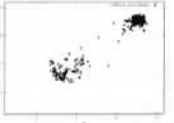

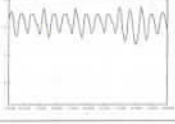
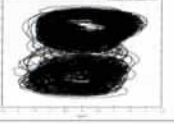
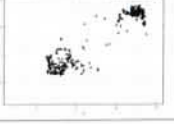

Intuitively, occurrence of qualitative changes in the physical characteristics of an attractor through the birth of an additional LE is more realistic than the analogous reconstruction using the concept of D_L . In fact, in the case of occurrence of an additional positive LE there is a new unstable direction on the system trajectory, which implies the qualitative new system dynamics. On the other hand, the LD defines the averaged local volume preserving its quantity, i.e. neither compressed nor extended. Observe that the LD includes not only positive and zero exponents, but also negative ones. Though the latter ones may be responsible for stability of any motion type, for the steady-state motion they do not influence the system dynamics,

since they rather define only metric properties of the attractor. It has been shown in the reference [Wolf *et al.* (1985)], that in general negative LE cannot be estimated through physical experiments approving our remark that they do not influence the physical characteristics of dynamical regimes.

In what follows, we consider transitions into chaos while changing patterns of the LE spectrum, as well as transitions of system dynamics with one positive LE into chaos with two positive LEs, i.e. into hyperchaos. The latter transitions within chaotic regimes are referred as chaos–hyperchaos transitions. The so far described phenomenon for the case of flexible plates subjected to harmonic load has been reported in reference.

In Table 8.9, time history $w(t)$, $w(\dot{w})$, Poincaré map $w_t(w_{t+T})$ and the power spectrum of the central shell point driven harmonically by $q_0 \sin(0.46t)$ are reported. The mentioned characteristics are given for three values of $q_0^{(1)} = 4,648$, $q_0^{(2)} = 4,652$ and $q_0^{(3)} = 4,656$, and the mentioned loads are denoted by area C on the dependence $\lambda(q_0)$ in Fig. 8.47. For q_0^1 : $\lambda_1 > 0, \lambda_2 < 0$, q_0^2 : $\lambda_1 > 0, \lambda_2 > 0$, q_0^3 : $\lambda_1 > 0, \lambda_2 < 0$, i.e. when we deal here with three equilibrium configurations. Namely, for q_0^1 and q_0^3 the system is in a chaotic regime, whereas for q_0^2 the unification of both attractors takes place

Table 8.9 Time histories, phase portraits, Poincaré maps and frequency power spectra of the shell center (chaotic vibrations) for different q_0 .

Type / q_0	$w(0.5; t)$	$w(\dot{w})$	$w_t(w_{t+T})$	Power spectrum $S(\omega)$
chaos (4648)				
hyper-chaos (4652)				
chaos (4656)				

in the center of $w_t(w_{t+T})$. In the chaos–hyperchaos regime, λ_1 and λ_2 achieve their maximum positive values, whereas λ_3 practically remains non-affected.

8.2.5 On the Sharkovsky's periodicity

One of the key problems in the theory of turbulence reduces to the following one: How to predict the beginning of its occurrence from a condition of stability and equilibrium?

Feigenbaum begun his investigations from the analysis of intervals between period doubling bifurcations of the square map. This map was first investigated in 1845 by P. Verhulst, who studied ecosystems, and hence the diagram $y = x^2 + c$ is named as Verhulst's diagram. The fundamental result obtained by Feigenbaum refers to its universal meaning. The analyzed mechanism called a route to chaos via period doubling bifurcations occurs not only for iterations $cx(1-x)$, but also, in the case of mappings into itself: $x^2 + c$, $c \sin(\pi x)$ and $cx^2 \sin \pi x$ defined on certain intervals.

Diagram of orbits shown in Fig. 8.48 allows to distinguish the attractive periodic orbits for the functions $f_c(x) = x^2 + c$. Observe that in certain parts the diagram is cut off. For instance, for $c \approx 1.75$ a white strip is visible, and the attracting orbits are of period-3. The natural question appears: Do other periodic orbits exist? The latter ones should be repellers, since the diagram presents only attractive orbits. It has been detected that the occurrence of the orbits with period-3 implies an occurrence of orbits with periods $n = 1, 2, 3, \dots$. In 1975, Lie and Yorke [Li and Yorke (1975)] considered orbits with period-3, but it happened that they studied only a particular case of Sharkovsky's theorem published in 1964 (see Section 2.4).

Let us compare two maps $f_c(x) = x^2 + c$ and $f_c(x) = z^2 + c$, i.e. the logistic map in real and complex plane, and constructed LE $\lambda_1(c)$ for the map $f_c(x) = x^2 + c$ (see Figs. 8.48, 2.9 and 2.10). The diagrams of the orbits for two functions have attracting, repelling and neutral points, which correspond to stable, unstable and neutral equilibrium states.

When starting from the vicinity of a fixed point, if we approach it via the infinite iterations process, this point is called an attractor.


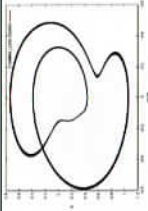
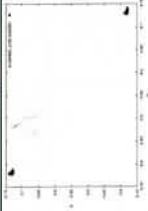
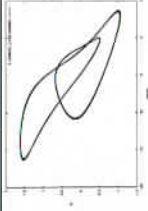
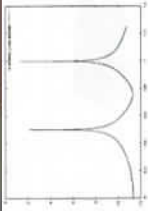

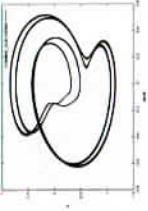
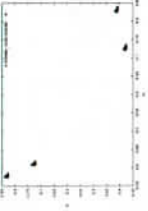
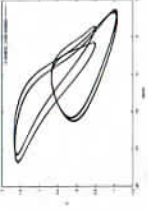
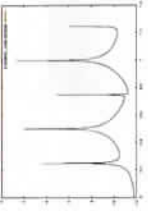

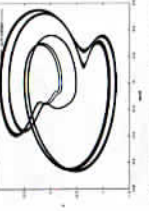
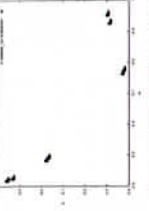
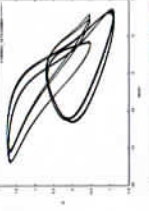


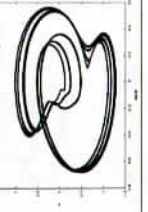
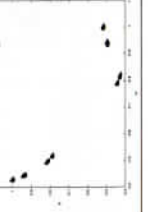

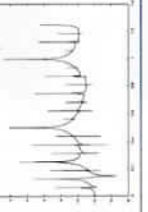
Table 8.10 Shell characteristics and Sharkovsky's order 3, 5, 7, 9, 13.

$w(0.5:t)$	$w(w)$	$w_t(w_{t-1})$	$w(dw/dx)$	$S(\omega)$	Surface	LE/q_0
						3 / 3740
						3*3 / 1936
						5 / 2220
						7 / 1472
						11 / 1328
						13 / 1257

Table 8.11 Shell characteristics and Sharkovsky's order 2, 3, 2, 5, 2, 7, 2, 9, 2, 11, 2, 13.

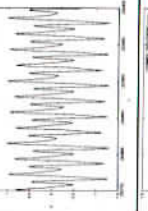
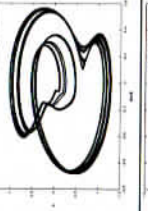
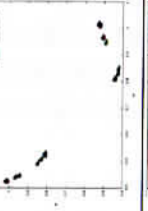

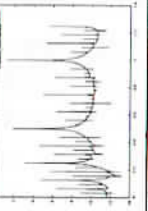

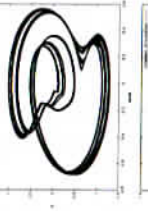

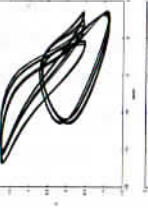
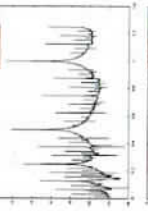

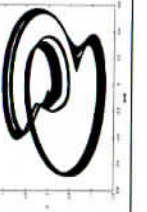

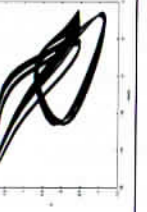
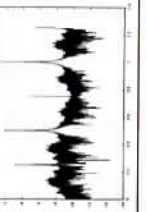
$w(0.5:t)$	$w(w)$	$w_t(w_{t-1})$	$w(dw/dx)$	$S(\omega)$	Surface	LE/q_0
						2*3 / 3728
						2*3*3 / 1945
						2*5 / 1420
						2*7 / 1636
						2*11 / 1280
						2*13 / 1260

Table 8.12 Shell characteristics and Sharkovsky's order $2^1, 2^2, 2^3, 2^4, 2^5, 2^6$.

$w(0.5;t)$	$w(w)$	$w_t(w_{t,T})$	$w(\partial w/\partial x)$	$S(\omega)$	LE/q_0
					$2^1 / 2350$
					$2^2 / 2400$
					$2^3 / 2470$
					$2^4 / 2494$

(Continued)

Table 8.12 (Continued)

					$2^5 / 2499$
					$2^6 / 2500$
					Chaos / 2510

(Tables 8.6 and 8.7). The following nonlinear phenomena have been detected:

1. In the case of period tripling, time history exhibits period partition into three equal parts, for 5–5 equal parts, and so on. Poincaré map consists of 3; 5; 7; 9; 11; 13 points. For orders $2 \cdot 3$, $2 \cdot 5$, $2 \cdot 7$, $2 \cdot 9$, $2 \cdot 11$, $2 \cdot 13$ we have groups consisting of 2 points each. Phase portrait shows period doubling. Observe that localization of points of Poincaré map is ordered for orbits with periods 3; $2 \cdot 3$; 9; $2 \cdot 9$; 13; $2 \cdot 13$, whereas for orders 5; 7; 11 and $2 \cdot 5$; $2 \cdot 7$; $2 \cdot 11$ a reconstruction takes place, and the points are located on the phase space in an arbitrary manner. The given orbits present windows of periodicity within chaos, and their structure is the same in the whole set of the control parameters $\{q_0, \omega_q\}$. All windows of periodicity have negative LEs $\lambda_i < 0, i = 1, 2, 3$.
2. For each orbit described so far (point 1), the changes in shell deflections in time $w(x, t)$ ($0 \leq x \leq 1; 127,500 \leq t \leq 128,000$) are shown, which allows to study a chart of the shell deformation depending on the orbit type 3; 5; 7; 9; 11. The increase in the period implies a transition into spatio-temporal chaos of the shell.